UNIVERSITY OF OKLAHOMA

GRADUATE COLLEGE

RELATIONSHIP BETWEEN THE MICRO-STRUCTURE OF CO–MO CATALYSTS SUPPORTED ON SILICA AND THE SELECTIVITY TOWARDS SINGLE-WALLED CARBON NANOTUBES

A DISSERTATION

SUBMITTED TO THE GRADUATE FACULTY

in partial fulfillment of the requirements for the

degree of

DOCTOR OF PHILOSOPHY

By

GIULIO LOLLI
Norman, Oklahoma
2007

ProQuest Information and Learning Company
300 North Zeeb Road
P.O. Box 1346
Ann Arbor, MI 48106-1346

RELATIONSHIP BETWEEN THE MICRO-STRUCTURE OF CO–MO CATALYSTS SUPPORTED ON SILICA AND THE SELECTIVITY TOWARDS SINGLE-WALLED CARBON NANOTUBES

A DISSERTATION APPROVED FOR THE
SCHOOL OF CHEMICAL, BIOLOGICAL & MATERIALS ENGINEERING

BY

Daniel E. Resasco

Richard G. Mallinson

Jeffrey H. Harwell

John F. Scamehorn

W. Arthur Porter

“Theory is when you know everything but nothing works. Experiments are when everything works but you don’t know why. Here we have put together theory and experiments: nothing works… and nobody knows why!”

Albert Einstein (1879-1955)

ACKNOWLEDGMENTS

First of all I need to thank my fiancée, she is my first breath in the morning and my last thought in the evening. Without her support I would not be here now. We decided together to start this journey and, now, after many sacrifices, is almost complete. I can only hope that our future will be as we dreamed.

Then I need to thank also my mother and father. I know what she would say: "We always come after Clementina", but the same would have happened if I switched, so you have to know that you are both my whole life. I have to thank them for the support they gave me in the past 28 years that had been critical in the past 10, since I left the comfort of my home to go to college, and then even further away…

I need to spend a special word for the wonderful people I have found here, from group-mates, to class-mates, room-mates, x-mates, people I worked with, from undergrads to postdocs. They all have been special friends! I hope to don't forget anybody: Jose, Mai, Steven, Phuong, Federico, Stefano, Armando, Deborah, Barbara, Jayme, Amelia, Tan, Veronica, Martina, Ariela, Lyon, Roberto, David, Andrea+Norma, Trung (big), Trung (little), Oat, Jerry, Mohamed, Jeff (the married), Jeff (the almost married), Quincy, Philip, Auan, Tanate, Air, Meaw, Pak, Kwan, Shah, Zhera, Selda, Holly, Phuong again, all the undergrads that stole our grad lounge and ate our doughnuts without knowing they were a week old.

I need also to thank all the people at SWeNT, without their huge efforts, the nanotubes group would not be as fructuous as it is. In particular without the work done by Leandro and Dave, I would have not been here today defending this thesis.

Special thanks go to my committee members: Dr. Resasco, Dr. Harwell, Dr. Scamehorn, Dr. Mallinson and Dr. Porter. In general I need to thank all the people at OU: all the faculty of the department, Terri that is always present to help everybody, Donna with her crazy emails, Alan that built wonderful equipment and was a constant presence for us 1st-floorers.

I want to add a personal thank to Dr. Porter. I don't think is correct to call him my mentor, but, at my eyes, he always resembled something like: "ok, this is the guy I want to look like, one day". And I will never forget the end of his emails: "steady on, skip". Steady on!

The last, but not least, is obviously Dr. Resasco. He has been my real mentor and advisor. He has always been present, in every moment, of the work and of my life in Norman. Without his incomparable help there will have been nothing in the last 4 years. And this is not only for me, the whole group and probably the whole OU will be different without him. I think the best way to describe him is using what my father said the first time he saw him: "Si vede dagli occhi, e' fenomenale", that translated in English sounds like: "You can see it from his eyes, he is terrific". Thank you very much Dr. Resasco. I will miss all of you!

TABLE OF CONTENTS

CHAPTER 1 1

1. Fundamentals of SWNT 1
  1.1. Structure 1
    1.1.1 Electronic Structure 1
    1.1.2. Optical transitions 4
  1.2. Properties 8
    1.2.1. Electrical properties 8
    1.2.2. Mechanical properties 8
    1.2.3. Thermal properties 10
  1.3. Applications 10
    1.3.1. Specialty products 10
    1.3.2. Commodities 13

CHAPTER 2 18

2. Growth of SWNT 18
  2.1 Growth and VLS mechanism 18
  2.2 Examples of SWNT synthesis 22
    2.2.1 Laser and Arc Discharge 22
    2.2.2. HiPCO 22
    2.2.3 CoMoCAT® 23
    2.2.4. Co-MCM41 25
  2.3 Selectivity toward SWNT 25
    2.3.1. Type I 26
    2.3.2. Type II 26
    2.3.3. Type III 28
  2.4. Conclusions 30

CHAPTER 3 38

3. Physical-Chemical Characterization of the Catalyst 38
  3.1. Preparation of the catalyst 38
  3.2. Phase evolution during reaction 39
  3.3. Role of the pre-reduction 45
    3.3.1 NO adsorption 45
    3.3.2. TPR 48
  3.4. Role of the support 50
    3.4.1. Morphology and chemistry of the support 50
    3.4.2 TPR 52
    3.4.3. NO adsorption 55
    3.4.4. Product Comparison 62

3.5. Product Quality 64
3.6. Conclusions 70

CHAPTER 4 73

4. Tailoring the catalyst to optimize selectivity Type I and II 73
4.1. Effect of the support 73
4.2 Effect of the pressure 77
4.3 Effect of gas composition 82
4.3.1 Inert diluting gasses 82
4.3.2. Non-noble diluting gas 84
4.3.3. Chemically active gasses 88
4.3.3.1 CO_2 Addition 89
4.3.3.2 Water addition 90
4.4 Effect of temperature 91
4.5 Conclusions 93

CHAPTER 5 96

5. Chemical potential model 96
5.1. Steps considered in the model 96
5.1.1. Carburization of the oxidic phase: 96
5.1.2. Catalyst Activation: 97
5.1.3. Decomposition of CO over the surface of the reduced Co cluster (interface 1) generating surface carbon species: 100
5.1.4. Carbon diffusion, nucleation and growth of SWNT: 100
5.1.5. Growth Termination: 100
5.2. Mathematical description of the model 101
5.2.1. Carburization 101
5.2.2. Active site formation 103
5.2.3. Rate of carbon deposition at interface 1: 111
5.2.4. Carbon diffusion and formation of SWNT at interface 2 113
5.3. Numerical fitting of the model 120
5.4. Conclusions 129

CHAPTER 6 138

6. Conclusions 138

APPENDIX A 142

A. Experimental methods..142
  A.1. SWNT Growth 142
    A.1.1. Catalyst preparation 142
    A.1.2. SWNT production 142
  A.2. SWNT Characterization Techniques 144
    A.2.1. Raman Spectroscopy 144
    A.2.2. SWNT suspensions 149
    A.2.3. SWNT (n,m) analysis 150
    A.2.4. TPO 151
  A.3. Catalyst characterization 151
    A.3.1. TPR 151
    A.3.2. NO Absorption 152
    A.3.3. XRD 152
  A.4 Kinetic Analysis. 153
    A.4.1. MS acquisition 153
    A.4.2. MS deconvolution 154

LIST OF TABLES

Table 3.1 Estimated crystallite sizes from X-ray diffraction of several species present in the catalyst during its lifetime. 41

Table 3.2 Physical-chemical characteristics of the SiO_2 supports used......................50

Table 4.1 Estimation of the diffusion coefficients of CO_2 in different gases. 83

Table 5.1. Fitting result from Figure 5.3; the mass balance closes very well validating the fitting. 121

Table 5.2 Numerical results of the fitting of Figure 5.6. 124

Table 5.3 Results of the fitting to reveal the effect of ψ_a and ψ_S on the reaction rate...126

LIST OF FIGURES

Figure 1.1 Representation of the Brillouin zone for a hexagonal lattice. 2

Figure 1.2 Band structure of graphite: left simulated by ab-initio calculations , right experimental. 2

Figure 1.3 Chiral map of SWNT and determination of the chiral vector. 3

Figure 1.4 a) Quantized waves inside a SWNT unit cell; b) corresponding wavevectors inside the Brillouin zone of a SWNT...4

Figure 1.5 Band structure (left) and joined density of states (right) of a SWNT. The transitions between the corresponding Van Hove Singularities are marked in general as E_{11} and E_{22}. 5

Figure 1.6 Optical absorption spectrum of a surfactant suspension of SWNT. The pair of transitions for the (7,6) nanotube are marked. In general the transitions from semiconducting nanotubes are denominated S_{xx} to be distinguished from the transitions of metallic SWNT denominated M_{xx}. 6

Figure 1.7 Contour plot of the emission wavelength from the semiconducting band gap in function of the excitation wavelength. Each feature corresponds to a specific semiconducting SWNT of corresponding S_{11} and S_{22} transitions. 7

Figure 1.8 Molecular dynamic model of plastic deformation of a SWNT. 9

Figure 1.9 Example of transparent conductive electrode produced in our lab (left) and a field emission display prototype from Samsung. 11

Figure 1.10 MWNT and nanofibers grown onto the surface of a carbon fiber. [curtesy of Veronica Magali Irurzun] 14

Figure 2.1 Schematic growth mechanism of silicon crystal by VLS, (a) Liquid droplet on substrate and (b) silicon nanowire growth...20

Figure 2.2 Molecular dynamic simulation of the formation of the first cap of a SWNT over Ni using CO as carbon source. 21

Figure 2.3Imaging of a carbon and catalyst plume produced after the vaporization of a carbon target by a laser pulse...22

Figure 2.4 Contour plot of the SWNT produced by CoMoCAT® (top) and HiPCO (bottom)...24

Figure 2.5 Density gradient separation of SWNT. CoMoCAT® (top right) and Laser (bottom)..28

Figure 2.6 Vertically aligned SWNT produced by CoMo supported on silicon wafer. 29

Figure 2.7 cartoon showing the mechanism of CoMoCAT®. The small Co particles generated on $CoMoO_4$ produce SWNT (left) while the large Co particles generated by segregated Co_2O_3 produce fibers or MWNT. [courtesy of Jose Herrera]....31

Figure 2.8 Comparison of the material produced: a) without the addition of Na; b) with the addition of 4% Na. The sodium disrupt the interaction between the Co and Mo as shown on top....32

Figure 3.1 XRD spectra of the CoMoCAT® catalyst 1:3 Co:Mo molar ratio 2 wt%. The ideal pattern for $CoMoO_4$ [7] is included for comparison....41

Figure 3.2 XRD spectra of the catalyst during its lifetime. The XRD patterns for $CoMoO_4$ (thin bars), and 2 forms of MoO_2 (thick bars full and dashed) are included for comparison. 42

Figure 3.3 Particular of Figure 3.2. The transition between $CoMoO_4$ and MoO_2 after reduction and heating is marked by an arrow. 43

Figure 3.4 XRD spectra of the material obtained after reaction with CO. The patterns for MoO_3 (black), Mo_2C (red) and metallic Co (blue dash) are included for comparison. 45

Figure 3.5 FTIR spectra of NO molecules absorbed onto monometallic Co (thin line) or Mo (bold line) on SiO_2. Evidenced is the difference between oxidized (red) and after reduction at 500ºC in H_2 (black)....46

Figure 3.6 FTIR spectra of NO absorbed on bimetallic CoMo supported on SiGel. The increasing reduction temperature in H_2 is shown on the right side. 48

Figure 3.7 TPR (temperature programmed reduction) of the bimetallic catalyst supported on SiGel. The vertical lines are the reduction temperatures analyzed in Figure 3.6. 49

Figure 3.8 Bridging of the metal oxides to the support via condensation of a silanol group....51

Figure 3.9 TPD (temperature programmed desorption) profile of the three different silica compared on table 3.2....52

Figure 3.10 Comparison of the catalyst's TPR profile prepared on the three different silica. 54

Figure 3.11 Evolution of the TPR profile after reduction in H_2 and reduction followed by heating in He. SiGel supported catalyst (left) and HiSil supported catalyst (right). 55

Figure 3.12 FTIR spectra of NO absorbed on bimetallic CoMo supported on HiSil. The increasing reduction temperature in H_2 is shown on the right side....56

Figure 3.13 Dipole moments in function of the geometry of the 2 ligands. When the dipole moment is zero, the vibration is IR inactive. The stronger the dipole, the stronger the IR absorption. In red is highlighted the metal site while in blue the NO molecule. The resulting dipole moment is shown with an arrow. 57

Figure 3.14 Fitting of the 2 bands of Co supported on silica. The calculated angle is 105º very close to the expected geometry for a tetrahedral configuration. 59

Figure 3.15 Calculated Mo-$(NO)_2$ angle in function of the reduction temperature for the HiSil supported catalyst. The Co angle was kept constant at 105º. For comparison, the monometallic Mo is also shown (full squares). 60

Figure 3.16 Calculated Mo-$(NO)_2$ angle in function of the reduction temperature for the SiGel supported catalyst. The Co angle was fixed at 105º (open squares) and 90º (full squares). 61

Figure 3.17 Calculated Co-$(NO)_2$ angle in function of the reduction temperature for the SiGel supported catalyst. The Mo angle was fixed at 90º. 62

Figure 3.18 Optical absorption spectra of the sodium cholate suspension of SWNT produced on SiGel (red) and Hisil (black) supported catalyst. 64

Figure 3.19 Raman spectrum of a SWNT sample. The SWNT's characteristic features are labeled. 65

Figure 3.20 Quality factor in function of the reduction temperature for the differently supported catalysts. 67

Figure 3.21 Estimation of (a) resonance ratio = (area of resonant band)/(area of nonresonant background); (b) normalized width = (width of resonant band)/(height of resonant band). 68

Figure 3.22 Resonant ratio in function of the reduction temperature for the differently supported catalysts. 69

Figure 4.1 Nucleation rate and corresponding diameter distribution (inset) for a given metal growth kinetic. 75

Figure 4.2 Effect of total pressure of CO on the carbon yield obtained. The other process variables were kept constant: reduction T 550°C 30 min.; reaction T 750°C 30 min. pure CO; He as inert gas; Catalyst 1:3 Co:Mo 2wt%. 79

Figure 4.3 Effect of pressure on the SWNT (n,m) distribution measured by optical absorption. 80

Figure 4.4 Extract from Figure 4.3 for the pressure range 0-40 psi. 81

Figure 4.5 Effect of inert gas dilution on the chirality of SWNT at constant partial pressure of CO. 84

Figure 4.6 Effect of N_2 dilution on the chirality of SWNT at constant partial pressure of CO. 86

Figure 4.7 Raman spectra of the SWNT produced using pure CO and 25% N_2 in CO. The D and D* bands are respectively enlarged on each side of the G band. 88

Figure 4.8 Optical absorption spectra of the SWNT obtained in pure CO (black) and 75% CO/He (red) with (dashed) and without (continuous) addition of 0.3% CO_2 89

Figure 4.9 Optical absorption spectra of SWNT, showing the effect of addition of increasing amount of water into the CO gas stream. 90

Figure 4.10 Effect of reaction temperature on the SWNT product distribution (conditions 60 psi pure CO). 92

Figure 5.1 Schematic of the SWNT growth mechanism. Two interfaces: gas-metal (1) and metal-SWNT (2) are used to model the process whose driving force is the difference C_S-C_f. 99

Figure 5.2 Prediction of activity based on different cases 111

Figure 5.3 Prediction of CO_2 evolution for the CoMoCAT® process using the model developed in equations 5.6, 5.38, and 5.39. 115

Figure 5.4 Prediction of CO_2 evolution for the CoMoCAT® process using the model developed in equations 5.6, 5.45, and 5.46. The effect at long time of the hindrance factor is evidenced. 119

Figure 5.5 Typical MS profile obtained at 20 psig CO pressure. Are evidenced the carburization of the oxide phase (blue shaded region) and the SWNT growth (bold red line). 121

Figure 5.6 Fitting of the experimental datasets using the model proposed in Equation 5.38. 123

Figure 5.7 Simulated data for the fitting of Figure 5.6. Inset is a magnification of the first minutes. 124

Figure 5.8 Graphical representation of the trend from table 5.2. 125

Figure 5.9 Trend of the free parameters in function of the pressure for the fitting of table 5.4. 127

Figure A.1 Typical raman spectrum of a SWNT sample. The 4 characteristic bands are marked: RBM (100-350 cm^{-1}), D (around 1300 cm^{-1}), G (1592 cm^{-1}) and D* (around 2600 cm^{-1}) 146

Figure A.2 Schematic of the origin of the D and D* band. The excited electron is transferred from the conduction to the valence band (bold continuous line) and the phonon is generated (bold dashed line). Because the phenomena happens at non zero momentum (k) to recombine with the hole it can either scatter elastically against a defect (long dash) or inelastically against a second phonon (short dash). The resulting Raman shift will be respectively 1,300 (D) and 2,600 (D*) cm^{-1}. 148

Figure A.3 Representation of the effect of the convolution integral (transfer function E). 154

Figure A.4 Raw MS signal obtained from the growth of SWNT at 20 psi. The molar fraction of CO (black), He (gray) and CO_2 (dashed red) are shown. 158

Figure A.5 CO signal from figure A.4 and its first derivative that represent E(t). 159

Figure A.6 Deconvolution using E(t) and FFT filtering of the signal (black) to obtain the real CO_2 concentration at the exit of the catalyst bed. 160

CHAPTER 1

1. Fundamentals of SWNT

1.1. Structure

The simplest definition of an ideal SWNT is “a rolled-up sheet of graphite”. This definition implies that, from a fundamental point of view, the physical properties and electronic structure should be derived from the ones of planar graphite.

1.1.1 Electronic Structure

The electronic structure of graphite has been studied deeply with quantum-chemical theoretical methods as well as experimentally. [1-5] This structure is characterized by a highly symmetric hexagonal array that determines a hexagonally shaped Brillouin zone with 3 axes of symmetry. The Brillouin zone is the “uniquely defined primitive cell of the reciprocal lattice in the frequency domain. The importance of the Brillouin zone stems from the Bloch wave description of waves in a periodic medium. From this analysis, it is found that the solutions can be completely characterized by their behavior in a single Brillouin zone” (Figure 1.1). [6] Inside the Brillouin zone of graphite there are three high-symmetry points: Γ is the center of the Brillouin zone, K is the corner of the hexagon, and M is the middle point of a face. [7] From the determination of the electronic structure of graphite (Figure 1.2) it follows that the K points are divergent and have non-zero electronic density at the

Fermi Level, even if there is not co-penetration of the valence and conduction bands. For this property, graphite is referred to as a semi-metal. [8,9]

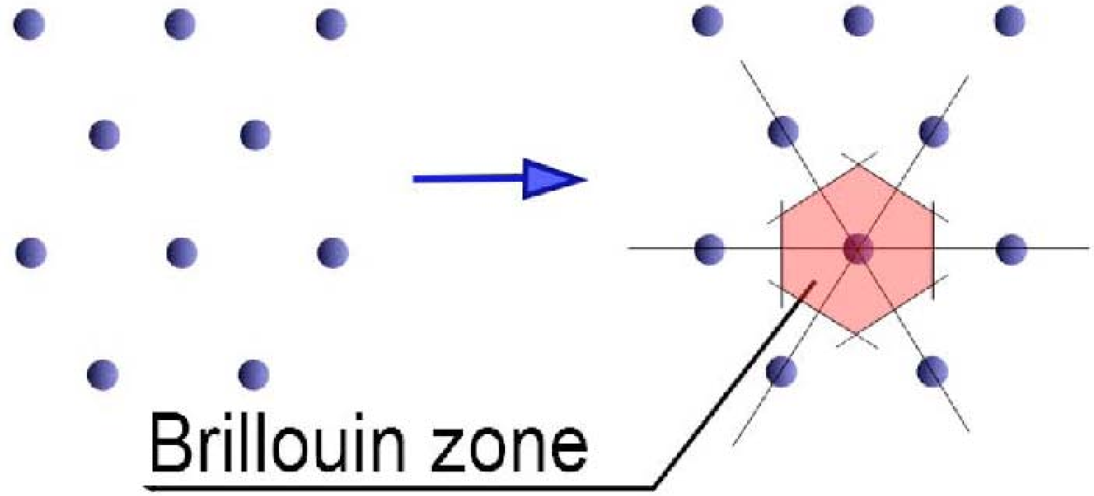

Figure 1.1 Representation of the Brillouin zone for a hexagonal lattice.

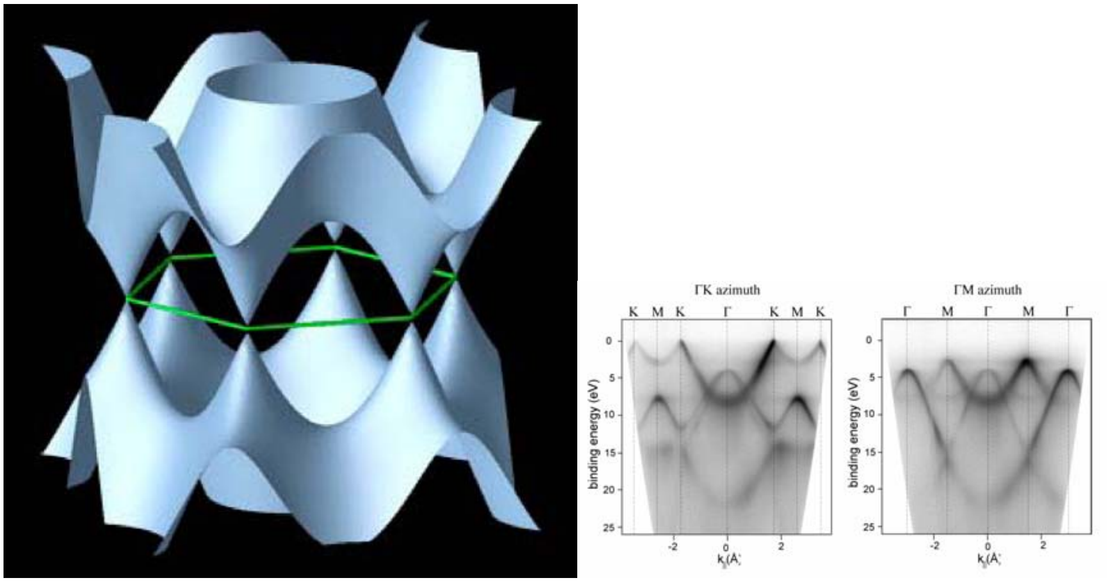

Figure 1.2 Band structure of graphite: left simulated by ab-initio calculations [10], right experimental. [11]

In the case of SWNT, besides the symmetries in the hexagonal structure of graphite, an additional helical symmetry is present, due to the cylindrical structure of the tube [12]; after a complete turn around the circumference, the structure has to be repeated. From a structural point of view that means that if we describe the resulting SWNT circumference with a vector onto the graphene sheet, the initial and final points of the vector should be equivalent. For example, if we decide to place the origin at the center of a hexagon, only circumference vectors that end in the center of another hexagon are allowed. [13] If we decompose the "chiral" vector in the components along the two symmetry axes of graphite, and we call it (n,m), only integer values of n and m will allowed (Figure 1.3). [14]

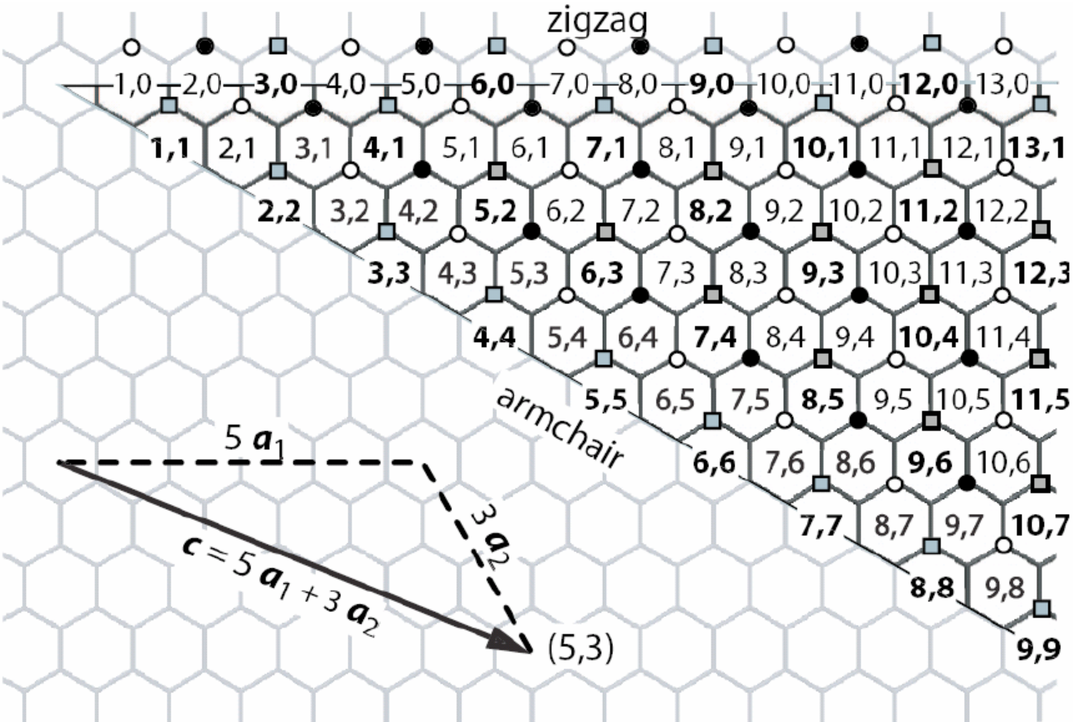

Figure 1.3 Chiral map of SWNT and determination of the chiral vector.

From a structural point of view, this means that only a discrete number (and consequently diameters) of SWNT is possible, and from an electronic point of view it means that the wave function associated with the electrons inside the molecular structure of a SWNT should be quantized. In particular, only wavevectors that are symmetric inside the lattice of the specific SWNT will be allowed. [10] This restriction results in discrete solutions inside the Brillouin zone of graphite. In particular, if one of these allowed wavevectors hits one of the K points of the graphite's Brillouin zone, the resulting nanotube will have non-zero density of electron at the Fermi level resulting in a metallic behavior. If the K point does not match with one of the allowed electronic wavevectors the resulting nanotube will behave as a semiconductor (Figure 1.4).

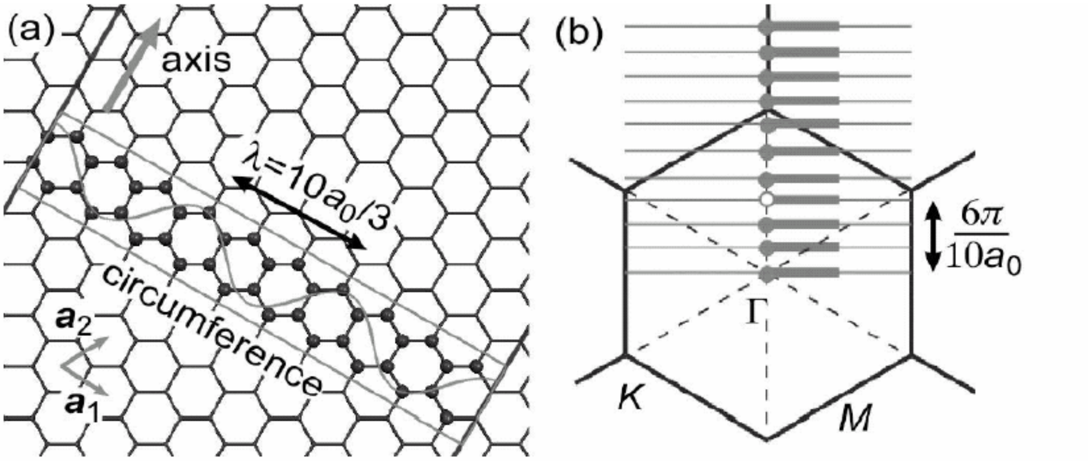

Figure 1.4 a) Quantized waves inside a SWNT unit cell; b) corresponding wavevectors inside the Brillouin zone of a SWNT. [10]

1.1.2. Optical transitions

For geometric properties the result is that, given the (n,m) chiral vector, if the difference between n and m is 0 or a multiple of 3 the SWNT will be metallic, otherwise it will be semiconducting. Moreover, being all the unit cells of a nanotube with the same quantized electronic structures, the electrons tend to pile up in very sharp and defined bands, which in the case of a perfect and infinitely long SWNT will diverge. These are called Van Hove singularities and the electronic transitions between the corresponding pairs of them (E_{xx}) provide the basis for spectroscopic techniques that are the main tools to determine the (n,m) structure of SWNT (Figure 1.5). [15-19] The generic electronic transition E_{xx} is generally referred to by the notation S_{xx} for semiconducting SWNT and M_{xx} for metallic.

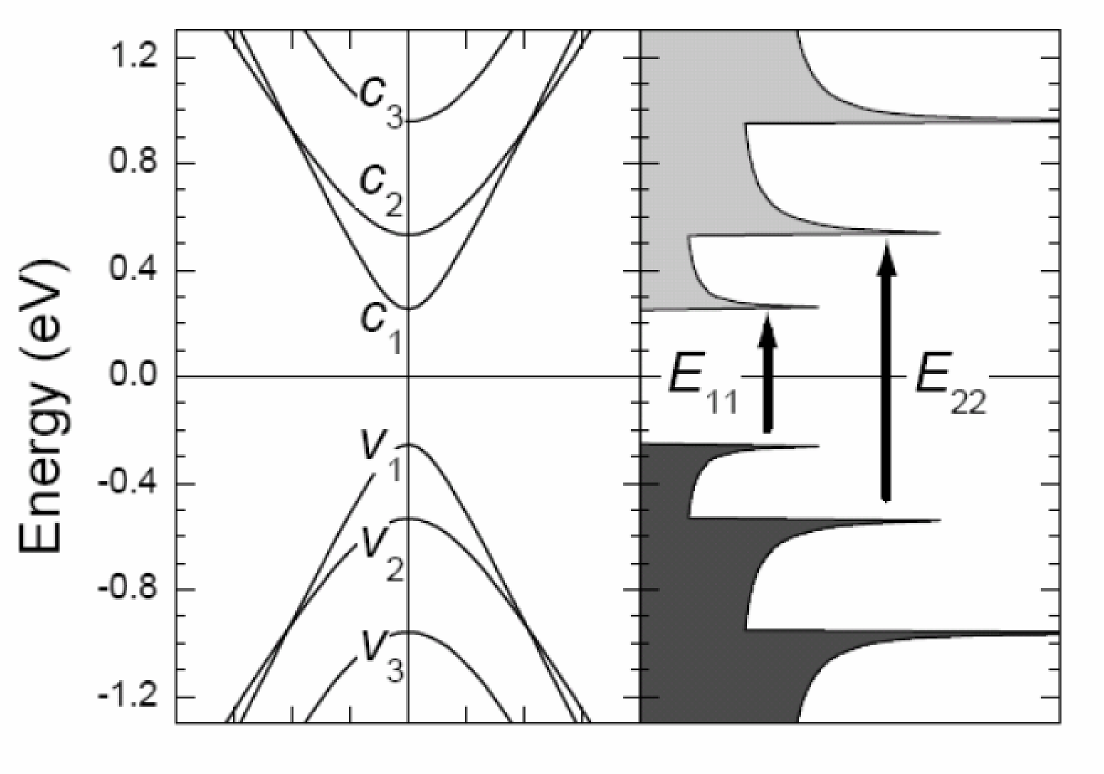

Figure 1.5 Band structure (left) and joined density of states (right) of a SWNT. The transitions between the corresponding Van Hove Singularities are marked in general as E_{11} and E_{22}. [10]

For every nanotube several direct transitions from the valence band to the conduction band, which result in an absorption spectrum, are possible (Figure 1.6). In the case of the semiconducting nanotubes the excited electron can relax thermally only up to the band gap, then a fluorescence photon is emitted. Based on this phenomenon it is possible to selectively excite the semiconducting nanotubes in the S_{22} transition or above and detect the emitted photon. The result of this analysis is a map of the optical transitions of the nanotubes that allows a very accurate identification of the (n,m) species for semiconducting SWNT (Figure 1.7). [20]

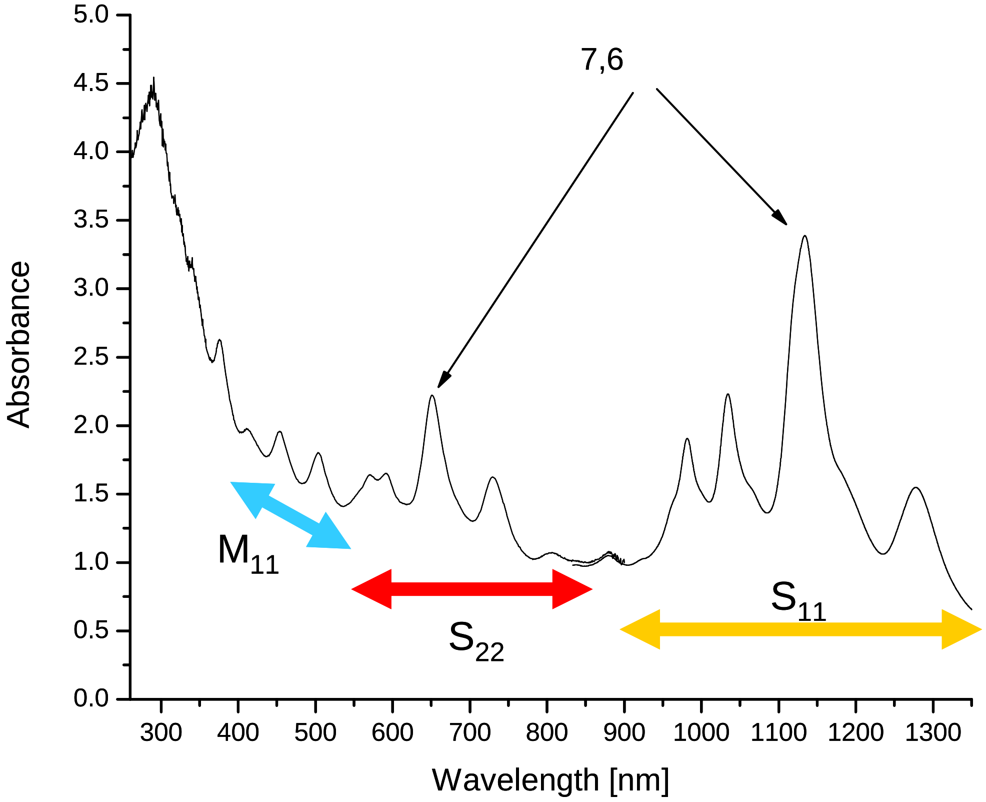

Figure 1.6 Optical absorption spectrum of a surfactant suspension of SWNT. The pair of transitions for the (7,6) nanotube are marked. In general the transitions from semiconducting nanotubes are denominated S_{xx} to be distinguished from the transitions of metallic SWNT denominated M_{xx}.

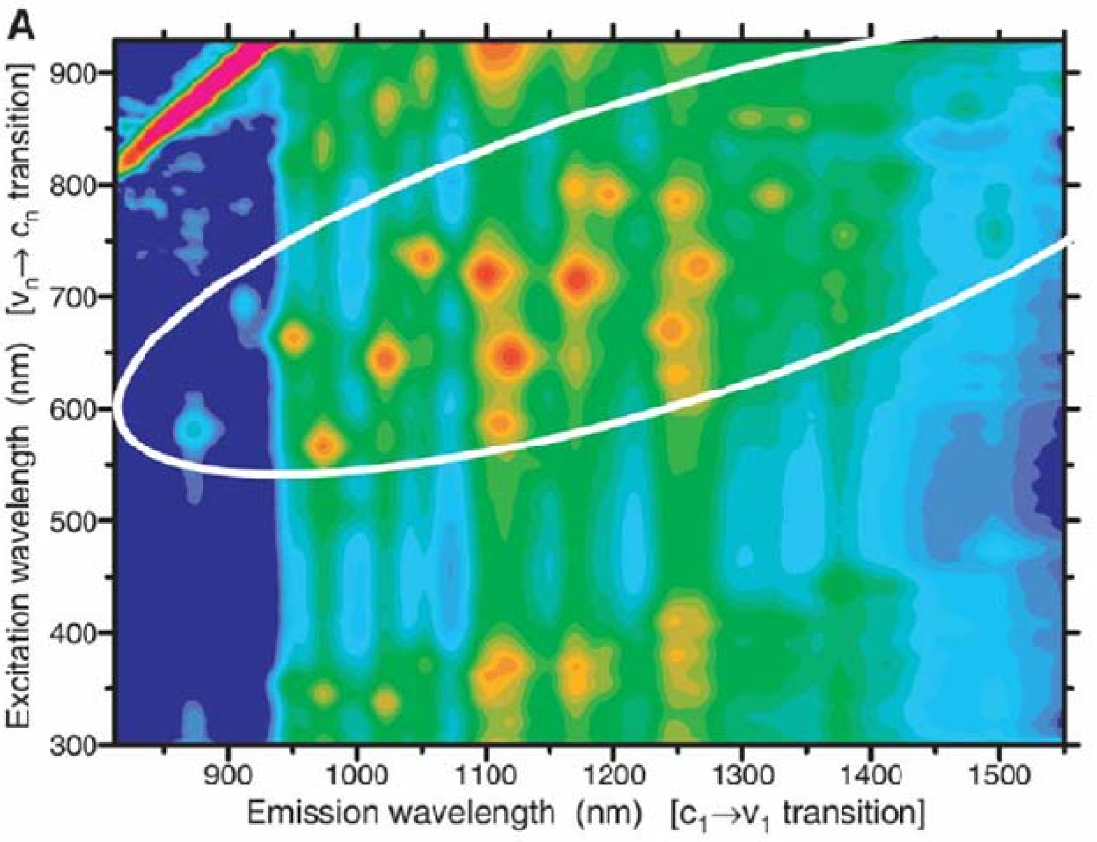

Figure 1.7 Contour plot of the emission wavelength from the semiconducting band gap in function of the excitation wavelength. Each feature corresponds to a specific semiconducting SWNT of corresponding S_{11} and S_{22} transitions. [21]

The ability to discriminate between specific (n,m) SWNT species is particularly important in applications in the electronic industry. For example two different SWNT with a very similar diameter like (7,5) and (6,6) (∅ = 0.818 and 0.814 nm, respectively) are completely different in terms of electronic structure: while (7,5) is a semiconductor with a band gap of 1.92 eV, (6,6) is a metallic nanotube. [22]

1.2. Properties

1.2.1. Electrical properties

The electrical properties of nanotubes are drastically different from the originating graphite. In the case of graphite, the electrical conductivity mostly occur in the layer between two graphene sheets, so graphite is an anisotropic conductor: the in-plane resistivity (9.6 10^{-6} Ωm) is about 5 times lower than the out-of-plane resistivity (4.1 10^{-5} Ωm) [23]. In the case of SWNT, the electrical properties depend greatly on their electronic structure; i.e. metallic or semiconducting. The metallic SWNT have been thought to be a possible candidate to replace high current power lines for several reasons: the light weight and high strength, which allows for making thicker cables, and the high current capacity, especially because they are not affected by electron drag at high currents. [24,25] Moreover, SWNT have been thought to present a form of conduction called “ballistic”. The moving electron, instead of hitting and moving the whole sea of electrons like in the case of a metal conductor, can move much more easily and cover longer distances: ideally it is the same electron that enters one end of the tube and exits from the other end. However, McEuen et al. [26] showed that the maximum ballistic length is around 500 nm, beyond this length SWNT behaves like a common metal. This is probably due to a lack of an ideal structure and the fact that hardly any SWNT is perfectly straight.

1.2.2. Mechanical properties

The mechanical strength of a single SWNT is due to the crystalline structure of its sp^2 bonds. These result in an even stronger system. The theoretical Young modulus E is estimated around 1 TPa that is around 4-5 times higher than steel. Concerning the mechanical resilience, there are several studies that model the possible deformation of a SWNT under stress and calculate the dissipated energy. [24] One of them is shown in Figure 1.8.

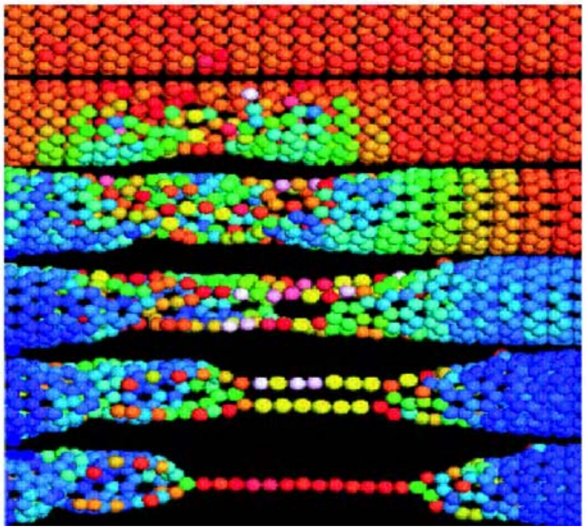

Figure 1.8 Molecular dynamic model of plastic deformation of a SWNT. [27]

Even when the intrinsic mechanical properties of individual SWNT are extraordinary, the more challenging aspect in their use in material reinforcement is how to bridge the matrix to the SWNT in a way to use all the properties of the material. In a mechanical system, the performance is limited by the weakest link. Up to now, there have been hundreds of studies that used SWNT as reinforcement material in, for example, polymer matrices, but the improvements obtained are far from the expected theoretical properties. [28 -33]

1.2.3. Thermal properties

The thermal properties of the SWNT are related in part to the electronic and in part to the mechanical structure. The influence of the electronic structure is associated to the existence of a quantized phonon structure. These phonons, which are vibrations along and across the SWNT, are responsible for thermal conductivity. In the case of SWNT, since the C-C bond is extremely stiff and the modulus extremely high, the phonon velocity is very elevated, thus making them an ideal thermal conductor. However, as said before for the mechanical and electrical properties, the final performance is limited by the weakest link (in this case, higher resistivity). The modulus of SWNT is so high that a mismatch [34] between the SWNT and the matrix moduli, for example a polymer, is so large that the phonon cannot leave the SWNT having a wavefunction that does not match the surrounding material. This mismatch, again, affects the final bulk property that is far from the intrinsic value of the SWNT. [35]

1.3. Applications

The SWNT applications can be divided into two big segments: specialty products and commodities. The price segment and availability needs for SWNT are completely different in the two cases.

1.3.1. Specialty products

The specialty products were the first to be targeted by the SWNT manufacturers and researchers. This is due to the fact that this market segment was the only one able to pay the high initial prices of production of SWNT and the only one demanding the small amounts available initially.

Typical applications in this category are in the electronic and the pharmaceutical industries. In the first case, a possible application is the use of semiconducting SWNT as field effect transistors and the use of metallic SWNT as vias to interconnect the several regions of the wafer. [36] This was seen as the first attempt to bridge the silicon electronics with the organic. Moreover, the high premium associated with the production of these electronic devices can absorb the high SWNT price. Other examples in this field are conductive transparent electrodes for touch screen displays and field emission displays (Figure 1.9)

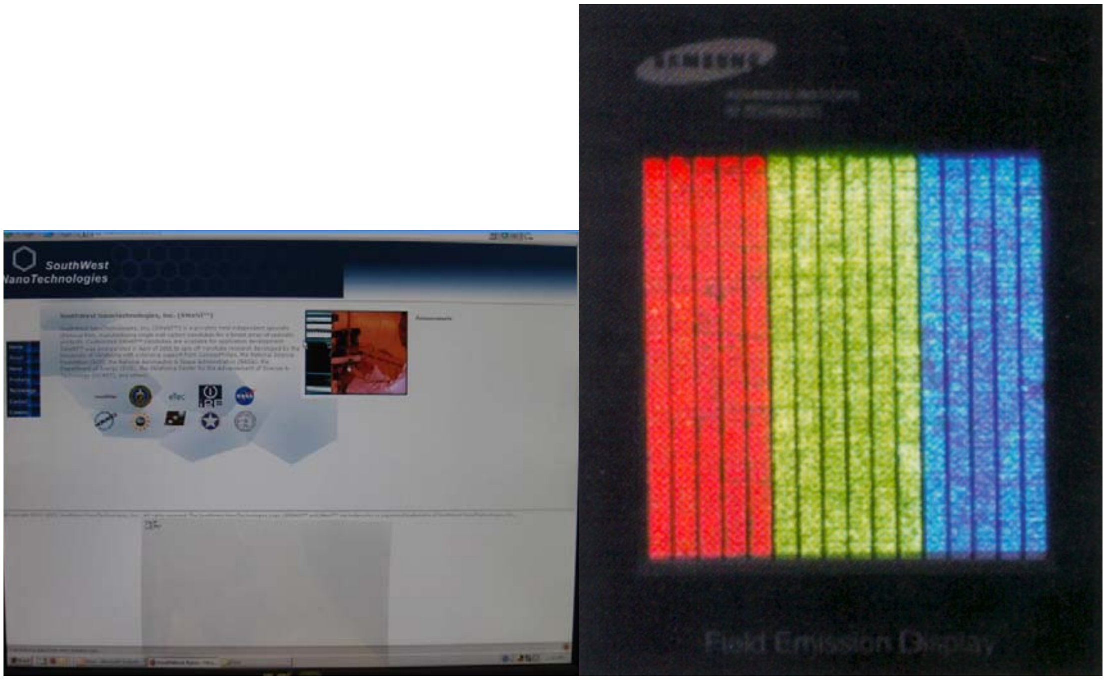

Figure 1.9 Example of transparent conductive electrode produced in our lab (left) and a field emission display prototype from Samsung.

Another important application is the use in the pharmaceutical industry. A typical approach is using the SWNT alternatively as a drug delivery vehicle or as a part of the drug itself. In the first case, a drug molecule is embedded inside the SWNT and the outside is covered with targeted receptors, releasing the drug only where needed. [37] In the second case the SWNT is the active drug itself. For example attaching a cancer selective protein on the outside of the SWNT will allow accumulation of the SWNT inside the tumor and afterwards, using their optical properties, to image or even burn the cancer cells: thus providing a cancer diagnostic and eventually a cancer treatment. [38] Even in this case, the pharmaceutical industry can charge a premium for a more effective or different drug composition and pay for the high cost associated with the use of high quality SWNT.

In both cases, even if the target price is high, there are quality-associated costs that should be considered. For example, for the use in the electronic industry, an effective and efficient method of separation or selective production of a specific SWNT kind (semiconducting and metallic in general or a specific (n,m) in particular) is needed. In the case of medical applications, the quality and purity of SWNT should be extremely high to limit the toxic effects associated with the nanotubes themselves and especially with the catalyst residues that in general include toxic metals like Co, Ni or Fe.

1.3.2. Commodities

On the other category lie many products that we use daily, and that can be improved with the use of SWNT. In this category, the material technology and the composite materials are the main players. However, for such applications the production scale should be able to increase from few milligrams to tons and the price, considering the possible improvement, should be competitive with the other options like MWNT or carbon fibers, just to stay in the same type of material.

For this reason, at first, the SWNT are being thought more as an improvement than as a replacement of the current technologies. For example, the carbon fibers composites are fabricated by laying sheets of carbon fiber tissue and embedding them in an epoxy resin. One of the problems with these materials is that, as the resin wears out on the outside, they tend to exfoliate. In this regard, SWNT can be thought as a bridge between the fibers and especially between the layers. This should also eventually improve the electrical and thermal conductivity in the perpendicular direction. Another approach is to attach them, or better yet, to grow them, on the external surface of the carbon fibers. This arrangement can increase the surface area of the fiber/SWNT composite, increasing the adhesion with the matrix. An example is illustrated in Figure 1.10.

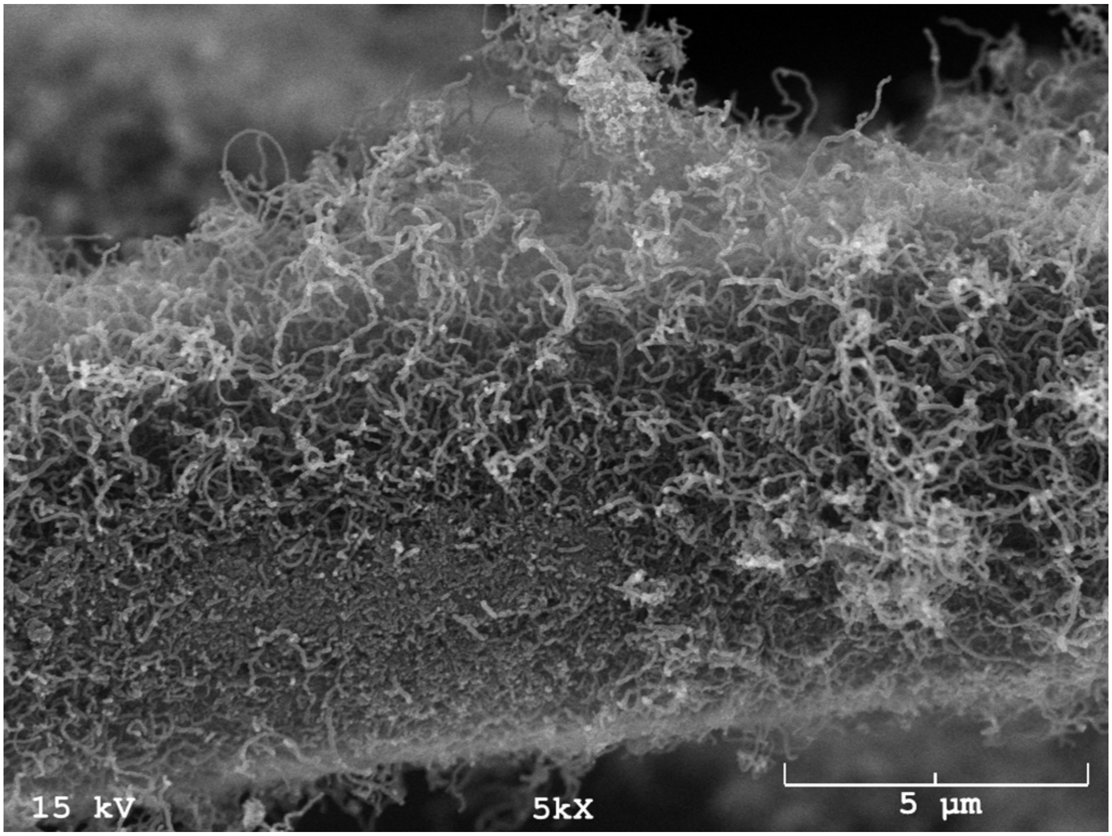

Figure 1.10 MWNT and nanofibers grown onto the surface of a carbon fiber. [curtesy of Veronica Magali Irurzun]

Reference:

1 M.S. Dresselhaus, G. Dresselhaus, R. Saito *World of Carbon* **2001** 1, 25-43.

2 A.V. Okotrub, L.G. Bulusheva, A.V. Gusel'nikov, A.L. Chuvilin, A. Fonseca *Proceedings - Electrochemical Society* **2000** 10, 229-235.

3 S. Kawasaki, F. Okino, H. Touhara, N. Liu, T. Nakajima *Advances in Quantum Chemistry* **2001** 37, 301-309.

4 R.C. Tatar, S. Rabii *Physical Review B:Condensed Matter and Materials Physics* **1982** 25(6), 4126-41.

5 J.M. Andre, G. Leroy *International Journal of Quantum Chemistry* **1969** 3(6), 983-99.

6 H. Ibach, H. Lüth Solid-State Physics, An Introduction to Principles of Materials Science, second edition **1996** Springer-Verlag

7 Ge.G Samsonidze, R. Saito, A. Jorio, A.G. Souza Filho, A. Gruneis, M.A. Pimenta, G. Dresselhaus, M.S. Dresselhaus *Physical Review Letters* **2003** 90(2), 027403/1-027403/4.

8 B.T. Kelly *Physics of Graphite* **1981** Applied Science Publ., London.

9 R.K. Kirby, T.A. Hahn, B.D. Rothrock in *American Institute of Physics Handbook*, third edition **1972** McGraw Hill.

10 S. Reich, C. Thomsen, J. Maultzsch Carbon Nanotubes: Basic Concepts and Physical Principles **2004** Wiley-VCH.

11 www.tp2.uni-erlangen.de/Toroid/results.html

12 R.A. Jishi, M.S. Dresselhaus, G. Dresselhaus *Physical Review B: Condensed Matter and Materials Physics* **1993** 47(24), 16671-4.

13 F. Torrens *Internet Electronic Journal of Molecular Design* **2004** 3(8), 514-527.

14 A.G. Souza Filho, A. Jorio, Ge.G. Samsonidze, G. Dresselhaus, M.S. Dresselhaus, A.K. Swan, M.S. Unlu, B.B. Goldberg, R. Saito, J.H. Hafner, C.M. Lieber, M.A. Pimenta *Chemical Physics Letters* **2002** 35(4) 62-68.

15 R. Saito, K. Sato, Y. Oyama, J. Jiang, Ge.G. Samsonidze, G. Dresselhaus, M.S. Dresselhaus *Physical Review B: Condensed Matter and Materials Physics* **2005** 72(15), 153413.

16 P. Corio, A. Jorio, N. Demir, M.S. Dresselhaus *Chemical Physics Letters* **2004** 392(4-6), 396-402.

17 A. Jorio, R. Saito, T. Hertel, R.B. Weisman, G. Dresselhaus, M.S. Dresselhaus *MRS Bulletin* **2004** 29(4), 276-280.

18 A. Jorio, A.G. Souza Filho, G. Dresselhaus, M.S. Dresselhaus, R. Saito, J.H. Hafner, C.M. Lieber, F.M. Matinaga, M.S. Dantas, M.A. Pimenta *Physical Review B: Condensed Matter and Materials Physics* **2001** 63(24), 245416.

19 A.G. Souza Filho, A. Jorio, J.H. Hafner, C.M. Lieber, R. Saito, M.A. Pimenta, G. Dresselhaus, M.S. Dresselhaus *Physical Review B: Condensed Matter and Materials Physics* **2001** 63(24), 241404.

20 H. Htoon, M.J. O'Connell, S.K. Doorn, V.I. Klimov *Physical review letters* **2005** 94(12), 127403.

21 S.M. Bachilo, L. Balzano, J.E. Herrera, F. Pompeo, D.E. Resasco, R.B. Weisman *Journal of the American Chemical Society* **2003** *125*, 11186.

22 R.B. Weisman, S.M. Bachilo *Nano Letters* **2003** 3(9), 1235-1238.

23 R.L. Powell, G.E. Childs in *American Institute of Physics Handbook* third edition **1972** McGraw Hill.

24 M.S. Dresselhaus, G. Dresselhaus, A. Jorio, A.G. Souza Filho, Ge.G. Samsonidze, R. Saito *Journal of Nanoscience and Nanotechnology* **2003** 3(1/2), 19-37.

25 P. Poncharal, C. Berger, Y. Yi, Z.L. Wang, W.A. de Heer *Journal of Physical Chemistry B* **2002** 106, 12104.

26 H. Kuzmany, J. Fink, M. Mehring, S. Roth *Electronic Properties of Molecular Nanostructures* **2001** American Institute of Physics.

27 J.A. Elliott, J.K.W. Sandler, A.H. Windle, R.J. Young, M.S.P. Shaffer *Physical Review Letters* **2004** 92(9), 095501.

28 M.L.P. Ha, B.P. Grady, G. Lolli, D.E. Resasco, W.T. Ford *Macromolecular Chemistry and Physics* **2007** 208(5), 446-456.

29 F. Buffa, G.A. Abraham, B.P. Grady, D.E. Resasco *Journal of Polymer Science, Part B: Polymer Physics* **2007** 45(4), 490-501.

30 M.N. Tchoul, W.T. Ford, G. Lolli, D.E. Resasco, M.L.P. Ha, B.P. Grady *Abstracts of Papers, 232nd ACS National Meeting, San Francisco, CA, United States, Sept. 10-14, 2006* **2006**

31 M.L.P. Ha, B.P. Grady *Abstracts of Papers, 229th ACS National Meeting, San Diego, CA, United States, March 13-17, 2005* **2005**

32 E.M. Moore, D.L. Ortiz, V.T. Marla, R.L. Shambaugh, B.P. Grady *Journal of Applied Polymer Science* **2004** 93(6), 2926-2933.

33 O. Probst, E.M. Moore, D.E. Resasco, B.P. Grady *Polymer* **2004** 45(13), 4437-4443.

34 V. G. Hadjiev, C. A. Mitchell, S. Arepalli, J. L. Bahr, J. M. Tour, R. Krishnamoorti *Journal of Chemical Phyisics* **2005** 122, 124708

35 S.S. Rahatekar, M. Hamm, M.S.P. Shaffer, J.A. Elliott *Journal of Chemical Physics* **2005** 123(13), 134702/1-134702/5.

36 H.R. Byon, H.C. Choi *Journal of the American Chemical Society* **2006** 128(7), 2188-2189.

37 United States Patent 20060017191

38 X. Huang, W.Q. Ding, J.L. Vaught, R.F. Wolf, J.H. Morrissey, R.G. Harrison, S.E. Lind *Blood* **2006** 107(3), 980-986.

CHAPTER 2

2. Growth of SWNT

Our research group developed in the past 8 years a unique method to produce SWNT denominated CoMoCAT®. [1-4] It is based on the use of a Co/Mo mixed oxide catalyst supported over a high surface area silica substrate. When contacted at high temperatures, above 700 °C, with CO, the so called Boudouard reaction (CO disproportion to CO_2 and solid carbon) takes place. When the catalyst presents the right Co/Mo ratio and surface dispersion the selectivity towards SWNT is extremely high. [5,6]

The first characterization of the Co/Mo catalyst and the catalytic mechanism has been done mainly by Herrera during his PhD work. [3,5] He explained the high selectivity by the interaction between the two metals involved: cobalt and molybdenum.

2.1 Growth and VLS mechanism

The growth of SWNT requires the presence of a metal able to dissolve, inside its lattice structure, an appreciable amount of carbon. The carbon then can diffuse on the surface and after reaching a condition of super-saturation tends to precipitate out forming carbon structures. [7-9] This mechanism involves a gas-phase component (the carbon containing gas), a metal-carbon alloy and a precipitated carbon specie. Even though it is formally a CVD (chemical vapor deposition) method, it is sometimes referred to as VLS (Vapor-Liquid-Solid) process due to the similarity of the mechanism with the phase transformation phenomena. [10-12]

This process was developed and studied since the 1960s, but has come back recently to explain the catalytic growth of Si-nanowires over Au catalyst. [13-16] In this case, the system forms an Au/Si alloy that, at the synthesis temperature, is melted (from that the name VLS) and after super-saturation it precipitates out crystalline silicon in the shape of a Si-nanowire (Figure 2.1). In the case of carbon nanotubes the metallic particle is not completely melted like in the pure VLS mechanism, but due to the high temperatures and small cluster size, the mobility is extremely high and the carbon diffusion inside the particle is much higher than in a bulk solid material, so it presents a liquid-like behavior.

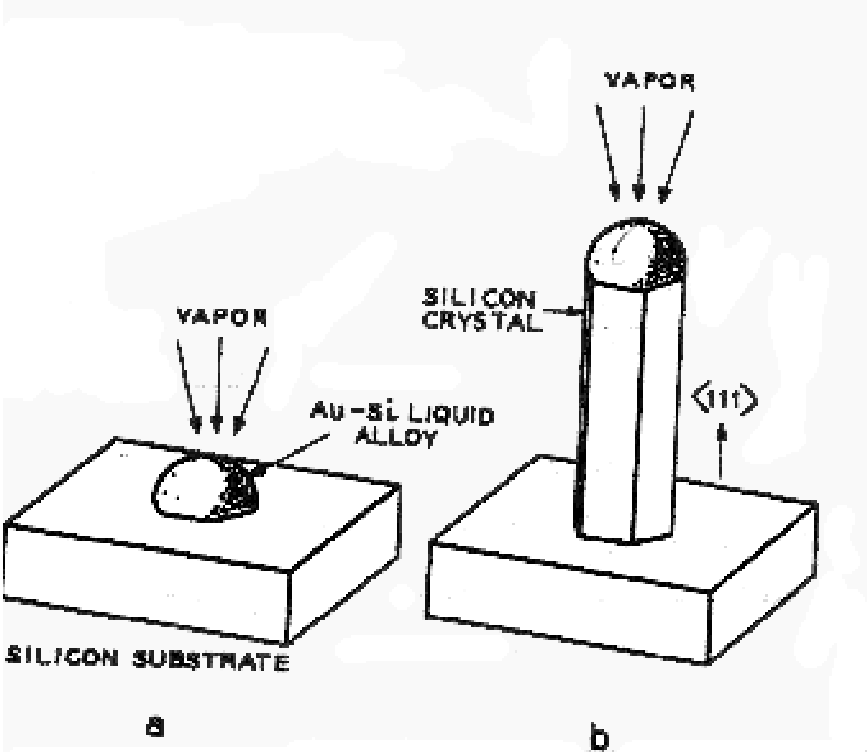

Figure 2.1 Schematic growth mechanism of silicon crystal by VLS, (a) Liquid droplet on substrate and (b) silicon nanowire growth. [13]

The type of carbonaceous structure that precipitates out of the metal-carbon system is determined mainly by the size of the metal particle. In the case of very small particles (below 2 nm) the material produced is SWNT. If the particle size increases, the probability of forming larger and multi-walled structures increases as well. Generally, larger particles (10-20 nm) tend to form large MWNT. [17] When the particle gets even bigger, bamboo-like structures, nanofibers or whiskers are the main product. This trend can be explained by the ratio between surface diffusion and bulk diffusion: a small particle is dominated by the surface (the ratio surface/bulk scale with 1/size) so the carbon tends to diffuse quickly on the surface of the particle forming a cap and then a hollow structure. This nucleation mechanism has been simulated by the group of Prof. Balbuena at Texas A&M using as model a Ni cluster and CO gas phase (Figure 2.2). [18-20] When the particle gets bigger the volume dominates, so the carbon tends to diffuse slowly inside the bulk of the particle, precipitating all around the surface from inside, which forms more filled structures.

Moreover, in the case of SWNT, the size of the structure formed is proportional to the size of the metal particle that catalyzed the growth. Generally there is an experimentally determined factor of 1.1-1.2 between the particle size and the diameter of the SWNT. [21,22] That means that in the case of a good catalyst for producing SWNT the size of the metal particle that dissolves the carbon should be around 1 nm and the particle distribution must be very narrow to prevent the presence of larger particles that will not be selective towards SWNT.

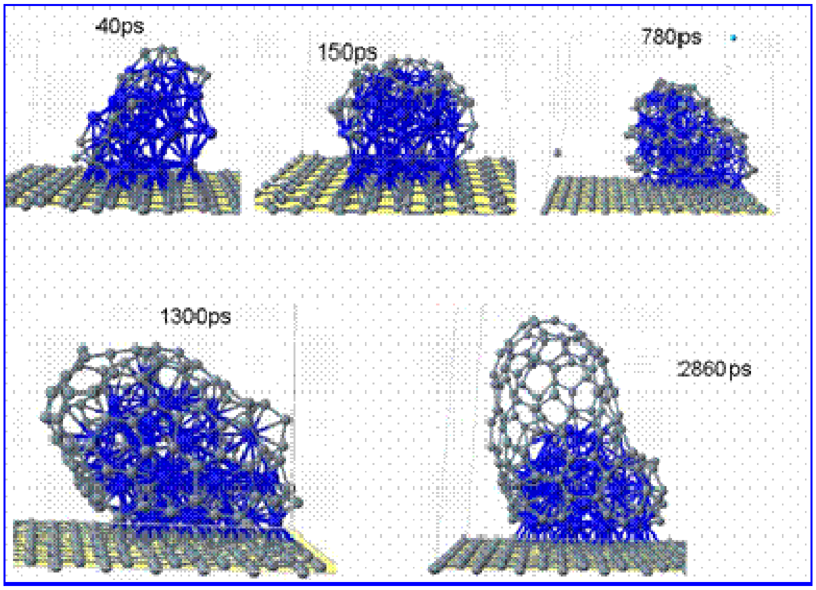

Figure 2.2 Molecular dynamic simulation of the formation of the first cap of a SWNT over Ni using CO as carbon source. [18]

2.2 Examples of SWNT synthesis

2.2.1 Laser and Arc Discharge

This general VLS mechanism is common to all the methods of producing SWNT. For example in the laser ablation or arc discharge method a target made of carbon and typically Ni/Y catalyst is hit and vaporized by a laser beam or electric arc in an Ar atmosphere. Inside the plume of vaporized material (Figure 2.3) the metal atoms condense and start dissolving carbon forming nanostructures. In this case, the size of the metal particle is not controlled and governed only by the condensation mechanism of the metal atoms (so depending on the gas atmosphere, pressure, temperature, flow rate, etc.) resulting in a wide distribution of carbon structures. Moreover, the carbon can even condense spontaneously resulting in large amounts of amorphous carbon, entangled in a network of carbon structures. [23 -29]

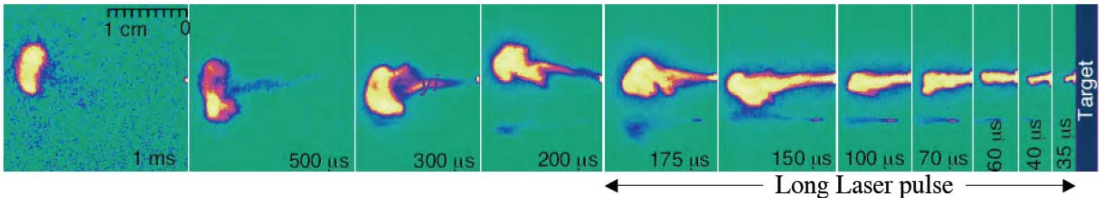

Figure 2.3Imaging of a carbon and catalyst plume produced after the vaporization of a carbon target by a laser pulse.

2.2.2. HiPCO

In another widely known process, HiPCO, the metal is introduced in the form of $Fe(CO)_5$, a gaseous compound, mixed with a CO stream and suddenly decomposed in a hot chamber under high pressure of CO. The metallic iron released tends to condense forming small Fe particles that start the growth of SWNT [30-32] similar to what happens with the Ni particles in the “laser” process. Even in this case the size of the particles is controlled by the condensation mechanism, so the distribution of structures is quite wide. An advantage over the “laser” process is the lack of spontaneous gas-phase carbon condensation: the Boudouard reaction ($2\ CO \leftrightarrow CO_2 + C_s$) has to be catalyzed by a metal particle to proceed at high rate.

2.2.3 CoMoCAT®

In the case of CoMoCAT® the size of the Co particle is controlled by the interaction with the Mo. In the catalyst the Co and Mo are in the form of mixed oxide, similar to the crystal structure of $CoMoO_4$, but highly dispersed. This is activated by a pre-reduction step in H_2 to generate oxygen vacancies and form more reactive oxidic specie. The metal oxide is very thermally stable due to the strong interaction with the support and can be heated to high temperatures (around 750 °C) without undergoing sintering. When contacted with CO, however, a chemical attack takes place and the oxidic structure (MoO_x with Co ions in the tetrahedral vacancies of the octahedral Mo structure) is converted to carbide. The resulting Mo_2C formed cannot stabilize the Co that tends to precipitate onto the surface in very small Co clusters. As soon as the cluster reaches a minimal size, the growth of the SWNT takes place preventing further agglomeration. This results in a very high selectivity towards SWNT and a very narrow distribution of diameters (Figure 2.4). [1-6]

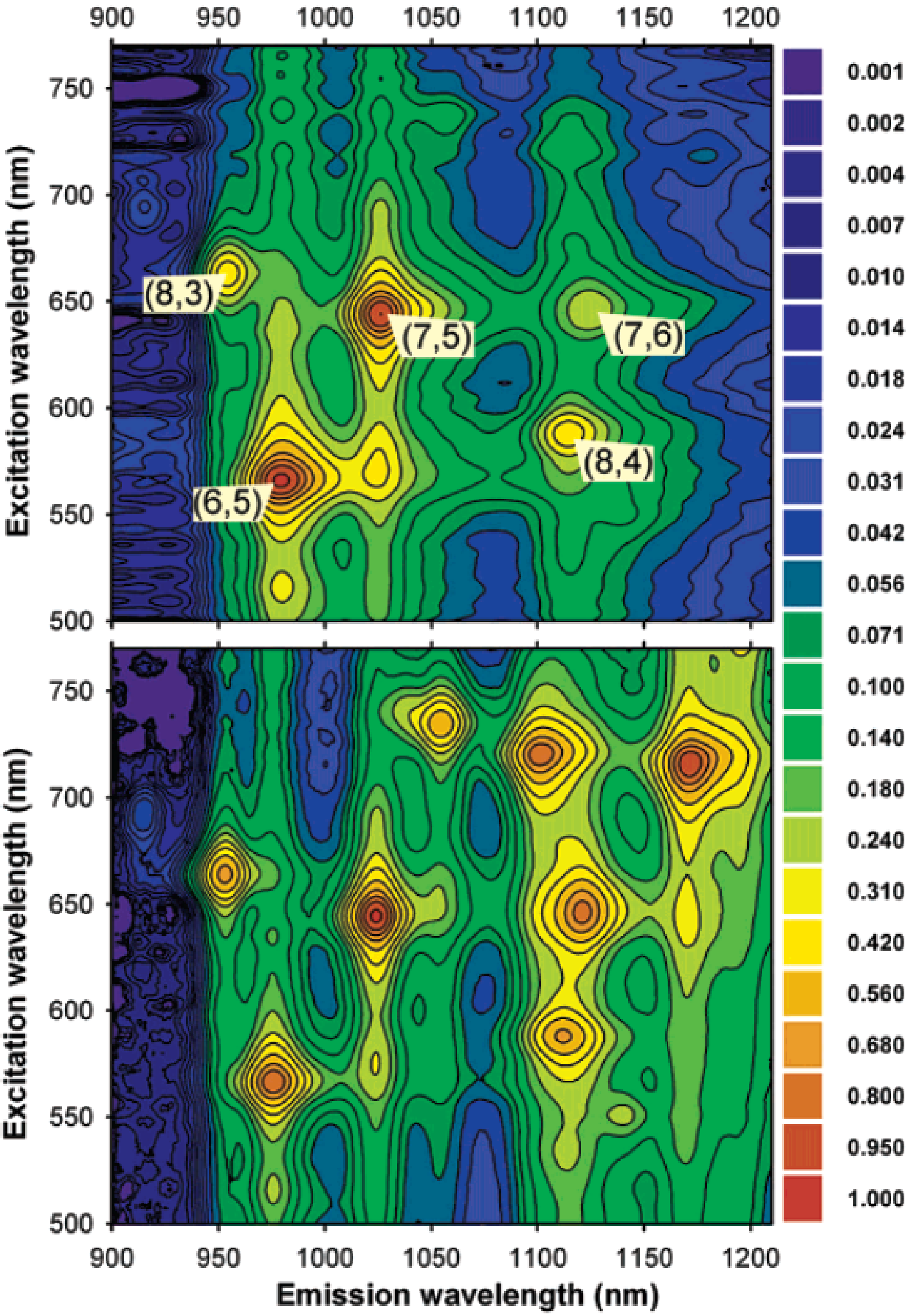

Figure 2.4 Contour plot of the SWNT produced by CoMoCAT® (top) and HiPCO (bottom)

2.2.4. Co-MCM41

Another method that should be mentioned due to the similarity with CoMoCAT® is the Co/MCM-41 developed at Yale University. In this case, only Co is present. However the Co^{2+} ions are embedded in the MCM-41 framework and, even when they get reduced at high temperature (up to 900 °C in H_2), the sintering is prevented by the physical structure of the meso-porous support with its long and straight channels that limit the mobility of the ions. [33 -37]

Many other production methods have been proposed in the literature, but they are all different variations of the same mechanism: the catalyst is generally Fe, Ni or Co stabilized in some way and contacted with a carbon containing gas. For the source of carbon, many gases have been used besides CO, like methane, ethane, ethylene, acetylene and ethanol, just to cite a few. [38,39] In general, these gases result in much higher carbon yields (the amount of carbon deposited per unit of catalyst) but the selectivity towards SWNT is usually lower, because these feedstocks tend to thermally decompose, or the byproduct of the reaction can affect the structure of the catalyst (this is the case, for example, of H_2 in methane decomposition).

2.3 Selectivity toward SWNT

SWNT are not a well defined molecule for which the simple chemical engineering concept of selectivity can apply. This is due to their ambiguous nature: on one side they are a perfectly crystalline well defined carbon structure, but on the other side a small modification in the helicity, defined by the chiral vector (n,m), leads to a completely different electronic structure. For that reason, we can define at least three different kinds of selectivity. [40]

2.3.1. Type I

Type I selectivity, which is probably the best known, is the selectivity of SWNT versus other forms of carbon. It is also the easiest to obtain. Almost all the supported catalyst methods cited before and HiPCO are highly selective, only laser ablation and arc discharge tend to produce more amorphous carbon. We can easily say, for all of them, that the selectivity towards SWNT is at least 95% or even more.

2.3.2. Type II

Type II selectivity is probably the most challenging to control. Inside the product SWNT it is the selectivity towards a specific (n,m) chiral vector. In this respect, the unsupported methods (from HiPCO to Laser and Arc) are intrinsically unselective. This is due to the process that leads to the formation of the catalytic metal particle that is determined, in this case, only by the condensation process and is almost impossible to control at the nanoscale. Between the supported catalyst methods, CoMoCAT® has shown the ability to obtain a narrow distribution [6] due to the chemically controlled mechanism of nucleation. We have also shown the ability to alter this narrow distribution by changing the reaction conditions and the catalyst formulation. [40,41]

The selectivity towards a specific SWNT is very important in the electronic industry where semiconductor SWNT can be used as field effect transistors [42] or metallic SWNT can be used as high current-load conductors for connecting different areas of the circuit.

Up to now, many methods have been proposed to post-separate SWNT in their chiral components, [43-46] but only few of them were successful, and none economically feasible. Between them, the method developed by Hersam et al. [44,47], using a density gradient ultracentrifugation, exploiting the slightly different density between the different kinds of SWNT is probably the most advanced one. In their work they also show that the best results in separations are obtained using a material that has already a predominant fraction of a specific (n,m) kind (i.e. our CoMoCAT® tubes), stressing the importance of selective production, even when using a subsequent refining separation (Figure 2.5).

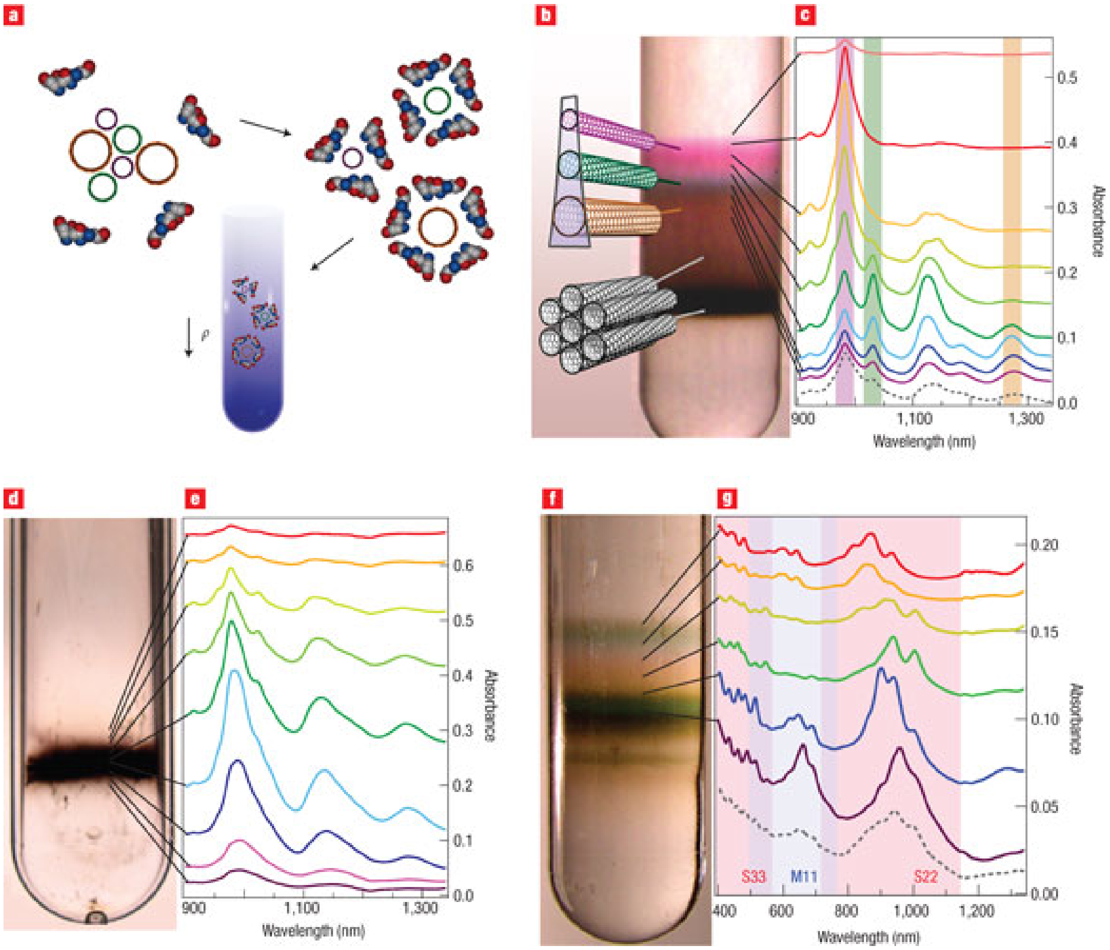

Figure 2.5 Density gradient separation of SWNT. CoMoCAT® (top right) and Laser (bottom) [47]

2.3.3. Type III

Type III selectivity is the selectivity towards a specific length. This is particularly important in applications like material reinforcement, where the high aspect ratio is related to the improvement of the final composite. If it is possible to cut the SWNT using harsh acid attacks like the "Pirana" method, [48] however it is impossible to put them back together, so producing as long as possible nanotubes become critical. In the case of the electronic industry, the length of an interconnection or a transistor is also important: it needs to be long enough to touch the electrodes, but not too long to interfere with the surrounding circuits.

The unsupported methods (Laser, Arc and HiPCO) generally tend to produce longer tubes than the supported ones. This is due to the effect of the morphology of the porous supports on the growth of the SWNT. When the pore ends or suddenly changes direction, the SWNT growth is hindered and because of the lack of free space it stops. The SWNT produced generally by CoMoCAT® method have an average length distribution around 1 µm. However, because the problem is the geometry of the system, an engineered support without pores (like a flat surface) can solve it. When the CoMo solution is deposited onto the silica passivation layer of a Si wafer, the resulting SWNT tend to grow vertically from the surface, forming a sort of forest of SWNT (Figure 2.6). In this case, it is possible to reach lengths up to 80 µm.

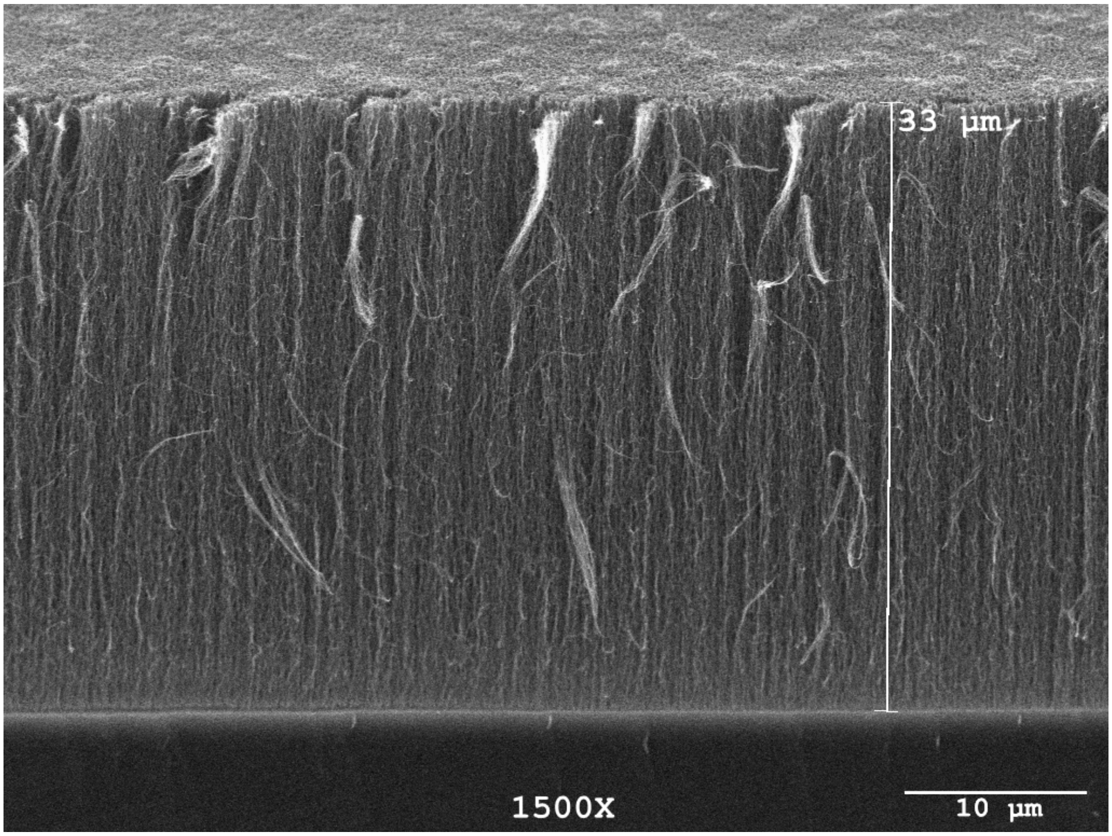

Figure 2.6 Vertically aligned SWNT produced by CoMo supported on silicon wafer.

Many other groups have developed the ability to grow this super long SWNT, [49] even up to 2 mm in length using a method called “Super Growth” [50], but all of them share the principle of using a flat surface, demonstrating that the constraint placed by the support is critical in limiting the growth.

2.4. Conclusions

As we have seen, the most common SWNT production methods involve a metal (Co, Ni, Fe) that belongs to group VIII and present a similar chemistry with the ability of dissolving large amounts of C in its lattice structure. All the methods have the necessity to control the particle size; in the Laser and HiPCO process this is done by controlling the physical process of diffusion and condensation, while in the case of CoMoCAT® this is done by controlling the chemistry of the catalyst.

The mechanism of CoMoCAT® has been supported in the past years by several publications [1-5] in which we demonstrated, using techniques like XANES/EXAFS, XPS and UV-Vis/DRS, the presence of an initial $CoMoO_4$-like structure and a final mixture of Mo_2C and metallic Co clusers (Figure 2.7). The stabilizing agent Mo can be substituted by other similar metals like W or Re [51,52], but in this case, the reduction temperature to activate the metals is much higher than in the case of Mo and it results in a less practical catalyst for production of SWNT. To further demonstrate the role of Mo as stabilizing agent and how critical the interaction is between Co and Mo, the complex was destabilized by the addition of external ions like Na. With the addition of Na, the Molybdenum tends to form the more stable Na_2MoO_4, leaving the Co segregated. This results in a non selective catalyst towards SWNT (Figure 2.8) [53]

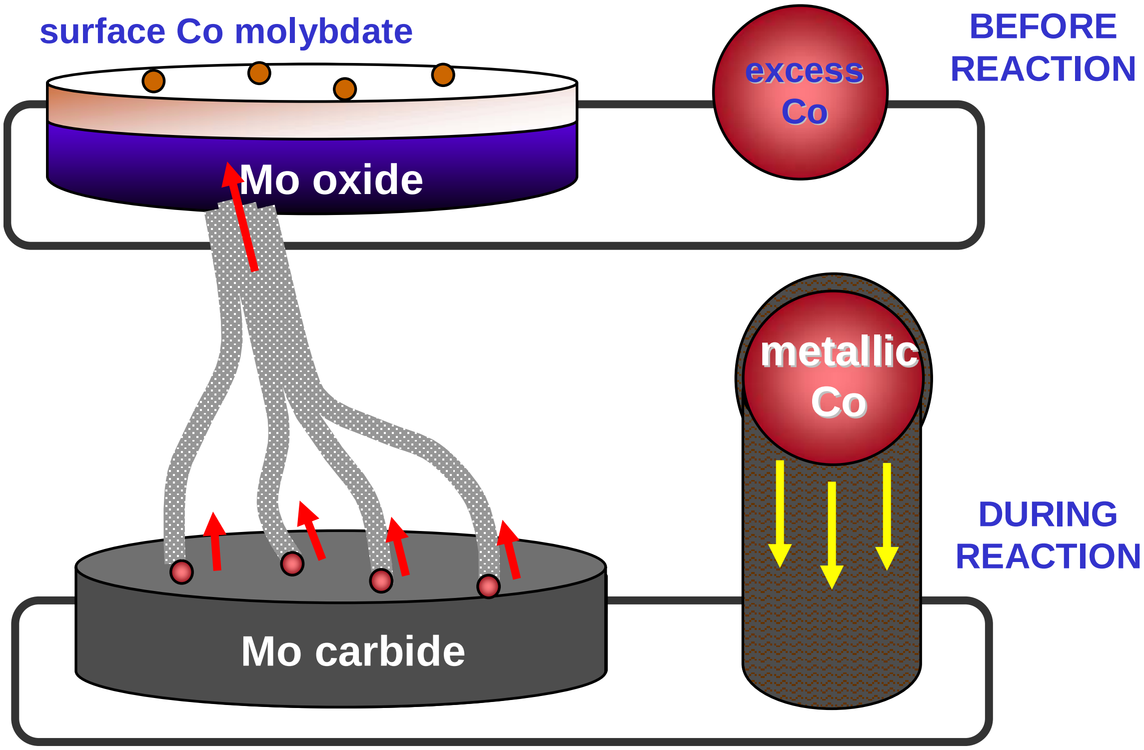

Figure 2.7 cartoon showing the mechanism of CoMoCAT®. The small Co particles generated on $CoMoO_4$ produce SWNT (left) while the large Co particles generated by segregated Co_2O_3 produce fibers or MWNT. [courtesy of Jose Herrera]

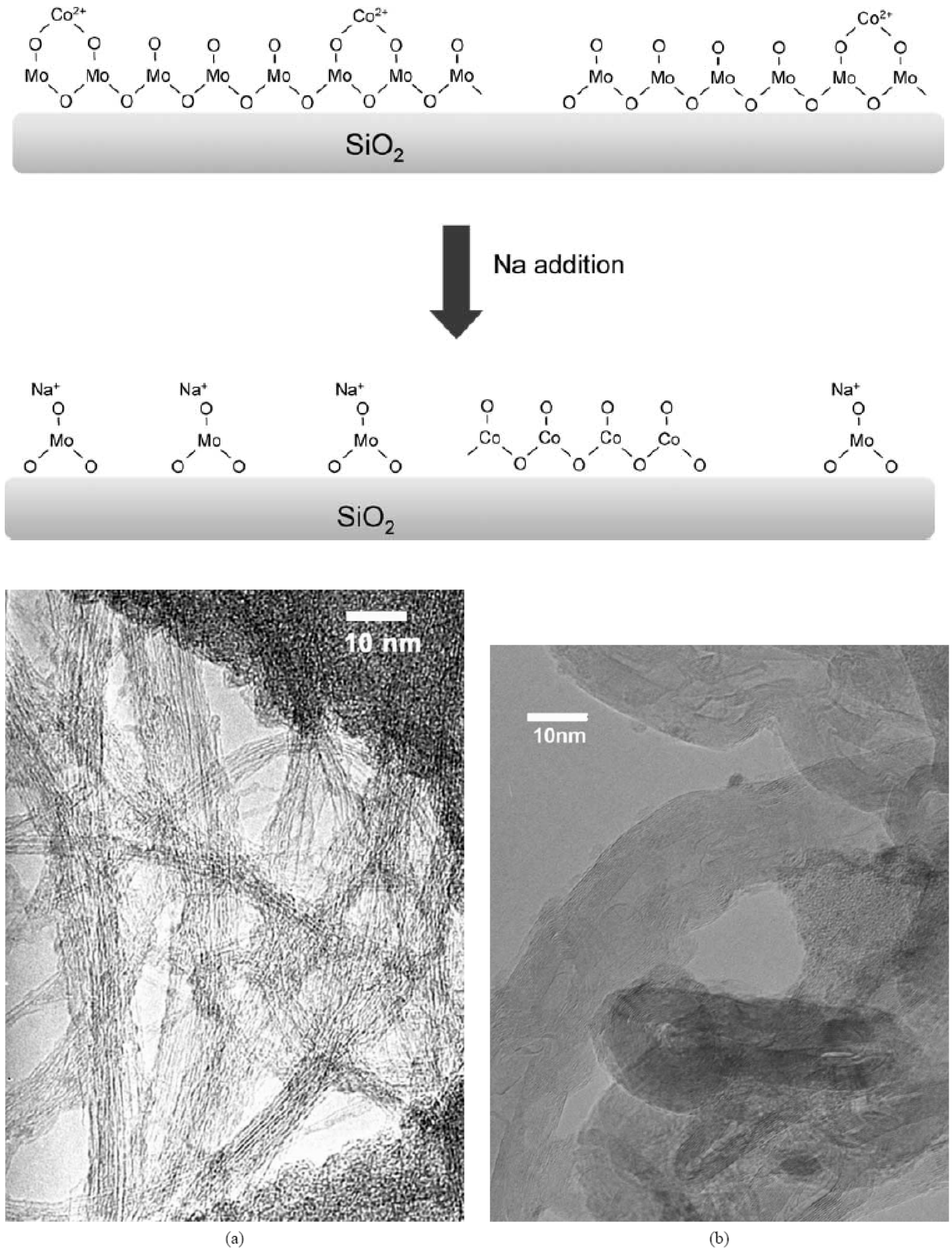

(a) (b)

Figure 2.8 Comparison of the material produced: a) without the addition of Na; b) with the addition of 4% Na. The sodium disrupt the interaction between the Co and Mo as shown on top.

All these studies have been done “post mortem” on the spent catalyst, while the most critical step is the initial contact with CO, when the oxide decomposition and the nucleation of the SWNT happen. The ability of studying and controlling this step is fundamental to control the intimate structure, like the (n,m) chiral vector, of the SWNT and to understand the kinetic of growth of SWNT. This is particularly important for trying to reach in production a high selectivity towards a specific (n,m) SWNT or a specific kind (metallic or semiconducting) for a targeted application.

Reference:

1 B. Kitiyanan, W.E. Alvarez, J.H. Harwell, D.E. Resasco *Chemical Physics Letters* **2000** 317, 497-503.

2 W.E. Alvarez, B. Kitiyanan, A. Borgna, D.E. Resasco *Carbon* **2001** 39, 547-558.

3 J.E. Herrera, L. Balzano, A. Borgna, W.E. Alvarez, D.E. Resasco *Journal of Catalysis* **2001** 204, 129-145.

4 D.E. Resasco, W.E. Alvarez, F. Pompeo, L. Balzano, J.E. Herrera, B. Kitiyanan, A. Borgna *Journal of Nanoparticle Research* **2002** 4, 131-136.

5 W.E. Alvarez, F. Pompeo, J.E. Herrera, L. Balzano, D.E. Resasco *Chemistry of Materials* **2002** 14, 1853-1858.

6 S.M. Bachilo, L. Balzano, J.E. Herrera, F. Pompeo, D.E. Resasco, R.B. Weisman *Journal of the American Chemical Society* **2003** 125, 11186-11187.

7 R.T.K. Baker, M.A. Barber, P.S. Harris, F.S. Feates, R.J. Waite *Journal of Catalysis* **1996** 26, 51.

8 S. Amelinckx, X.B. Zhang, D. Bernaerts, X.F. Zhang, V. Ivanov, J.B. Nagy *Science* **1994** 265, 635.

9 S. Fan, M. G. Chapline, N. R. Franklin, T. W. Tombler, A. M. Cassell, H. Dai *Science* **1999** 283, 512.

10 A.M. Morales, C.M. Lieber *Science* **1998** 279, 208.

11 J. Gavillet, A. Loiseau, C. Journet, F. Willaime, F. Ducastelle, J.-C. Charlier, *Physical Review Letters* **2001** 87, 275504.

12 M. Yudasaka, Y. Kasuya, M. Takizawa, S. Bandow, K. Takahashi, F. Kokai, S. Iijima *AIP Conference Proceedings* **2000** 544, 217.

13 R.S. Wagner, W.C. Ellis *Applied Physics Letters* **1964** 4, 89.

14 R.S. Wagner, W.C. Ellis, *Trans. Met. Soc. AIME* **1965** 233, 1053.

15 R. S. Wagner *Whisker Technology* **1970** Wiley-Interscience.

16 Y. Wu, P. Yang Journal of the American Chemical Society **2001** 123, 3165.

17 F. Rohmund, L.K.L. Falk, E.E.B. Campbell *AIP Conference Proceedings* **2000** 544, 234.

18 A. Martinez-Limia, J. Zhao, P. B. Balbuena, *Journal of Molecular Modeling* **2007** 13, 595-600.

19 P.B. Balbuena, J. Zhao, S. Huang, Y. Wang, N. Sakulchaicharoen, D.E. Resasco *Journal of Nanoscience and Nanotechnology* **2006** 6, 1247-1258.

20 J. Zhao, P. B. Balbuena *Journal of Physical Chemistry A* **2006** 110, 2771-2775.

21 F. Ding, A. Rosén, K. Bolton *The Journal of Chemical Physics* **2004** 121(6), 2775-2779.

22 C. N. R. Rao, G. U. Kulkarni, A. Govindaraj, B. C. Satishkumar, P. John Thomas *Pure and Applied Chemistry* **2000** 72(1–2), 21–33.

23 T.W. Ebbesen, P.M. Ajayan *Nature* **1992** 358, 220-222

24 C. Journet, P. Bernier *Applied Physics A-Materials Science & Processing* **1998** 67(1)**,** 1-9.

25 T. Guo, P. Nikolaev, A. Thess, D.T. Colbert, R.E. Smalley *Chemical Physics Letters* **1995** 243(1,2), 49-54.

26 M. Yudasaka, R. Yamada, N. Sensui, T. Wilkins, T. Ichihashi, S. Iijima *Journal of Physical Chemistry B* **1999** 103(30), 6224-6229.

27 P.C. Eklund, B.K. Pradhan, U.J. Kim, Q. Xiong, J.E. Fischer, A.D. Friedman, B.C. Holloway, K. Jordan, M.W. Smith *Nano Letters* **2002** 2(6), 561-566.

28 W.K. Maser, E. Munoz, A.M. Benito, M.T. Martinez, G.F. de la Fuente, Y. Maniette, E. Anglaret, J.L. Sauvajol *Chemical Physics Letters* **1998** 292(4-6), 587.

29 A.P. Bolshakov, S.A. Uglov, A.V. Saveliev, V.I. Konov, A.A. Gorbunov, W. Pompe, A. Graff *Diamond and Related Materials* **2002** 11(3-6), 927-930.

30 P. Nikolaev, M.J. Bronikowski, R.K. Bradley, F. Rohmund, D.T. Colbert, K.A. Smith, R.E. Smalley, *Chemical Physics Letters* **1999** 313(1,2), 91-97.

31 R.E. Smalley, B.I. Yakobson *Solid State Communications* **1998** 107(11), 597-606.

32 M.J. Bronikowski, P.A. Willis, D.T. Colbert, K.A. Smith, R.E. Smalley *Journal of Vacuum Science & Technology, A: Vacuum, Surfaces, and Films* **2001** 19(4, Pt. 2), 1800-1805.

33 Y. Yang, J.D. York, J. Xu, S. Lim, Y. Chen, G.L. Haller *Microporous and Mesoporous Materials* **2005** 86(1-3), 303-313.

34 Y. Chen, D. Ciuparu, S. Lim, G.L. Haller, L.D. Pfefferle *Carbon* **2005** 44(1), 67-78.

35 Y. Chen, D. Ciuparu, Y. Yang, S. Lim, C. Wang, G.L. Haller, L.D. Pfefferle *Nanotechnology* **2005** 16(7), 476-483.

36 D. Ciuparu, Y. Chen, S. Lim, Y. Yang, G.L. Haller, L.D. Pfefferle *Journal of Physical Chemistry B* **2004** 108(40), 15565-15571.

37 T. Somanathan, A. Pandurangan, D. Sathiyamoorthy *Journal of Molecular Catalysis A: Chemical* **2006** 256(1-2), 193-199.

38 Q. Wen, W. Qian, F. Wei, Y. Liu, G. Ning,Q. Zhang *Chemistry of Materials* **2007** 19(6), 1226-1230.

39 Y. Wang, Y. Liu, D. Wei, L.C. Cao, L. Fu, X.L. Li, H. Kajiura, Y.M. Li, K. Noda *Journal of Materials Chemistry* **2007** 17(4), 357-363.

40 G. Lolli, L. Zhang, L. Balzano, N. Sakulchaicharoen, Y. Tan, D.E. Resasco *Journal of Physical Chemistry B* **2006** 110(5), 2108-2115.

41 L. Zhang, L. Balzano, D.E. Resasco *Journal of Physical Chemistry B* **2005** 109(30), 14375-14381.

42 H.R. Byon, H.C. Choi *Journal of the American Chemical Society* **2006** 128(7), 2188-2189.

43 S.N. Kim, Z. Luo, F. Papadimitrakopoulos *Nano Letters* **2005** 5(12), 2500-2504.

44 M.S. Arnold, S.I. Stupp, M.C. Hersam *Nano Letters* **2005** 5(4), 713-718.

45 S.R. Lustig, A. Jagota, C. Khripin, M. Zheng *Journal of Physical Chemistry B* **2005** 109(7), 2559-2566.

46 Y. Maeda, S. Kimura,M. Kanda, Y. Hirashima, T. Hasegawa, T. Wakahara, Y. Lian, T. Nakahodo, T. Tsuchiya, T. Akasaka, J. Lu, X. Zhang, Z. Gao, Y. Yu, S. Nagase, S. Kazaoui, N. Minami, T. Shimizu, H. Tokumoto, R. Saito *Journal of the American Chemical Society* **2005** 127(29), 10287-10290.

47 M.S. Arnold, A.A. Green, J.F. Hulvat, S.I. Stupp, M.C. Hersam, *Nature Nanotecnology* **2006** 1, 60.

48 Z. Gu,H. Peng, R.H. Hauge, R.E. Smalley, J.L. Margrave *Nano Letters* **2002** 2(9), 1009-1013.

49 L. Zhang, Z. Li, Y. Tan, G. Lolli, N. Sakulchaicharoen, F.G. Requejo, B.S. Mun, D.E. Resasco *Chemistry of Materials* **2006** 18(23), 5624-5629.

50 S. Noda, K. Hasegawa, H. Sugime, K. Kakehi, Z. Zhang, S. Maruyama, Y. Yamaguchi *Los Alamos National Laboratory, Preprint Archive, Condensed Matter* **2007** 1-11, arXiv:0704.0915v1

51 J.E. Herrera, D.E. Resasco *Journal of Physical Chemistry B* **2003** 107, 3738-3746.

52 P. Chungchamroenkit, B. Kitiyanan, J.E. Herrera, S. Chavadej, D.E. Resasco *Diffusion and Defect Data--Solid State Data, Pt. B: Solid State Phenomena* **2007** 121-123(Pt. 1, Nanoscience and Technology, Part 1), 337-341.

53 J.E. Herrera, D.E. Resasco. *Journal of Catalysis* **2004** 221, 354-364.

CHAPTER 3

3. Physical-Chemical Characterization of the Catalyst

3.1. Preparation of the catalyst

The catalyst was prepared by incipient wetness co-impregnation of an aqueous solution containing the proper amount of $Co(NO_3)_2 \cdot 6H_2O$ and $(NH_4)_6Mo_7O_{24} \cdot 7H_2O$ over a high surface area porous silica support. All the previous studies were conducted using SiGel (Alfa Aesar) as support. [1-5] In this chapter, we will compare this preparation with another type of silica support: precipitated silica (HiSil 210 from PPG) that has a different surface morphology and chemistry due to the different preparation method. In the incipient wetness impregnation only the amount of liquid necessary to fill the pores of the support is used: this insures no over-wetness that results in a not-homogeneous product. A typical catalyst composition is 1:3 Co:Mo molar ratio with a 2 wt% metal loading.

Even if different ratios and loadings can be used, we have chosen 1:3 as a basic composition because it is more conservative in terms of the required properties of the catalyst. A higher Co:Mo ratio reduces the chance to have a good interaction with the MoO_3 framework: a perfect 1:1 ratio (like in $CoMoO_4$) may not necessarily result in 100% cobalt-molybdate structure, but will present a fraction of CoO or

Co_3O_4 that will be unselective towards SWNT; having a highly sub-stochiometric ratio (like 1:3) ensures that the amount of isolated cobalt oxide is minimized.

As the ratio determines the chemical structure of the system, the loading determines the physical structure. A low metal loading results in high dispersion of the oxidic phase, while a higher loading will result in a coarser dispersion. If the domains of $CoMoO_4$ are too big, the Co, once released, will quickly aggregate in large particles and will be no longer selective towards SWNT. For example, considering a surface occupation for a MoO_3 monolayer of 0.196 nm^2/Mo [6], in a 2 wt% catalyst, the surface occupied by the MoO_3 will be ideally 24 m^2/g. For that result, the MoO_3 should be very dispersed on the high surface area silica gel (500 m^2/g) as well as on the lower surface area precipitated silica (150 m^2/g). A higher metal loading (e.g. 6 wt%) results in poorer dispersion on the low surface area support.

Once impregnated, the support was dried of the excess liquid in an air convection oven at 110°C for at least 12 hours and then calcined at 500°C for 3 hours. During this final step, the nitrogen-containing precursors decompose and generate the wanted metal oxides.

3.2. Phase evolution during reaction

The catalyst in the oxidic form is inactive towards the production of SWNT. As we discussed before, to generate carbon structures, a metal such Co, Ni or Fe should be present in the reduced metallic form. In the case of CoMoCAT® the activation is completed "in-situ" only during the growth of SWNT. However the catalyst has to be pre-activated with a partial reduction and subsequently completely reduced in presence of CO. [1,2,4,5] During this process it undergoes a series of physical-chemical transformations that are responsible for the formation of the right surface structures. If the ultimate goal is the tailoring of the selectivity towards a specific (n,m) type, more than towards SWNT in general, a better understanding of that evolution is necessary.

A powerful tool to look at the phase composition is X-Ray diffraction. The resulting diffraction pattern can be matched with a crystal structure database [7] and the phases present can be identified. The analysis of the catalyst in the oxidized state (Figure 3.1) reveals indeed the presence of $CoMoO_4$. This is in agreement with the previous EXAFS data on the fresh catalyst [3,5] and with what is expected from the catalyst chemical composition. From a more detailed analysis of the XRD data it is also possible to estimate the average crystallite size of the $CoMoO_4$ domains using the Debye-Scherrer equation: the FWHM (full width at half maximum) is inversely proportional to the crystallite size. [8] In this case, as can be clearly seen from the weak and broad pattern obtained, the crystallites are extremely small and estimated to be around 22 nm (table 3.1). However we need to carefully consider that the Scherrer equation is affected by an error up to 50% and that XRD sensitivity is enhanced for larger crystallites. For this, we can conservatively say that the distribution is smaller than the values shown in table 3.1.

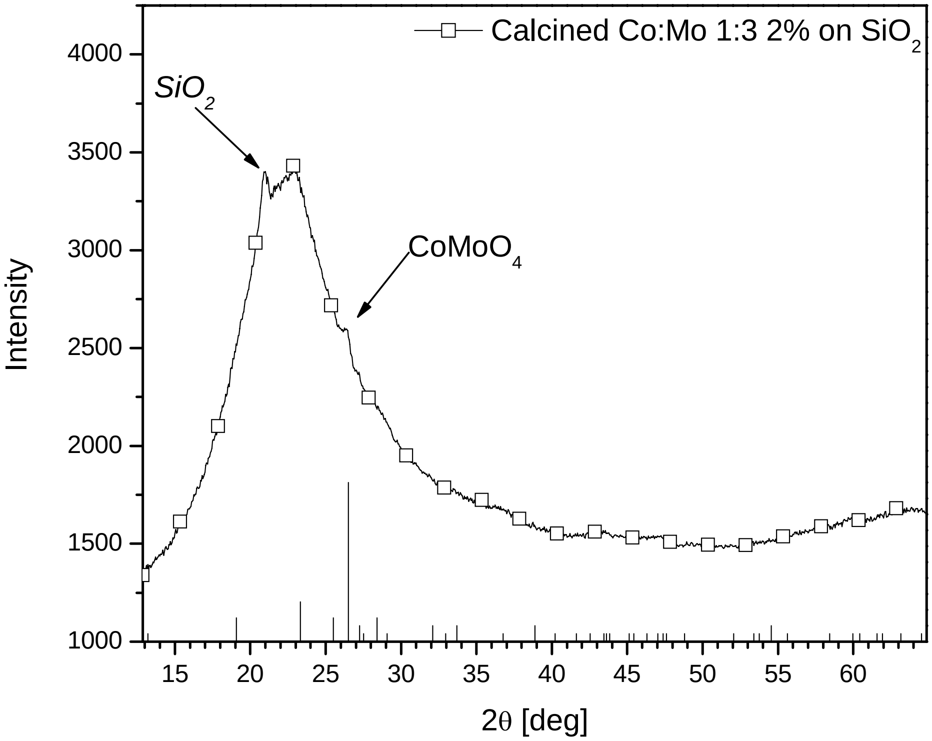

Figure 3.1 XRD spectra of the CoMoCAT® catalyst 1:3 Co:Mo molar ratio 2 wt%. The ideal pattern for $CoMoO_4$ [7] is included for comparison.

Crystallite Size (nm)

	Calcined	Pre-reaction 500°C H_2 750°C He	Reacted 750°C CO
$CoMoO_4$	21.7	–	–
MoO_2	–	22.9	–
Mo_2C	–	–	8.6
Co	–	–	7.4

Table 3.1 Estimated crystallite sizes from X-ray diffraction of several species present in the catalyst during its lifetime.

More interesting than the initial state of the catalyst is the evolution it undergoes during the pretreatment in hydrogen at 500ºC (Figure 3.2 and 3.3). After the pretreatment, all the XRD features disappear, suggesting a partial loss of the crystalline structure. However, after the subsequent heating in He, some features reappear due to a reorganization of the crystalline domains. These features are attributed to MoO_2, a partially reduced form of molybdenum oxide. This suggests that the Co^{2+} ions, which before reduction were distributed homogeneously in the $CoMoO_4$-like structure, now segregate in very small domains, invisible to XRD, leaving the excess Mo as a sub-oxidic form.

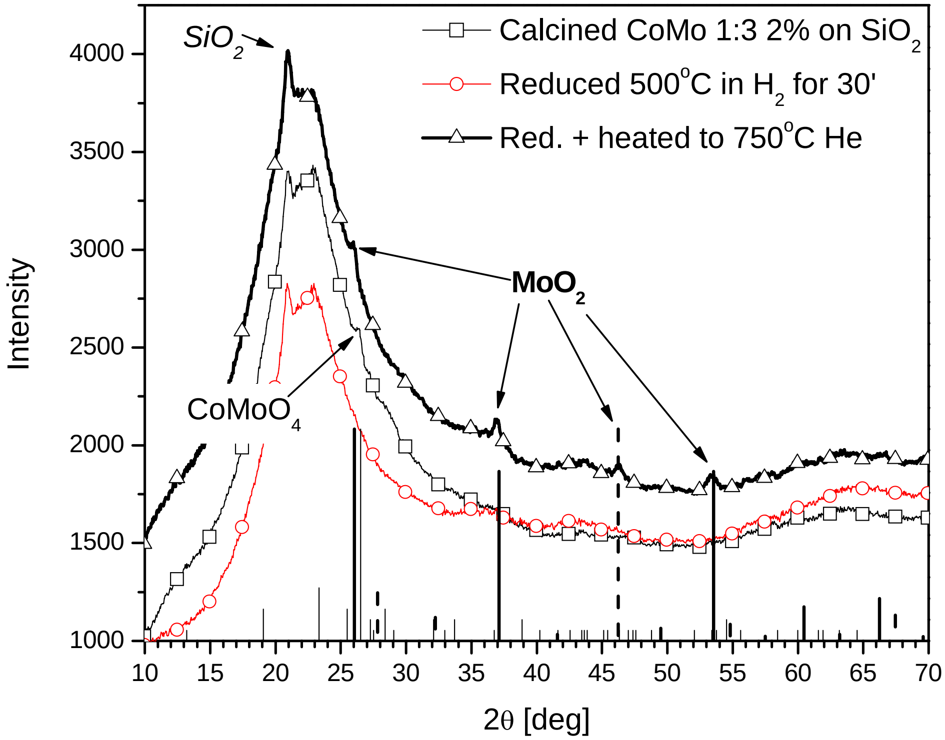

Figure 3.2 XRD spectra of the catalyst during its lifetime. The XRD patterns for $CoMoO_4$ (thin bars), and 2 forms of MoO_2 (thick bars full and dashed) are included for comparison.

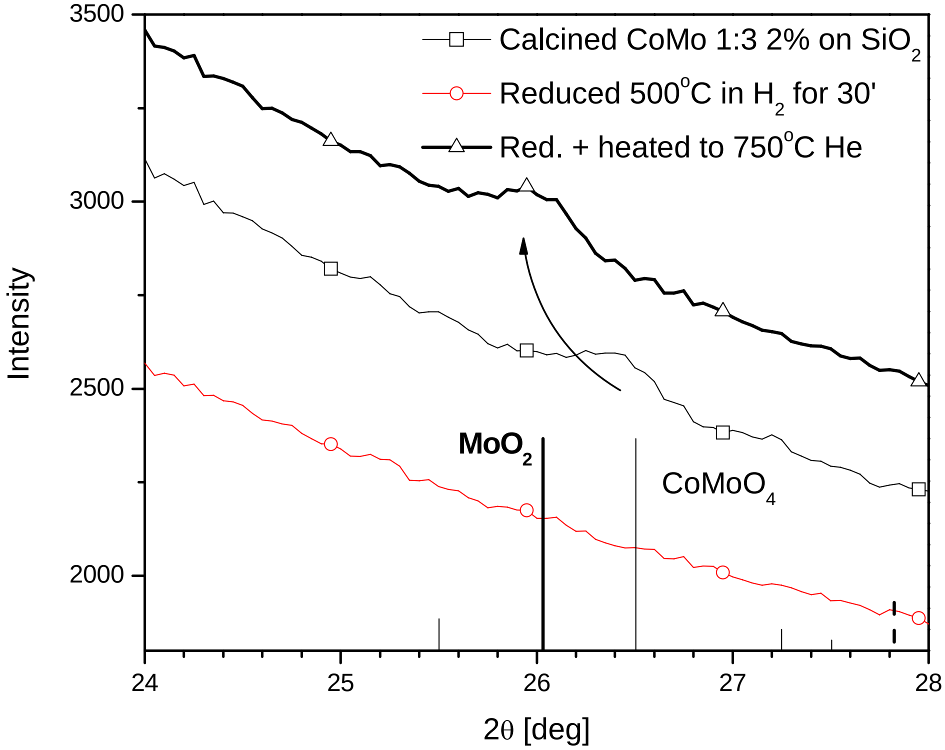

Figure 3.3 Particular of Figure 3.2. The transition between $CoMoO_4$ and MoO_2 after reduction and heating is marked by an arrow.

This picture is a refinement of the model developed previously [3] because, even when both models start from the same picture, the previous one didn't consider the importance of the domain size. The present model takes into account that the initial catalyst presents a well dispersed $CoMoO_4$ structure, but the size of these domains is still too big to be selective towards SWNT. During the pre-reduction, the dual oxide is attacked and looses its crystallinity, but after heating, it recovers it in the form of domains of MoO_2, similar in size to the starting $CoMoO_4$ (see table 3.1), that are probably decorated with very small areas, richer in Co. This oxidized Co that decorates the surface of the MoO_2 clusters is probably responsible for the release of the metallic form after contacting with CO. Interestingly this is similar to what happens in the CoMo system after sulfidation [9,10], with the Co atoms that decorate the edges of the moly sulfide sandwich structure.

When these small domains of $CoMoO_4$ are contacted with CO, another chemical attack happens: the excess MoO_2 is converted, at least partially, in Mo_2C, and the Co is released and reduced to metallic Co (Figure 3.4). The size of the resulting crystals is several times smaller than the ones on the initial catalyst. These crystals result in nm-size metallic clusters that are responsible for the selective growth of SWNT.

In summary, there are two critical steps in the pretreatment of the catalyst: the pre-reduction that destroys the large crystallinity of the $CoMoO_4$ domains and the following reorganization of the surface, producing MoO_2 domains decorated with Co ions. This mechanism shows how critical the pre-reduction step can be, but also suggests that other variables can have an important role. Among them, the underlying support is probably the morst critical. The support, through the metal-support interaction [11-13], can change the temperature needed for reduction and alter the way the system reorganizes afterwards.

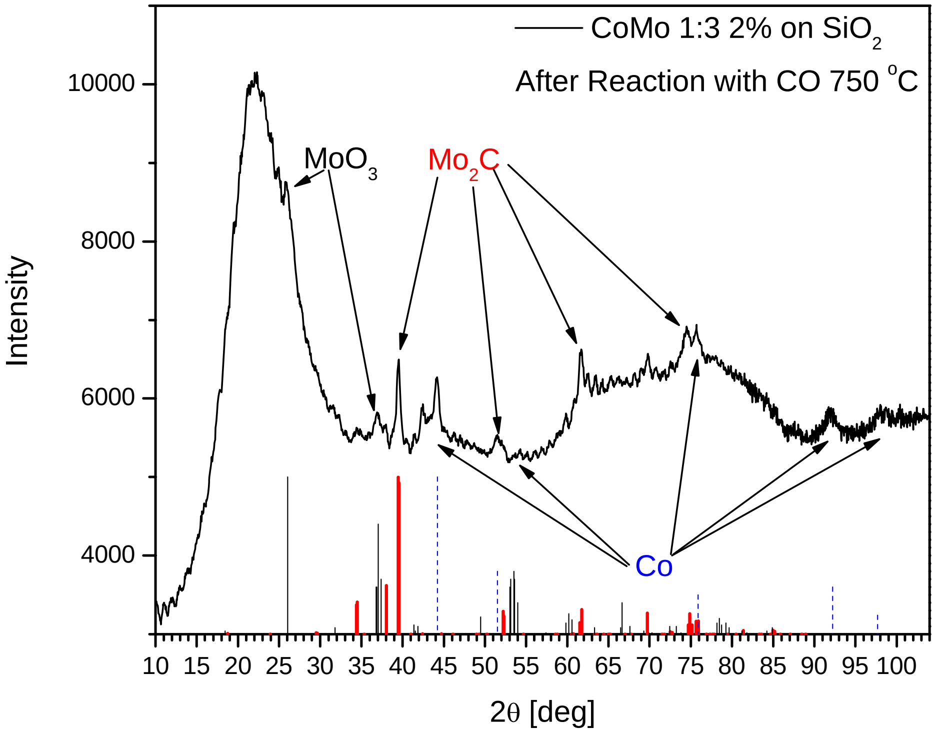

Figure 3.4 XRD spectra of the material obtained after reaction with CO. The patterns for MoO_3 (black), Mo_2C (red) and metallic Co (blue dash) are included for comparison.

3.3. Role of the pre-reduction

3.3.1 NO adsorption

As we have seen above, the pre-reduction is a critical step in changing the microstructure of the surface exposed. A very powerful method to study the chemistry of the external surface of a catalyst is the use of a probe molecule. In general, in this technique, a gas is chemisorbed onto the catalyst. The IR vibration feature changes from the one of the molecule in the gas phase and depends on the interaction with the absorbing site. In the case of Co/Mo system this technique has been widely employed in the study of HDS catalyst using NO adsorption. [14,15] In this case, the formation of a dinitrosyl complex is responsible for the IR features. Two different modes are seen corresponding to the symmetric and the anti-symmetric stretching of two Me-NO bonds. In particular, as seen on Figure 3.5, Co shows vibrations at 1,870 and 1,800 cm^{-1} and Mo at 1,800 and 1,690 cm^{-1}, corresponding respectively to the symmetric (higher frequency) and anti-symmetric (lower frequency) stretching.

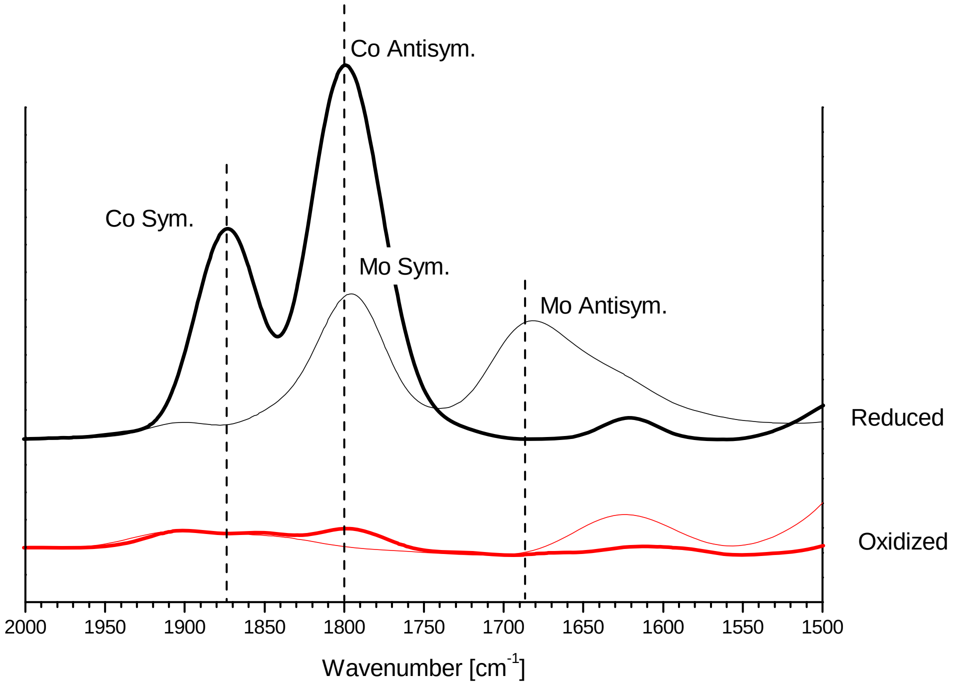

Figure 3.5 FTIR spectra of NO molecules absorbed onto monometallic Co (thin line) or Mo (bold line) on SiO_2. Evidenced is the difference between oxidized (red) and after reduction at 500°C in H_2 (black)

The NO absorption depends also on the chemistry of the metal site: not all the oxidation states of Co and Mo can coordinate with NO. In particular, Co^{3+} is not able to coordinate NO while Co^{2+} or Co^0 can. [16,17] In the case of Mo, all the oxidation states can coordinate NO, but the intensity of the resulting bands increases in the following order: $Mo^{6+} < Mo^{4+} \cong Mo^{2+} << Mo^{0}$. However, in the case of oxidized Mo we have to consider that at least one oxygen vacancy had to be present to allow access of the NO molecule to the Mo site.

Now, it is easy to explain the monometallic systems (Figure 3.5): Co on silica is in the form of Co_3O_4 that has a spinel structure with Co^{2+} ions inside the tetrahedral vacancies far from the surface of the crystal. When it is oxidized, Co_3O_4 presents weak or almost negligible absorption because the majority of exposed Co sites are Co^{3+}. However, after a mild reduction, the Co^{3+} sites are replaced by Co^{2+} or even metallic Co^{0}, which present strong adsorption capacity. In the case of Mo, the initial structure is MoO_3 without oxygen vacancies. The signal from Mo starts appearing as soon as some vacancies are produced in the lattice structure, even if the metal is still oxidized.

In the case of the bimetallic catalyst on SiGel (Figure 3.6), when both metals are present at the same time and interacting, we can see that neither Co or Mo are exposed at a reduction temperature below 400°C. After reducing at 500°C, Co appears, but still the signal from Mo is almost absent. This signal increases only after 600°C.

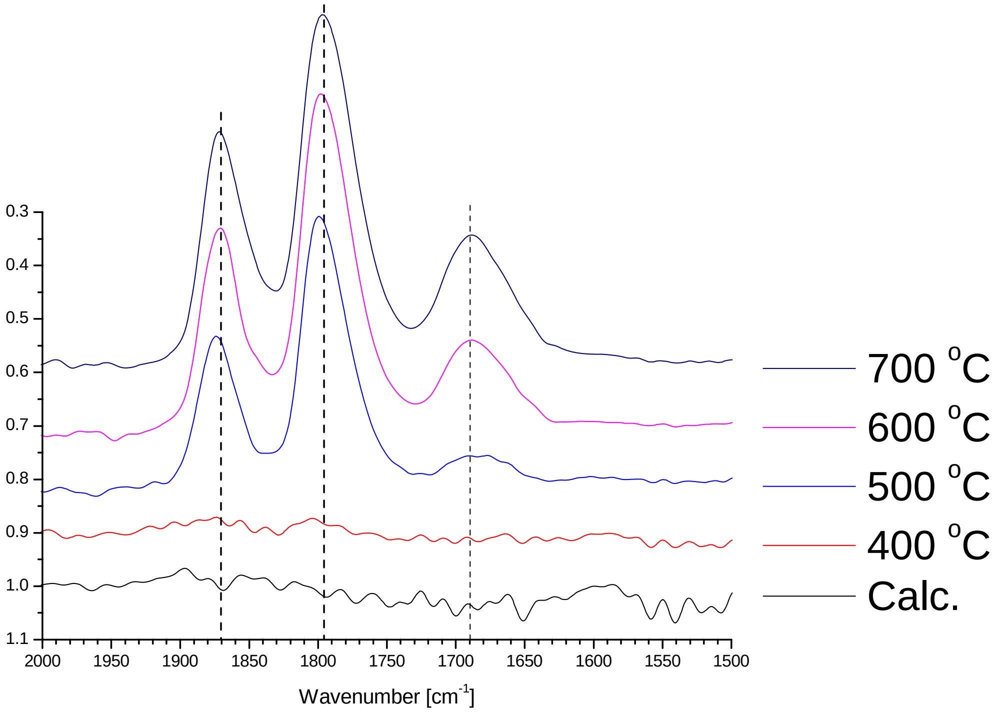

Figure 3.6 FTIR spectra of NO absorbed on bimetallic CoMo supported on SiGel. The increasing reduction temperature in H_2 is shown on the right side.

3.3.2. TPR

The results from NO adsorption are in agreement with the temperature programmed reduction of the catalyst. Figure 3.7 marks the reduction steps analyzed by NO adsorption. As we can see, below 400°C almost no reduction happens, leaving the catalyst basically unchanged when compared to the original calcined state. Between 400°C and 500°C a sharp reduction peak is present. From the NO absorption analysis, this is associated with a Co-rich phase that tends to segregate Co ions on the surface. The higher reduction phase is probably a Mo-rich phase. In this case, the Co released at lower temperature is free to sinter, while the higher temperature phase of Mo is basically inactive if not reduced.

The presence of two markedly different phases and chemical compositions is what, according to our model, we have to avoid in order to obtain high type I selectivity. This lack of selectivity can be attributed to the wrong metal-support interaction.

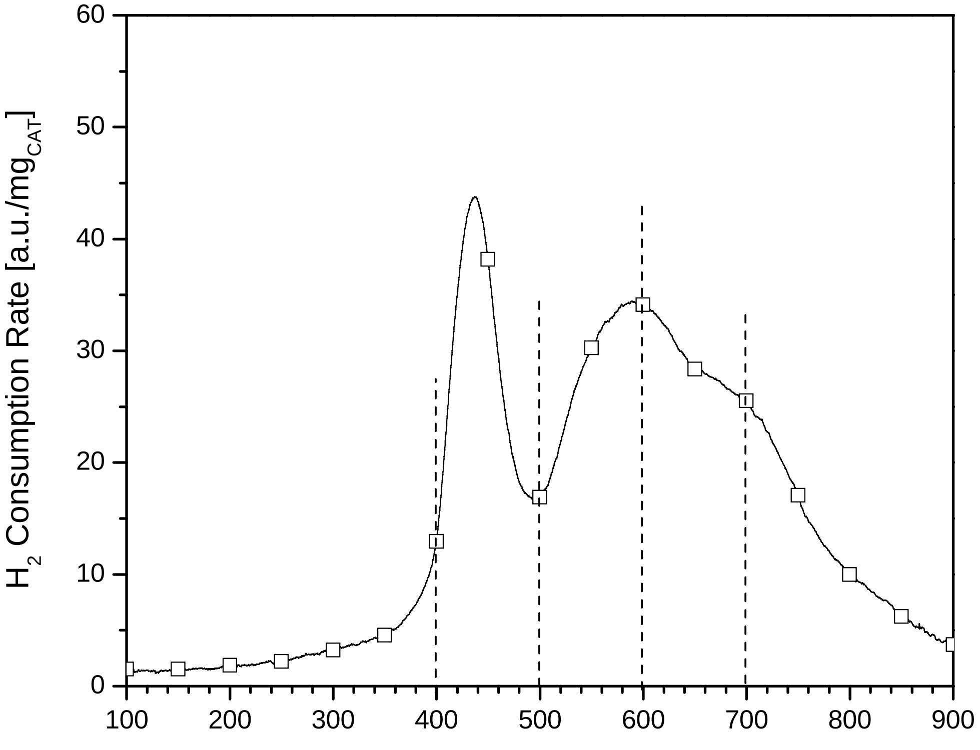

Figure 3.7 TPR (temperature programmed reduction) of the bimetallic catalyst supported on SiGel. The vertical lines are the reduction temperatures analyzed in Figure 3.6.

3.4. Role of the support

To further investigate the interaction of Co/Mo with the support, as introduced before, several different kinds of silica have been studied.

3.4.1. Morphology and chemistry of the support

The change of the silica support can have a double effect: a physical effect due to a change in morphology because of the different surface area or pore volume, and a chemical effect because of different surface reactivity. Even if both are important, probably the altered chemistry is the key aspect responsible for the different metal-support interaction. Two different silica supports were studied: Silica Gel (from Alfa Aesar) and precipitated silica (HiSil 210 from PPG). They differ in morphology as well as in chemistry. In particular, as we can see from table 3.2, Silica Gel has a higher surface area and a slightly smaller pore volume than HiSil, as is typical of micro-porous materials. However, the precipitated silica presents a higher density of OH surface groups and especially of active OH sites. These were measured using a method developed by Sears. [18] It is based on ion exchanging the proton with NaCl at pH 6.0. The developed HCl is then back-titrated using NaOH or KOH till pH 9.0.

	S.A. m^2/g	P.V. cm^3/g	Total -OH OH/nm^2	Exchangeable -OH OH/nm^2
SiGel	500	0.7	5.2	0.6
HiSil	150	1.1	19.7	1.5
D.H. HiSil	150	1.1	5.9	–

Table 3.2 Physical-chemical characteristics of the SiO_2 supports used

The increased number of OH groups (which make the surface more hydrophilic), especially the higher number of exchangeable sites, can increase the interaction with the metal oxides present. This effect is shown in Figure 3.8.

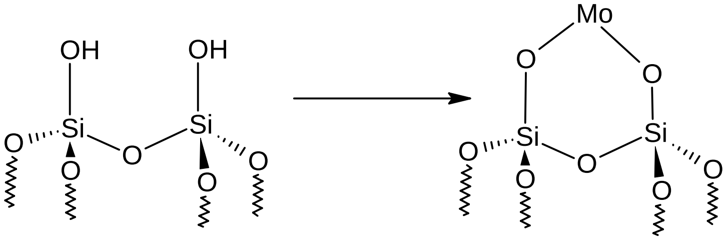

Figure 3.8 Bridging of the metal oxides to the support via condensation of a silanol group.

To further investigate the importance of surface chemistry versus morphology of the support, a de-hydroxilated version of HiSil was prepared by preheating the support to 500°C for 6 hours, removing the majority of the OH groups without altering the morphology. The comparison between the water desorption profiles of the three types of silica is shown in Figure 3.9 and the properties are summarized in table 3.2.

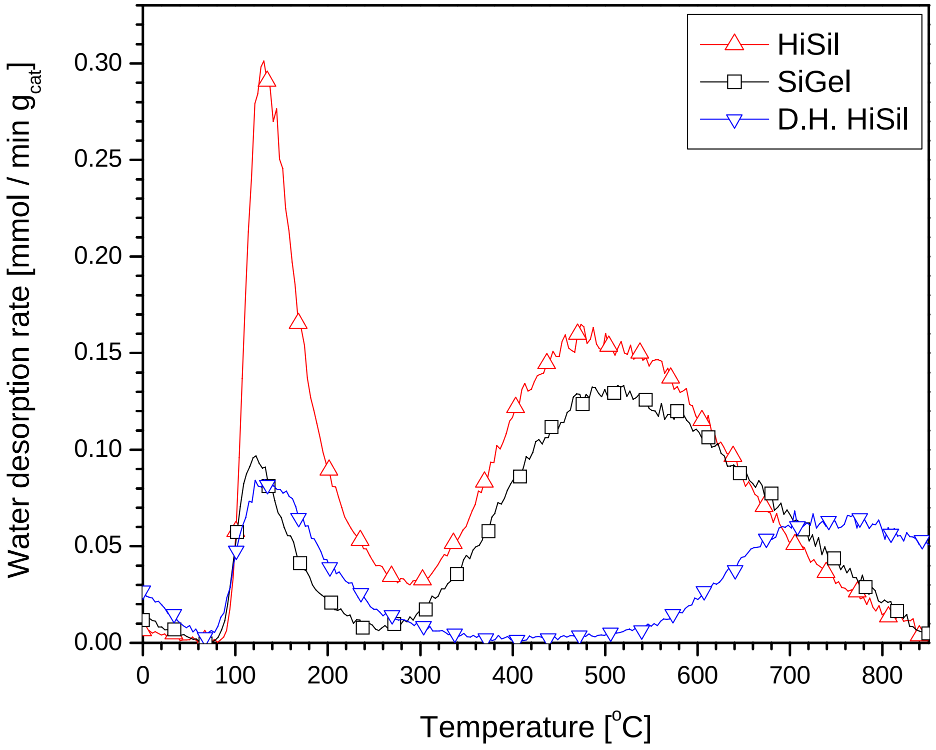

Figure 3.9 TPD (temperature programmed desorption) profile of the three different silica compared on table 3.2

The three different catalysts, equal in composition (1:3 Co:Mo 2wt%), will be denominated from now on SiGel, HiSil and D.H.Hisil.

3.4.2 TPR

The differences made by the various interactions with the support are extremely marked and clear from TPR (Figure 3.10). SiGel, as seen before, presents two distinct peaks attributed to a Co-rich phase and a Mo-rich phase. This is completely different from HiSil, where the profile is altered and shows a broad and unique peak centered around 550°C. This suggests the presence of a single phase, homogeneous in chemical composition. To understand if the variation is due to the different morphology of the support or to the different surface chemistry, the TPR of the de-hydroxilated silica is also shown in Figure 3.10. As we can see, the overall pattern for the TPR is similar to that of the fresh precipitated silica, even if the temperature is shifted up and the presence of a higher temperature shoulder is more marked. This suggests that the phase separation present in the silica-gel-supported catalyst is due to the chromatographic effects of enrichment of the ions present inside the support's micro-pores, acting as a liquid chromatography column.

The increased temperature of the D.H. HiSil supported catalyst may be due to a larger aggregate size. On the fresh HiSil, the high OH group density allows a better anchoring of the oxidic species and increases the dispersion. When the reduction temperature is too high, the $CoMoO_x$ phase is not activated for the subsequent reduction with CO. Moreover, an over-reduction in H_2 will increase the particle size due to sintering and release of metallic Co. Both effects result in an unselective catalyst.

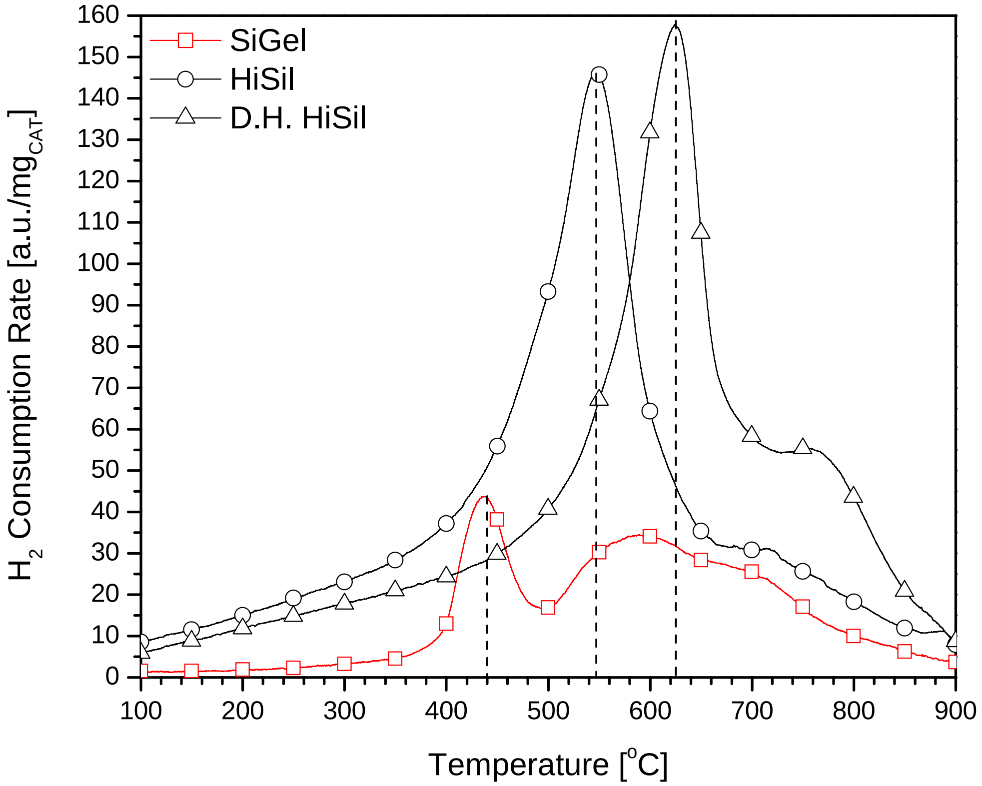

Figure 3.10 Comparison of the catalyst's TPR profile prepared on the three different silica.

To better understand the evolution of these phases, a series of "during-the-life" TPR were performed. As we can see from Figure 3.11, after a reduction at 500°C in hydrogen, the SiGel supported catalyst presents a lower temperature shoulder that does not recover after heating at high temperatures. This suggests that the earlier reducing Co-rich phase is prone to bleach out the extra Co^{2+} ions that can form Co oxide or even metal. The single-reduction peak of the HiSil supported catalyst, however, does not result in this segregation. Also, after being heated to high temperatures, the catalyst tends to form a higher temperature reduction peak (around 700°C). This is in agreement with the XRD data and can be attributed to MoO_2.

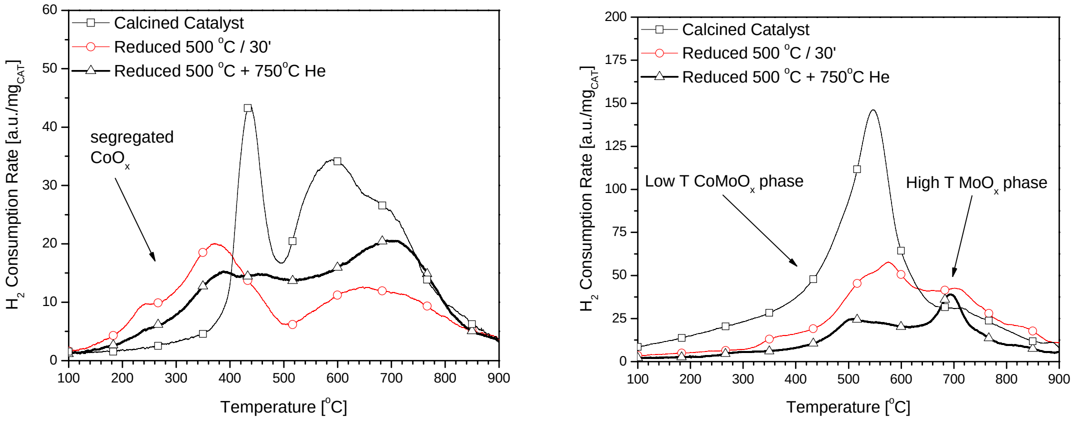

Figure 3.11 Evolution of the TPR profile after reduction in H_2 and reduction followed by heating in He. SiGel supported catalyst (left) and HiSil supported catalyst (right).

3.4.3. NO adsorption

The difference observed in TPR is also confirmed by NO adsorption. If we compare the spectra obtained on SiGel (Figure 3.6) with the ones obtained on precipitated silica (Figure 3.12), we can see that in the case of SiGel, at 500°C the majority of the Co was exposed or reduced and the Mo was still without oxygen vacancies. On HiSil, alternatively, Co and Mo tend to increase together above 500°C. This is, again, in agreement with the marked lines on Figure 3.7 and the presence of a single $CoMoO_4$-like phase.

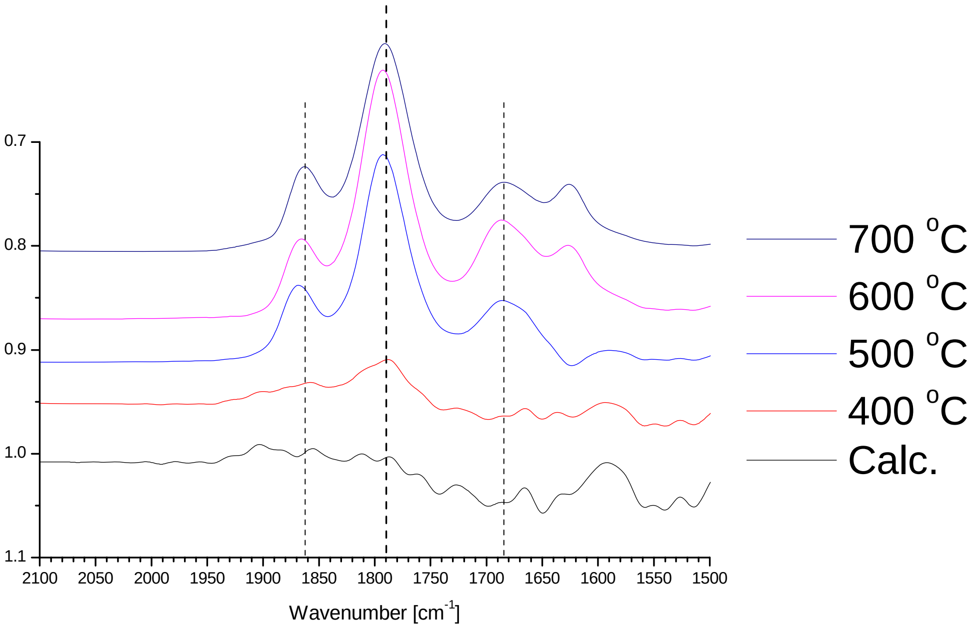

Figure 3.12 FTIR spectra of NO absorbed on bimetallic CoMo supported on HiSil. The increasing reduction temperature in H_2 is shown on the right side.

Other information, which can be extrapolated from the NO absorption, is the angle between the two vibrating molecules. This angle is determined by the simple geometrical summation (as vectors) of the two dipole moments of the molecules. [19] The intensity of each of the two modes (symmetrical and anti-symmetrical) is then proportional to the resulting overall dipole and can be summarized by the formula:

$$\frac{I_A}{I_S} = \tan^2\left(\theta/2\right) \qquad \textbf{Equation 3.1}$$

The schematics of the mechanism are summarized in Figure 3.13

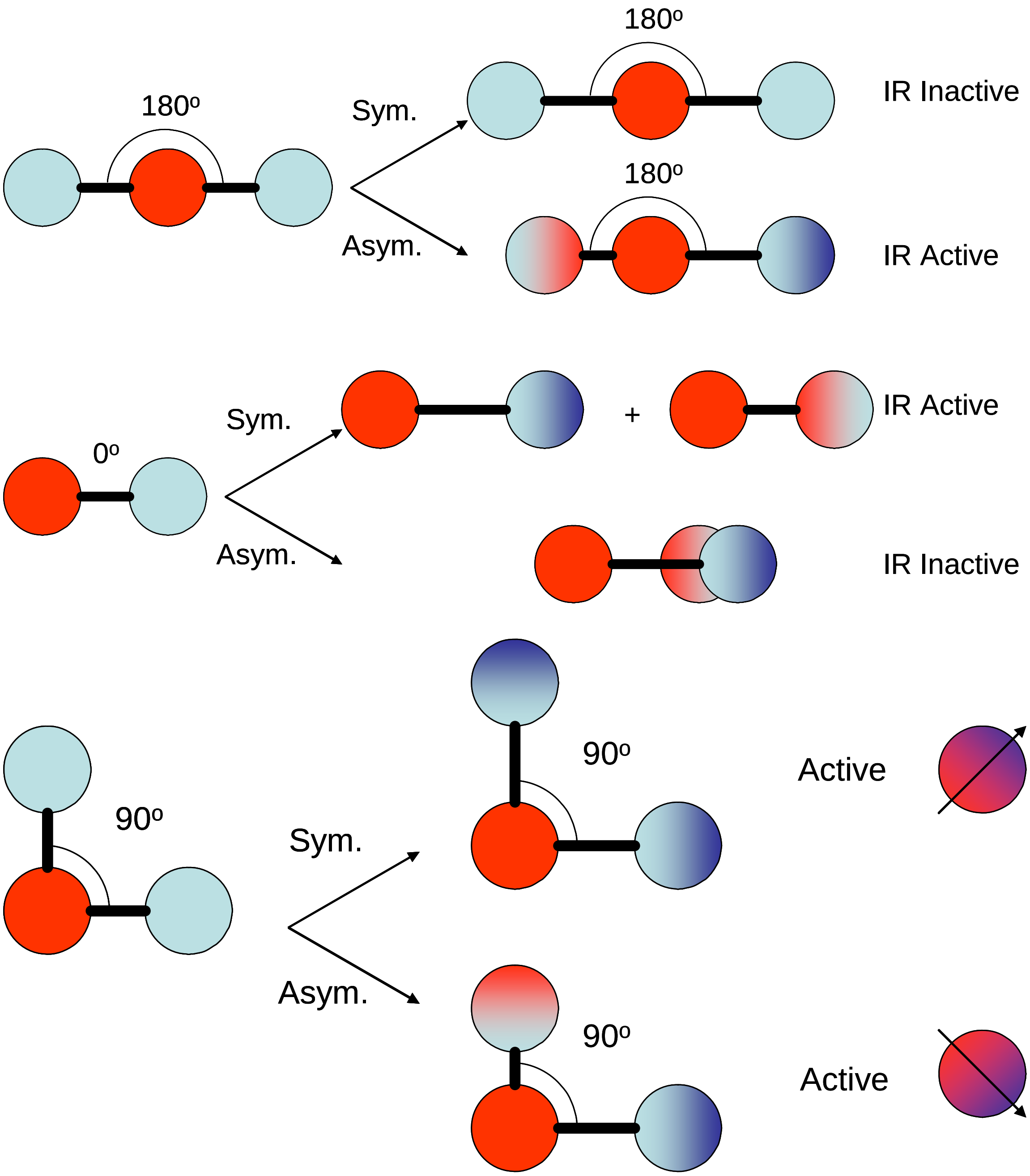

Figure 3.13 Dipole moments in function of the geometry of the 2 ligands. When the dipole moment is zero, the vibration is IR inactive. The stronger the dipole, the stronger the IR absorption. In red is highlighted the metal site while in blue the NO molecule. The resulting dipole moment is shown with an arrow.

The theoretical angle between the NO ligands depends on the hybridization of the unoccupied orbital of the metallic ions and the geometry of the crystalline lattice. In metal oxides, the configuration can be, typically, tetrahedral (109.5°) or octahedral (90°). In the presence of surrounding oxygen molecules these angles can become more acute due to the steric effect. The result is an angle that is slightly smaller than expected, but should get closer by increasing the extent of the reduction.

In the case of the CoMo system, being that the anti-symmetric band of Co is overlapped with the symmetric band of Mo, we have to assume the geometry associated with one of the two atoms (the ratio between its bands) to estimate the geometry of the other.

A good choice, for making this assumption, is (considering the spinel structure of $CoMoO_4$, with the Co^{2+} ions in the tetrahedral vacancies and Mo^{6+} ions in the octahedral vacancies of the FCC oxygen lattice) assuming the Co^{2+} in a tetrahedral environment. Specifically, a calculation was made using Co_3O_4 on silica, that has a similar spinel structure with the Co^{2+} ions (the only ions that can coordinate NO) in the tetrahedral vacancies. The calculation reveals that the angle between the NO molecules is 105° very close to the expected 109.5° (Figure 3.14). This experimental angle was chosen for the following fittings. The results obtained from the HiSil supported catalyst are in agreement with our expectations. The angle increases from around 78° at a low reduction to 86° at a higher reduction, getting closer to the expected 90° of the octahedral Mo (Figure 3.15). Interestingly, the same experiment, done on the monometallic Mo, shows an angle of around 79° after reduction at 500°C. This angle is similar to that of bimetallic catalyst and is in line with the expected structure for MoO_3; however, after reduction at 700°C, it drops to 74°, getting closer to the BCC structure of metallic Mo. This means that Co also helps to preserve the original crystalline structure, delaying the reduction of Mo.

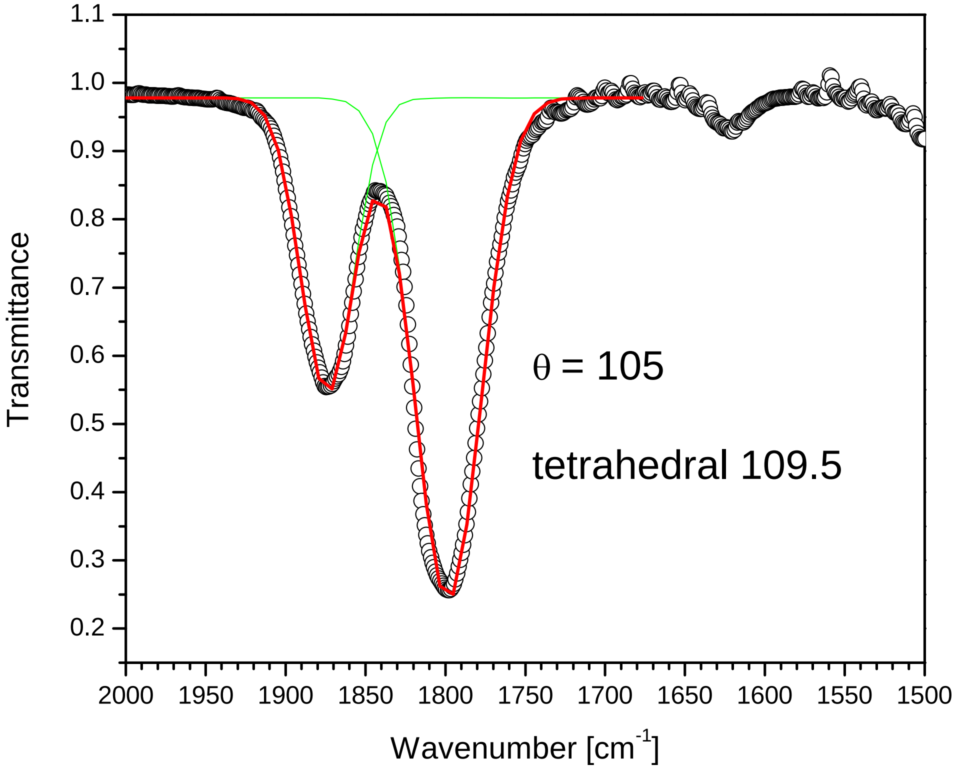

Figure 3.14 Fitting of the 2 bands of Co supported on silica. The calculated angle is 105º very close to the expected geometry for a tetrahedral configuration.

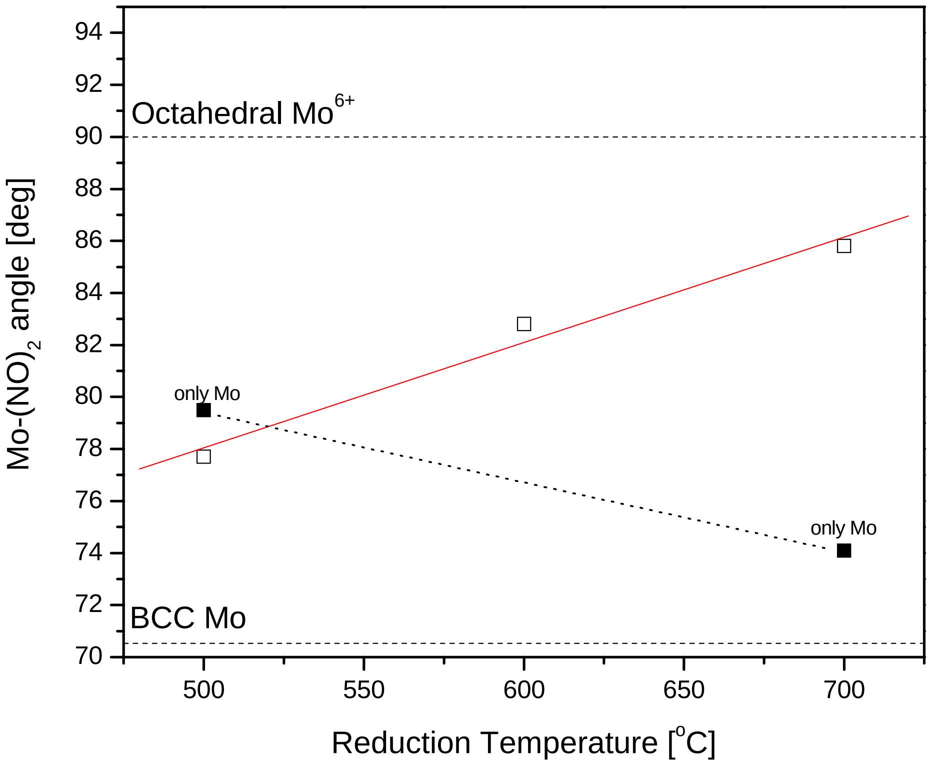

Figure 3.15 Calculated Mo-(NO)$_2$ angle in function of the reduction temperature for the HiSil supported catalyst. The Co angle was kept constant at 105°. For comparison, the monometallic Mo is also shown (full squares).

Even more important than the comparison with monometallic catalysts, it is the comparison with the angular data obtained on SiGel. As we can see from Figure 3.16, the assumption made before, fixing the Co angle to 105° (open squares), holds at low reduction temperatures, but predicts more than 130° after reduction at 700°C. Even the other possible, even if improbable, assumption of a Co angle equal 90° does not hold (full squares), having an initial angle too low (around 45°). However we can notice that the 500°C reduction and the 700°C reduction for the two assumptions will predict a Mo structure around 90° that is the expected. This suggests that there can be a transformation of the Co structure from tetrahedral to octahedral. This is shown in Figure 3.17 where the Mo angle was fixed to 90° and the Co was calculated. The initial point around 104° is in agreement with the $CoMoO_4$ structure. During the reduction, this angle seems to decrease to values close to 90°. This can be either attributed to CoO, that has a cubic structure, or to metallic Co, with its HCP structure. In this latter case, there are two equally possible configurations, 60° and 120°, which will average out resulting in an overall dipole moment corresponding to a 90° configuration.

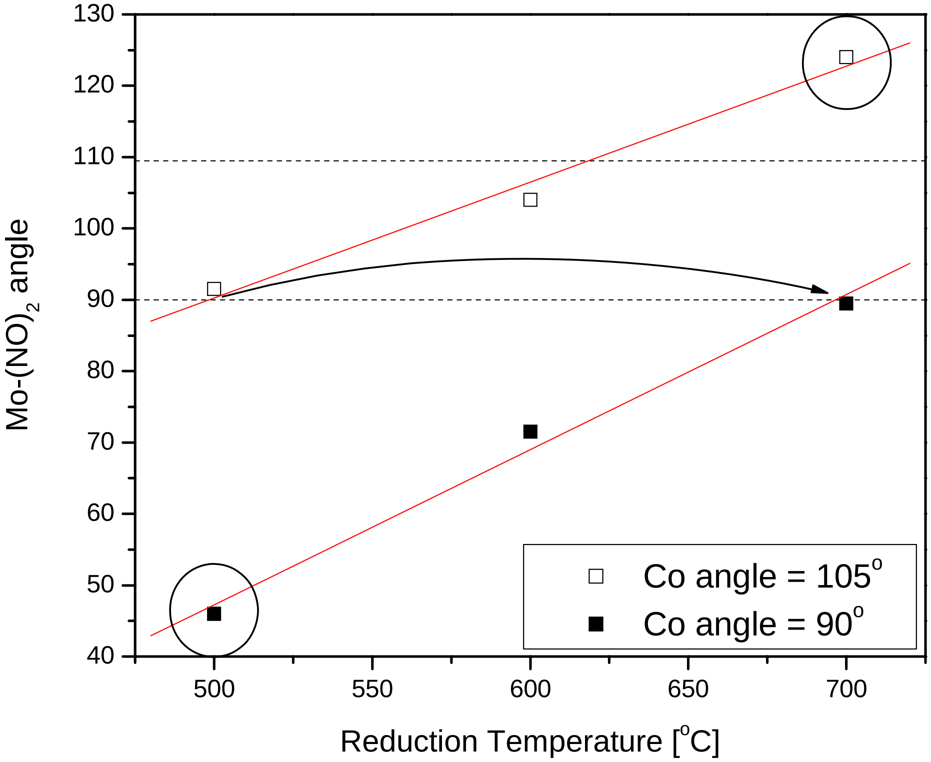

Figure 3.16 Calculated Mo-$(NO)_2$ angle in function of the reduction temperature for the SiGel supported catalyst. The Co angle was fixed at 105° (open squares) and 90° (full squares).

The formation we observed of segregated Co is in agreement with the TPR study presented previously and will probably result in an unselective (Type I) catalyst.

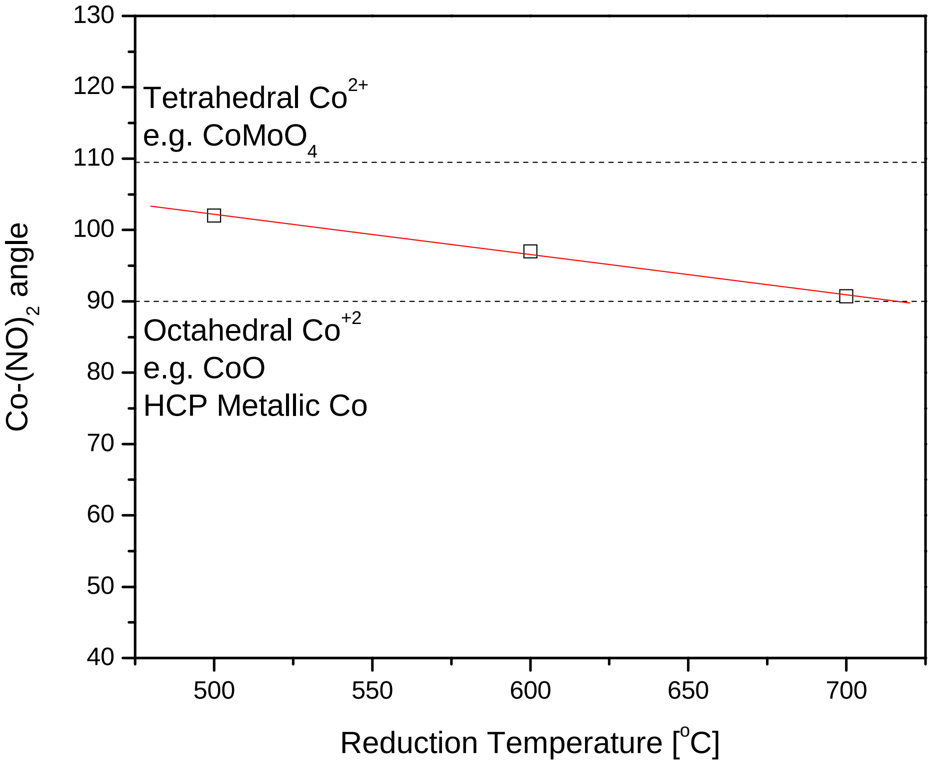

Figure 3.17 Calculated Co-(NO)$_2$ angle in function of the reduction temperature for the SiGel supported catalyst. The Mo angle was fixed at 90º.

3.4.4. Product Comparison

As we have seen, the two catalysts, even if extremely similar in composition and preparation, present completely different behavior during to the reduction process. If Type I and Type II selectivity, as described before, are functions of the microstructure of the catalyst, we will expect to see differences between these two systems.

Type I selectivity (selectivity of SWNT versus other forms of carbon), according to our catalyst model, is expected to be quite low in the case of the SiGel supported catalyst, due to the high amount of isolated Co present after reduction. Yet, the prediction of type II selectivity can be more complex. If, on one side, the large Co particles grow larger structures (probably only a few of them will be SWNT), on the other side, the remaining Co that is still interacting with the Mo will form very small islands of metallic Co that will have only a small chance of sintering (very slow kinetics) due to the lower effective availability of Co. These small clusters can eventually grow very thin nanotubes. On the other hand, the catalyst supported by precipitated silica, presents a good interaction with the support. It will be very selective for Type I, but probably not so much for Type II due to the broad distribution of sites and the higher chance to eventually sinter.

This difference is exactly what we have observed. If we compare the optical absorption of the SWNT produced on the two different catalysts (Figure 3.18), we can clearly see the narrower (n,m) distribution of the catalyst supported on SiGel. It presents only a pair of optical absorption peaks, corresponding to the dominating (6,5) SWNT [0.75 nm]. The other catalyst displays a large distribution of peaks centered around the (7,6) and (8,7) SWNT [0.88 and 1.02 nm, respectively]. However, as we can see, the intensity of the features, associated with the SiGel catalyst, is much weaker than the others. As explained in the next paragraphs, this is probably due to the presence of other forms of carbon (low Type I selectivity) that increase the background without participating in the optical transitions. This increase in background appears as a decrease of the spectral features if the signal is normalized to a specific wavelength value.

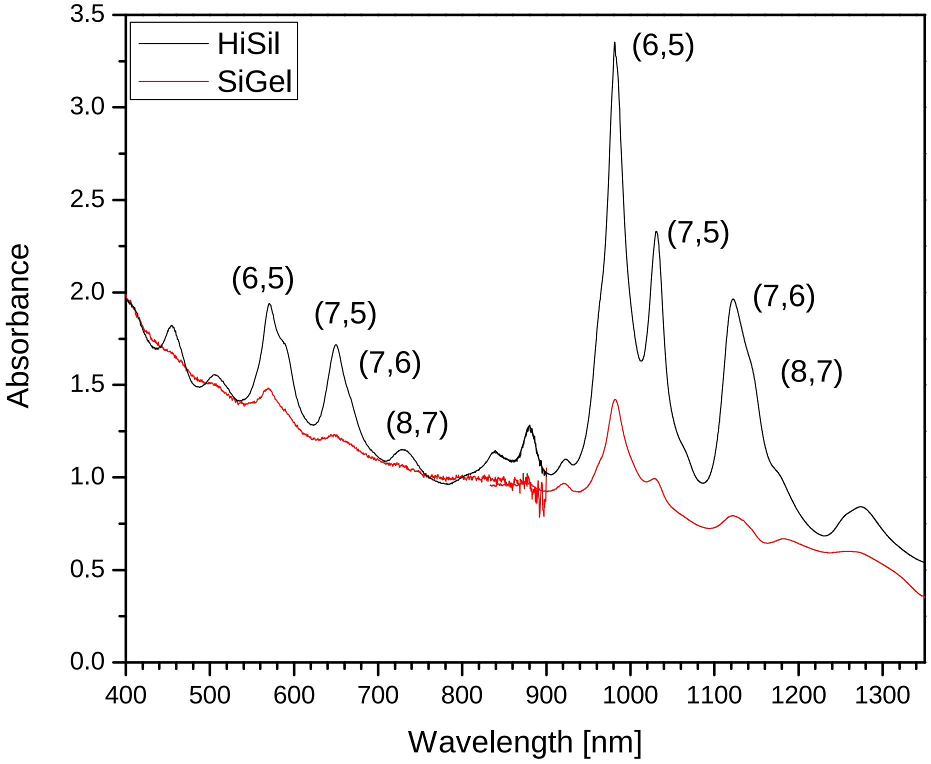

Figure 3.18 Optical absorption spectra of the sodium cholate suspension of SWNT produced on SiGel (red) and Hisil (black) supported catalyst.

3.5. Product Quality

Besides these clear differences in the reduction behavior of the catalysts, the final test, that we always have to refer to, is the growth of SWNT and their overall quality. There is not a single and clear characterization technique for the quantification of the quality of SWNT. The two most widely used and accepted techniques are Raman [5,20-24] and optical absorption spectra. [25-28]

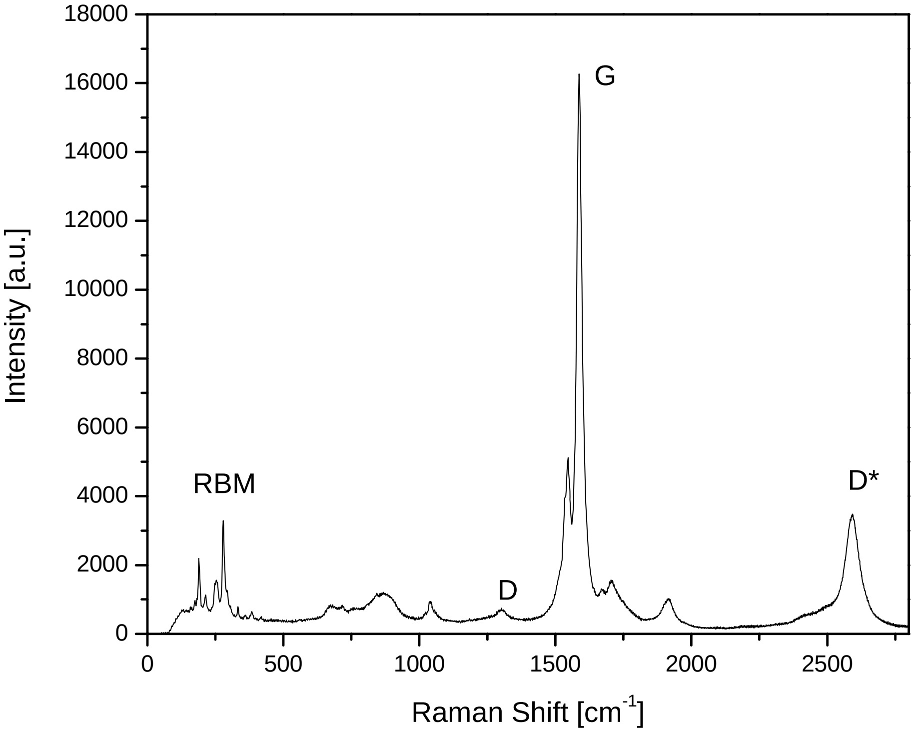

Figure 3.19 Raman spectrum of a SWNT sample. The SWNT's characteristic features are labeled.

In the Raman spectrum in particular (Figure 3.19), the features that are analyzed to infer the quality are the G band at 1,594 cm^{-1} and the D-D* bands, around 1,300 cm^{-1}-2,600 cm^{-1}. The origin of the D-D* bands is quite complex and it is discussed in more detail in Appendix A. Briefly, the D band is related to the presence of a defect (missing or extra atom and/or sp^3 carbon) in the crystalline sp^2 lattice of the graphitic wall of the SWNT. The G band is associated with the C=C vibration in sp^2 hybridized carbon. For this, the resulting ratio, D/G, is proportional to the ratio between defects and non-defects in a carbon nanotube, so it is desirable that it be as low as possible. Alternatively a so-called quality factor [5] defined as Q=(1-D/G) is also used and clearly equivalent.

Only recently, Thomsen [24] proposed to use the D/D* instead of the D/G ratio. The D* band is also associated with the lack of defects in the SWNT, like the G band, but is generated by a double resonance process, similar to D band. For this reason, it has been proposed as a better indication of the SWNT quality. We must say that both the D/G and D/D* follow the same trend, being an indication of the same phenomenon, but the D/D* is more sensitive, especially at low density of defects, than the D/G.

However, we have to remember that Raman of SWNT is highly resonant, meaning that only the SWNT excited by the specific laser wavelength are seen. This resonance results in a weak dependence of the features from the average of the sample. An example of that is given in Figure 3.20, where the quality factor (1-D/G) is apparently not affected by the differences in reduction temperature on HiSil.

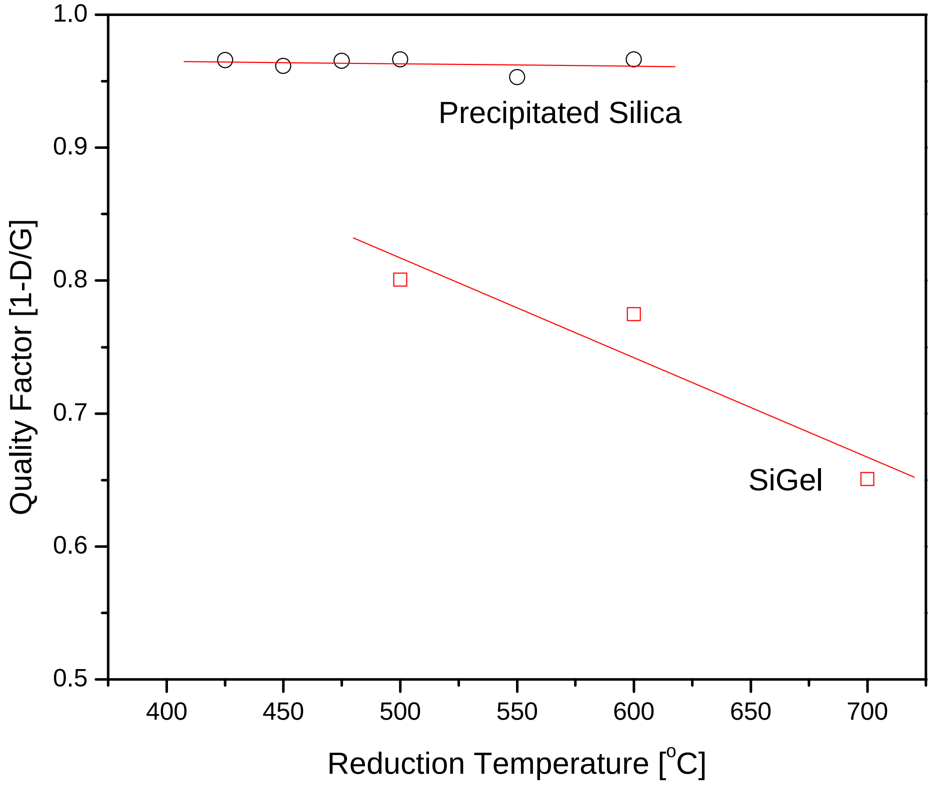

Figure 3.20 Quality factor in function of the reduction temperature for the differently supported catalysts.

The optical absorption features, as discussed in Chapter 1, are associated with the electronic transitions between the corresponding Van Hove singularities on the joined electronic density of states of SWNT. Because these transitions are generated by the superposition of quantized (and allowed) wavefunctions inside the SWNT lattice, a more crystalline and perfect SWNT will have sharper and higher Van Hoves singularities, resulting in stronger optical absorption features. Generally, the absorption spectra are normalized to the underlying background, which is caused by the carbon plasmon and the Reighley scattering of the photons against the suspended particles and, in principle, is proportional to the total amount of carbon present in the sample. The resulting ratio has been called "resonant ratio" and is described in Figure 3.20. [29] The ratio can be either calculated by selecting a specific SWNT band (as the example in Figure 3.21) or a range of bands. The important aspect of this method is the consistency of the measurement from sample to sample.

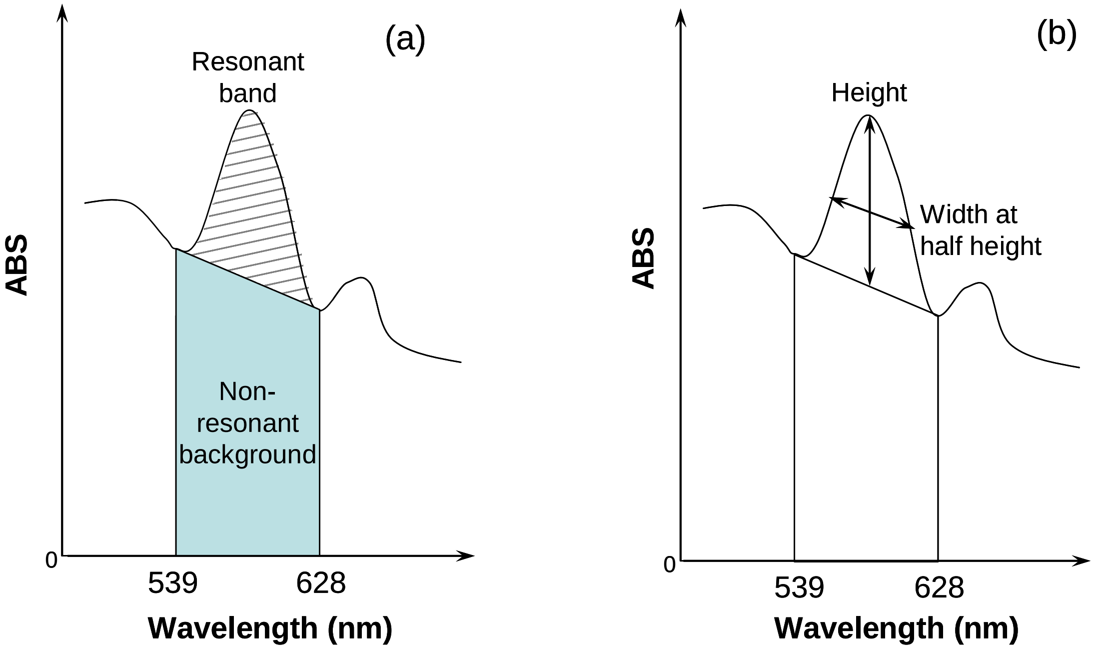

Figure 3.21 Estimation of (a) resonance ratio = (area of resonant band)/(area of nonresonant background); (b) normalized width = (width of resonant band)/(height of resonant band). [29]

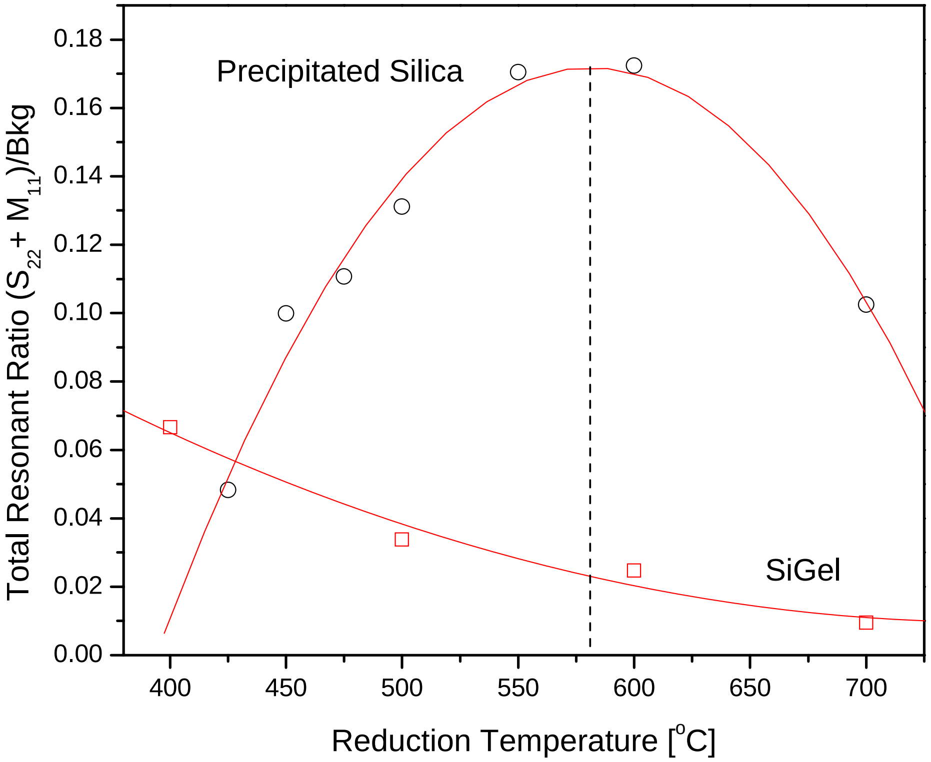

Figure 3.22 Resonant ratio in function of the reduction temperature for the differently supported catalysts.

As we can see, both the Raman quality factor (Figure 3.20) and the resonant ratio (Figure 3.22) are in agreement. For the SiGel supported catalyst, the overall quality is low and decreases at increasing reduction temperature. This can be explained by the high amount of Co bleached out of the $CoMoO_x$ that can sinter forming larger Co particles. In the case of the HiSil supported catalyst, the quality, from optical absorption, achieves a maximum point between 550°C and 600°C. Interestingly, this temperature corresponds to the maximum reduction rate in TPR (Figure 3.10). Until this temperature is reached, the catalyst still retains its oxidized structure and is only activated more and more, resulting in an easier reaction with CO, as well as a higher quality of the product. After that, the catalyst is over-reduced and the Co particles start sintering, resulting in the same problem of the SiGel catalyst: type I selectivity is reduced, resulting in a background increase and a lower resonant ratio.

3.6. Conclusions

The chemistry of the catalyst is extremely dependent upon the geometry and surface chemistry of the support used. This is due to the different interactions with the support and the resulting variations in behavior under pre-reduction.

Obtaining the right pre-reduction behavior is the key point for type I selectivity. A system that will not present the right interaction between the metal species and the support will not result in high selectivity.

Type II selectivity depends on the availability of Co and so on the nucleation kinetics. This will be discussed in more detail later. However, a catalyst that presents a very sharp reduction peak will result in a narrower distribution of sites generated during the decomposition, and therefore in a narrower distribution. Yet, in this case, the chances of getting over-reduced increase: the reduction window is narrower, as it happens for the first phase of the SiGel system.

Reference:

1 B. Kitiyanan, W.E. Alvarez, J.H. Harwell, D.E. Resasco *Chemical Physics Letters* **2000** 317, 497-503.

2 W.E. Alvarez, B. Kitiyanan, A. Borgna, D.E. Resasco *Carbon* **2001** 39, 547-558.

3 J.E. Herrera, L. Balzano, A. Borgna, W.E. Alvarez, D.E. Resasco *Journal of Catalysis* **2001** 204, 129-145.

4 D.E. Resasco, W.E. Alvarez, F. Pompeo, L. Balzano, J.E. Herrera, B. Kitiyanan, A. Borgna *Journal of Nanoparticle Research* **2002** 4, 131-136.

5 W.E. Alvarez, F. Pompeo, J.E. Herrera, L. Balzano, D.E. Resasco *Chemistry of Materials* **2002** 14, 1853-1858.

6 Z. Li, L. Gao, S. Zheng *Applied Catalysis A: General* **2002** 236, 163–171.

7 ICDD PDF-2 version 2004 with SLEEVE search engine.

8 A.L. Patterson *Phys. Rev.* **1939** 56, 978 – 982.

9 H. Topsøe, B.S. Clausen, F.E. Massoth *Hydrotreating Catalysis, Science and Technology*, **1996** Springer-Verlag.

10 M. Daage, R.R. Chianelli *J. of Catalysis* **1994** 149, 414-427.

11 R.T.K. Baker, J.J. Chuldzinsky *J. Catal.* **1980** 64, 464

12 G.L. Haller, D.E. Resasco *Adv. Catal.* **1989** 36, 173.

13 S.A. Stevenson, J.A. Dumesic, R.T.K. Baker, E. Ruckensein *Metal Support Interactions in Catalysis, Sintering and redispersion* **1987** Van Nostrand Reinhold.

14 N.Y. Topsoe, H. Topsoe *J. Catal.* **1982** 75,354.

15 P. Ratnasamy, H. Knozinger *J. Catal.* **1978** 54, 155.

16 S.K. Bhargava, D.B. Akolekar *Journal of Colloid and Interface Science* **2005** 281, 171–178.

17 S.F. Parker, A. Amorelli, Y.D. Amos, C. Hughes, N. Porter, J.R. Walton *J. Chem. Soc. Faraday Trans.* **1995** 91(3), 517-524.

18 W.H. Heston, R.K. Iler Jr., G.W. Sears Jr. *J. Phys. Chem.* **1960** 64, 147.

19 F. Prinetto, G. Ghiotti *Spectrochimica Acta Part A* **1999** 55, 2495–2511.

20 Y.A. Kim, H. Muramatsu, M. Kojima, T. Hayashi, M. Endo, M. Terrones, M.S. Dresselhaus *Chemical Physics Letters* **2006** 420(4-6), 377-381.

21 S. Maruyama, Y. Miyauchi, Y. Murakami, S. Chiashi *New Journal of Physics* **2003** 5, 1-12, Paper No. 149.

22 J.E. Herrera, D.E. Resasco *Chemical Physics Letters* **2003** 376(3,4) 302-309.

23 J.F. Colomer, C. Stephan, S. Lefrant, G. Van Tendeloo, I. Willems, Z. Konya, A. Fonseca, C. Laurent, J.B. Nagy *Chemical Physics Letters* **2000** 317(1,2), 83-89.

24 S. Reich, C. Thomsen, *Phys. Rev. B* **(2000)** 62, 4273.

25 M.E. Itkis, D.E. Perea, R. Jung, S. Niyogi, R.C. Haddon *Journal of the American Chemical Society* **2005**, 127(10), 3439-3448.

26 A.G. Ryabenko, T.V. Dorofeeva, G.I. Zvereva *Carbon* **2004** 42(8-9), 1523-1535.

27 B. Zhao, M.E. Itkis, H. Hu S. Niyogi, R.C. Haddon *Abstracts of Papers, 227th ACS National Meeting, Anaheim, CA, United States, March 28-April 1, 2004* **2004** IEC-215.

28 O. Matarredona, H. Rhoads, Z. Li, J.H. Harwell, L. Balzano, D.E. Resasco *Journal of Physical Chemistry B* **2003** 107(48), 13357-13367.

29 Y. Tan, D.E. Resasco *Journal of Physical Chemistry B* **2005** 109(30), 14454-14460.

CHAPTER 4

4. Tailoring the catalyst to optimize selectivity Type I and II

In the first two chapters we have discussed the importance of having high Type I and Type II selectivity to meet the applications' demands for SWNT. Later in Chapter 3 we have seen how the microstructure of the catalyst is responsible for Type I selectivity, and how the catalyst phases evolve during the steps of the production. We have also described how the selectivity towards a specific (n,m) type (Type II selectivity) is affected by the nucleation step of the growing SWNT. Now, keeping in mind the growth mechanism of SWNT, it is possible to tune some process variables to improve Type I selectivity and control type II selectivity.

4.1. Effect of the support

As we have seen in Figure 3.18 the same catalyst formulation (Co:Mo 1:3 molar ratio 2 wt%) supported on different silica can produce a different SWNT distribution when the type of silica changes. We have explained this difference in terms of a different nucleation behavior: the catalyst supported on SiGel presents a low temperature reduction peak associated with a Co-rich phase. This phase reduces easily and releases Co that can further aggregate and produce larger carbon structures, resulting in a low Type I selectivity. During this step, Co is depleted from the Mo-rich phase; when this phase is attacked by CO, Co ions are released and can nucleate very small clusters onto the surface resulting in small diameter SWNT. This catalyst seams to have a high selectivity towards the (6,5) SWNT. A possible explanation for this specificity can be found in the general mechanism of SWNT growth. As we have said in Chapter 2, one of the requirements for producing a carbon structure is using as a catalyst a metal like Fe, Ni or Co that can dissolve C inside its lattice. Isolated atoms can eventually dissociate the carbon containing gas, but cannot dissolve the released carbon. Therefore there is a critical size above which the number of atoms present in a cluster is enough to produce a coherent lattice structure and dissolve an appreciable amount of carbon. For example a spherical Co cluster of 0.8 nm contains only 24 atoms, while a 1 nm cluster has 48 atoms.

When the cluster is too small, the solubility of C is limited. When it reaches the critical size, probably around 0.8 nm, it can start the growth of SWNT. For a metal cluster of this size the expected SWNT diameter is around 0.75 nm, which corresponds exactly to the (6,5) nanotube. Thus, the reason for the high selectivity towards (6,5) is that it is one of the first SWNT corresponding to the critical size above which the Co clusters start dissolving carbon inside their lattice.

To understand this better, we also have to consider that once the SWNT cap (Figure 2.2) has been formed, the chirality of the SWNT has been determined and the growth of the Co particle is locked by the layer of carbon on the surface. The nucleation step is what determines the (n,m) type.

We can say that the Type II selectivity is determined by the ratio between the kinetics of growth of the Co cluster and the kinetic of nucleation of the SWNT. If the Co cluster has a growth rate much slower than the cap nucleation rate, as soon as it reaches the critical size, the SWNT starts growing and freezes future growth of the metal particle. The resulting distribution will be very narrow around the critical size. On the opposite, if the rate of Co growth is faster than the rate of nucleation of the SWNT, the metal particles will keep growing resulting in a distribution of diameters larger than the critical.

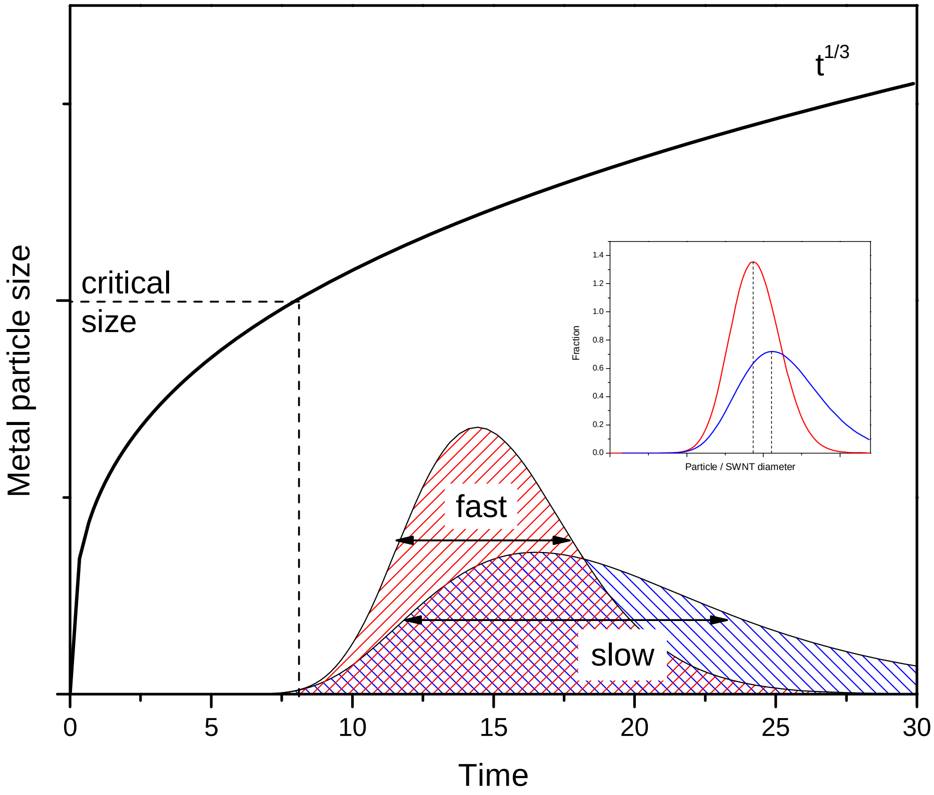

Figure 4.1 Nucleation rate and corresponding diameter distribution (inset) for a given metal growth kinetic.

That competition is illustrated in Figure 4.1. If we consider a constant rate of addition of Co atoms to the cluster, the diameter will increase as $t^{1/3}$. We can model the nucleation probability distribution above the critical particle size with a lognormal distribution. In the lognormal distribution the probability of nucleation is reduced by the presence of already nucleated particles, this is the case of SWNT. The red and blue regions in Figure 4.1 represent distributions with a fast or slow kinetic parameter; we can now plot this probability as a function of the instantaneous size of the metal particle at that time. This gives a diameter distribution of the metal particles at the time of nucleation (inset in Figure 4.1). As we can see, the distribution is shifted towards larger particles and becomes broader for slower kinetics.

This behavior is what we observed comparing the product distribution of the two differently supported catalysts, keeping the catalyst composition and reaction conditions constant (Figure 3.18). On the SiGel supported catalyst, the amount of Co effectively interacting with Mo is less due to the bleaching during the reduction in H_2. Moreover, the Mo framework is just partially reduced, resulting in a slow carburization by CO. If the decomposition of the MoO_x framework is slow, the nucleation of the Co particles is limited by the release rate of these ions from the Mo-rich phase. This results in high selectivity towards the (6,5) SWNT. Contrarily, on the HiSil supported catalyst, the $CoMoO_x$ phase before contact with CO has a high amount of Co at the surface and the MoO_x is heterogeneously reduced, being the TPR peak (Figure 3.11) very broad. This results in a fast nucleation of the Co atoms and a broader distribution of diameters, centered on larger particles size (around 1 nm that has twice the Co atoms than a 0.8 nm cluster).

However, even if the material produced on SiGel supported catalyst has very high Type II selectivity, the Co released at low reduction temperatures results in a poor Type I selectivity. A very good catalyst candidate for high Type I and Type II selectivity should be characterized by a strong metal support interaction (as the HiSil supported catalyst) and by a better balanced ratio between the Co growth and the nucleation kinetics.

If the Co particle growth rate is controlled mainly by the catalyst microstructure, and this one is limited by the requirements of Type I selectivity, the cap nucleation kinetics is affected also by the gas side: the Boudouard reaction provides the C for the SWNT growth. Its rate is affected by the pressure of the system, the temperature and the composition of the feed gas. Accordingly we can now change these variables to alter the nucleation kinetics and try to obtain higher (n,m) selectivity on the HiSil supported catalyst that already presents high Type I selectivity.

4.2 Effect of the pressure

The Boudouard reaction $2CO \longleftrightarrow CO_2 + C_s$ is a non-equalmolar exothermic reaction characterized by reversibility and equilibrium. In the simplest reversible kinetic model we can assume:

$$r = kp_{CO}\left(1-\frac{{p_{CO_2}}/{p^2{}_{CO}}}{K_{eq}}\right)$$ **Equation 4.1**

This is characterized by a kinetic term (outside the parenthesis) and an equilibrium term (inside the parenthesis). When the system approaches the equilibrium, that is when the forward reaction has the same speed as the reverse reaction, the equilibrium term approaches zero, resulting in a null net rate. An increase in the temperature of the reaction will increase the kinetic term according to the Arrhenius expression:

$$k = k_0 \exp\left(-{E_{att}}/{RT}\right)$$ **Equation 4.2**

but it will decrease the equilibrium term, since the reaction is highly exothermic:

$$\begin{aligned} K_{eq} &= \exp\left(-{\Delta G}/{RT}\right) \\ \Delta G &= \Delta H - T\Delta S \\ \Delta H^0 &= -41.22\,{kCal}/{mol} = -172.3\,{kJ}/{mol} \end{aligned}$$ **Equation 4.3**

This results in a net functionality, which can be positive, negative or null, depending on pressure and gas composition.

On the other side, the increase in partial pressure of the system, has a double effect: it increases the kinetic term, by a greater number of collisions between CO molecules and the surface, and it also increases the equilibrium term, being the reaction characterized by a reduction of the number of moles, so moving the system away from equilibrium. This should result in a large increase in the rate of carbon deposition and eventually increasing the SWNT nucleation step.

The effect of the pressure on the total amount of carbon produced is clear from Figure 4.2. The carbon deposited after 30 min. reaction increases almost linearly with the pressure of CO.

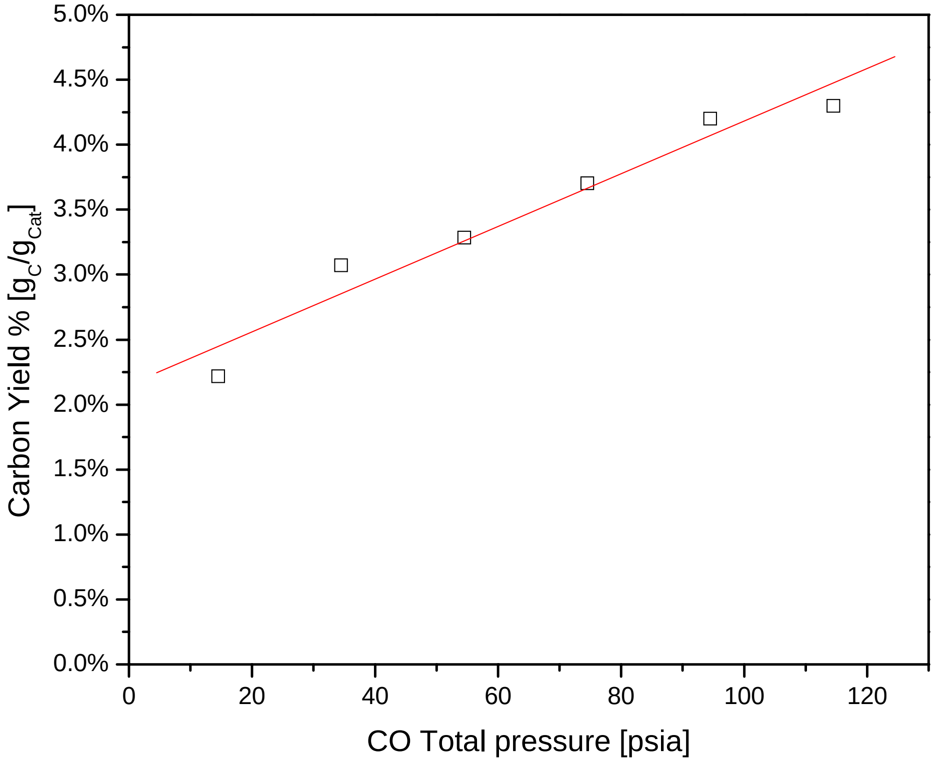

Figure 4.2 Effect of total pressure of CO on the carbon yield obtained. The other process variables were kept constant: reduction T 550°C 30 min.; reaction T 750°C 30 min. pure CO; He as inert gas; Catalyst 1:3 Co:Mo 2wt%.

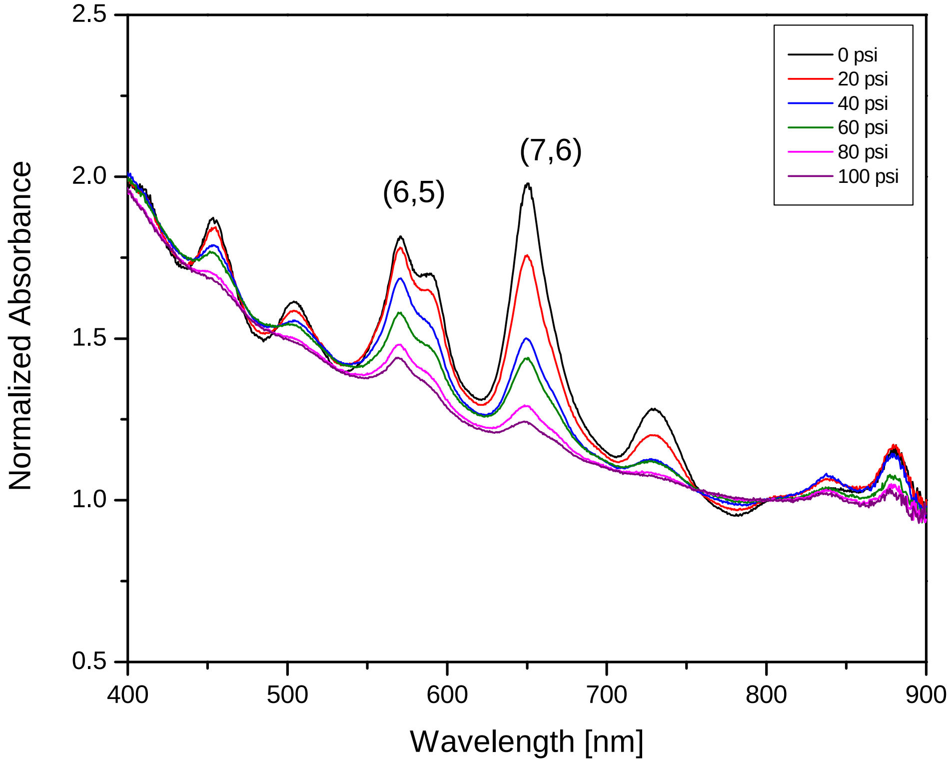

Figure 4.3 Effect of pressure on the SWNT (n,m) distribution measured by optical absorption.

To understand the effect of pressure on the cap nucleation kinetic we have to analyze the (n,m) distribution of the SWNT produced (Figure 4.3). As we can see, there is an overall reduction of the resonant ratio (i.e. quality of the SWNT) at increasing pressures, especially above 60 psig. However, there is also a shift of the mean diameter towards smaller SWNT and especially the (6,5) SWNT. For example at a pressure equal to 0 psig, the dominant SWNT is the (7,6) with a sharp transition around 650 nm. At just 20 psig, the intensity of the (7,6) drops and equal that of (6,5) that corresponds to the transition at 570 nm. At 40 psig, the (6,5) SWNT becomes dominant. Above that pressure the overall distribution does not change much, but the overall quality keeps dropping. We can see this trend better if we focus only on the pressure range 0-40 psi, as shown in Figure 4.4: there is a reduction in nanotube diameter that asymptotically reaches the value of the (6,5) nanotube.

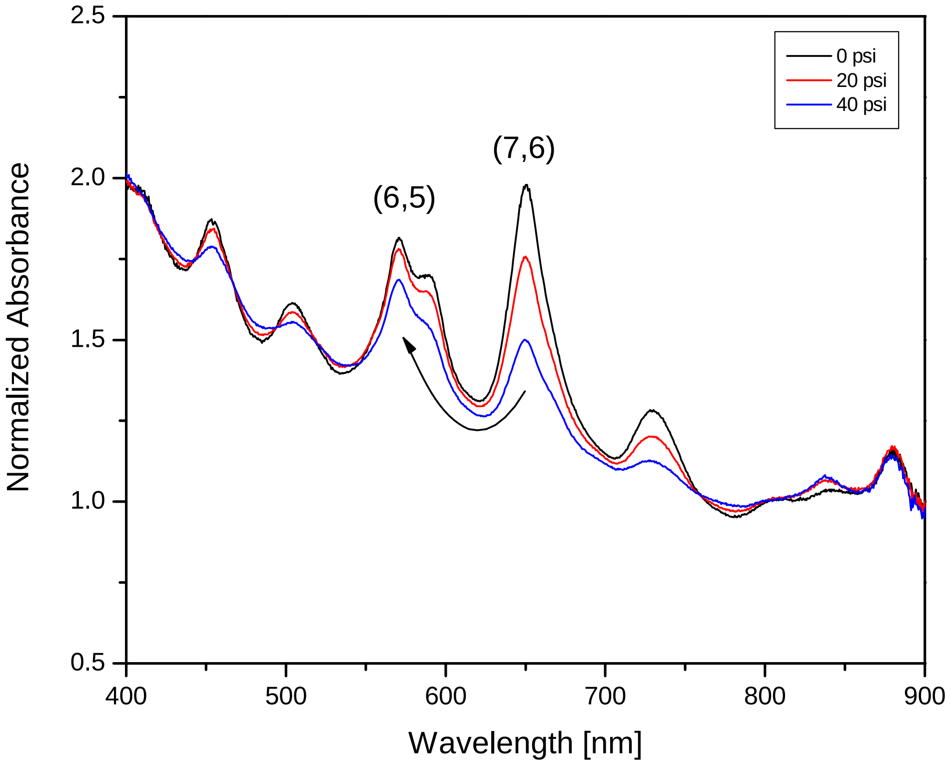

Figure 4.4 Extract from Figure 4.3 for the pressure range 0-40 psi.

This is in perfect agreement with our kinetic growth model. The only thing that is not entirely clear is the effect of pressure onto the quality of SWNT. We offer two possible explanations:

a) The higher pressure and higher growth rate can affect the quality of the SWNT not allowing the carbon atoms to find the best configuration before leaving the surface of the metal, thus creating 5- and 7-member rings on the sidewall of the SWNT. However, in the case of the vertically aligned SWNT produced by the same method, as shown in Figure 2.6, the rate of growth is much higher than the rate in the high surface area catalyst and the product has high quality, even if the diameter distribution is much larger.

b) The other possible explanation is the accumulation of CO_2 inside the pores, where it is produced. There, the reverse Boudouard reaction can be important. Gasification of C atoms inside the structure of the SWNT, leaving a vacancy in the lattice, or even oxidation of SWNT by CO_2 can happen. Moreover this accumulation of CO_2 inside the pores, where the catalyst is present and active, can affect the rate of reaction.

4.3 Effect of gas composition

4.3.1 Inert diluting gasses

To further investigate the effect of possible CO_2 accumulation inside the pores and the internal diffusion limitations associated with the system, a series of experiments with different gas compositions has been performed. Considering that the diffusivity of CO_2 changes depending on the gas composition. The addition of an inert gas allows changing slightly the diffusion coefficient of the mixture, thus revealing possible internal diffusion limitations for the CO_2 generated. A series of experiment using mixtures of 25% inert gas / 75% CO has been performed using, as inert gases, He, Ar and N_2.

To keep the intrinsic kinetic constant, the partial pressure of CO was maintained constant in all the experiments. Specifically, the total pressure was fixed at 34.5 psia (20psig) for the pure CO experiment and was increased to 46 psia (31.5 psig) for the 75% CO in inert gas. The diffusivity of CO_2 in the different gases: He, Ar, N_2 and CO is shown in table 4.1.

	He	Ar	CO	N_2
$\mathcal{D}$ (m^2/s)	$2.05 \cdot 10^{-5}$	$5.50 \cdot 10^{-6}$	$5.79 \cdot 10^{-6}$	$5.89 \cdot 10^{-6}$

Table 4.1 Estimation of the diffusion coefficients of CO_2 in different gases. [1,2]

If we compare the SWNT chirality (Figure 4.5) for the three samples (pure CO, 75% CO in He and 75% CO in Ar), we can see that there is no appreciable difference in the SWNT chiral distribution and total carbon yield, even if the diffusivity of the gas mixture to CO_2 increases in the sequence He>>CO>Ar. This suggests that there are no internal diffusion limitations to the reaction or the accumulation of CO_2 does not affect the nucleation rate.

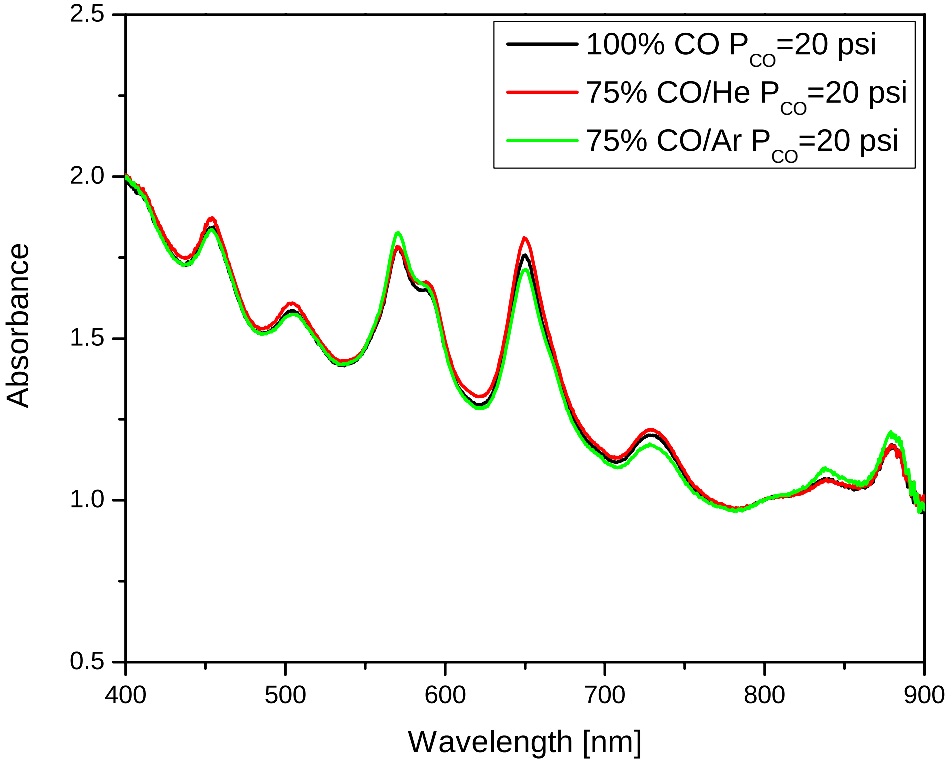

Figure 4.5 Effect of inert gas dilution on the chirality of SWNT at constant partial pressure of CO.

4.3.2. Dilution with Nitrogen

If we now compare the product obtained using 75% CO in N_2 with the SWNT produced on pure CO, shown in Figure 4.6, we can see that there is a drastic decrease in the concentration of larger diameter SWNT in the case of N_2 dilution and an increase in the concentration of (6,5) species. This cannot be explained by differences in the physical behavior of the system: the mass diffusion is very similar for pure CO as for the CO/N_2 mixture and, as we have seen before, the system seems not to be affected by internal diffusion limitations. The difference should be ascribed to in the chemical nature of N_2 compared to noble gasses like He or Ar. In the case of N_2, it is known that it tends to dissociate on metals, especially at high temperatures. [3,4] A typical example is the ammonia synthesis process, that is generally performed at temperatures around 600 °C over Fe(111). Atomic N is produced on the surface of the metal. Balbuena et al., in a DFT simulation of the dissociation of CO over Ni at 750 °C, observed that, in presence of N_2, some atomic N is present on the surface of the metal. [5] Compared to C, N has an extra electron, thus it can still form 3-directional bonds, like sp^2 carbon, but the angle between them is 109.5° (sp^3 hybridization) instead 120°. The introduction of a possible N atom in the structure of SWNT would reduce the stress due to the curvature compared to planar graphite. This modification can be especially important during the formation of the cap, where the curvature is higher and the presence of highly distorted pentagons is necessary to close the structure. A reduction in the stress between the bonds might result in a reduction in the activation energy (E_{att}) of the process for SWNT nucleation, resulting in an increase in the kinetic rate according to an Arrhenius behavior as shown in equation 4.2. Like pressure, this increase in the kinetic constant would have a similar, if not higher, effect on the reduction of the diameter distribution around the critical size.

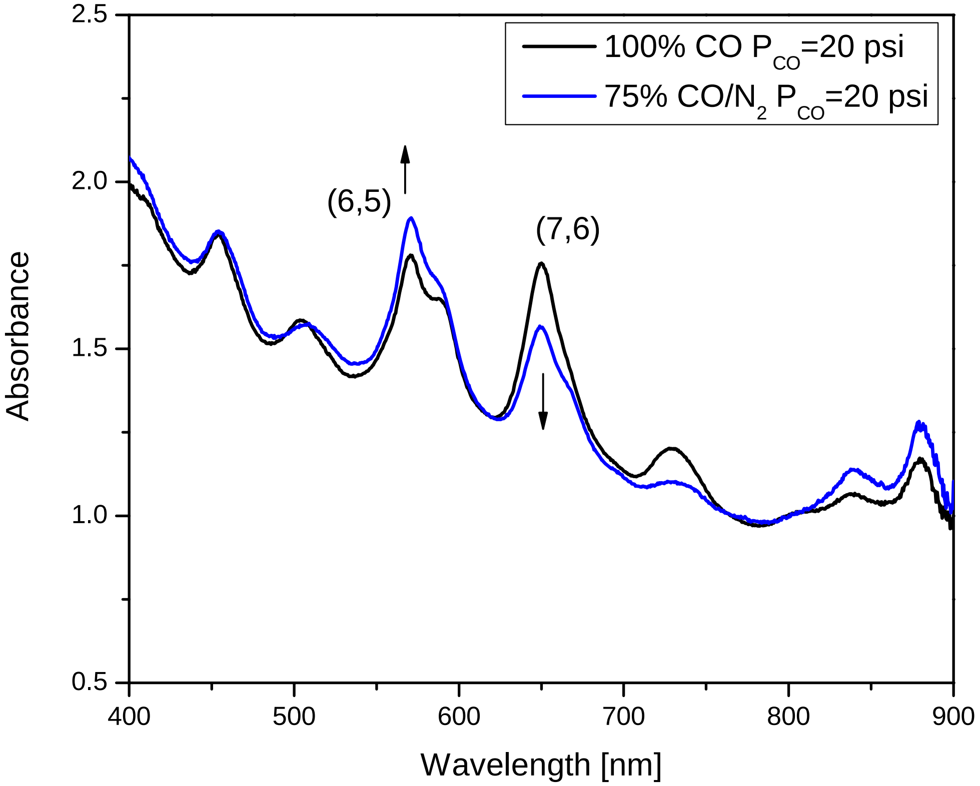

Figure 4.6 Effect of N_2 dilution on the chirality of SWNT at constant partial pressure of CO.

The direct measurement of N inside the crystalline lattice of a SWNT is a hard task, but we can have an indirect measurement using Raman scattering. In the spectrum of a SWNT 4 characteristic regions can be identified: the radial breathing mode (RBM) at low wavenumbers, the disordered-carbon band (D) around 1,300 cm^{-1}, the graphite band (G) at 1,592 cm^{-1} and the first harmonic of the D band (D*) around 2600 cm^{-1}. The physical phenomena that generate these bands are described in more detail in the appendix. When N is present in the atomic structure of a SWNT, the whole electronic structure will be affected and it will appear as a defect in the crystalline lattice. The most widely used indication of defects in SWNT is the ratio between the D band, that is generally and erroneously attributed to the vibration of a sp^3 carbon, while instead is related to the presence of a defect in the structure, and the G band that is associated with the vibration of a sp^2 carbon, so it represents the crystalline perfection of the system. Recently, Thomsen et al. [6,7] proposed to use the ratio between D and D* bands instead of D and G. The D and D* bands are generated by the interaction of the excited electron with a defect (D) or a phonon (D*). Thus, since both D and D* capture the same physical phenomena, in presence (D) or not (D*) of a defect, the ratio D/D* is a more reliable indication than the widely used D/G ratio. An increased number of defects inside the structure will increase the D band and decrease, at the same time, the D*, resulting in a more precise detection of defects, especially at low density.

The Raman spectra of the SWNT produced in pure CO and the mixed 75% CO in N_2 are shown in Figure 4.7. There is a small but significant increase in the D band, associated with a decrease of the D*, in presence of N_2. This, even if is not a direct measurement of the presence of N inside the SWNT lattice, support our findings.

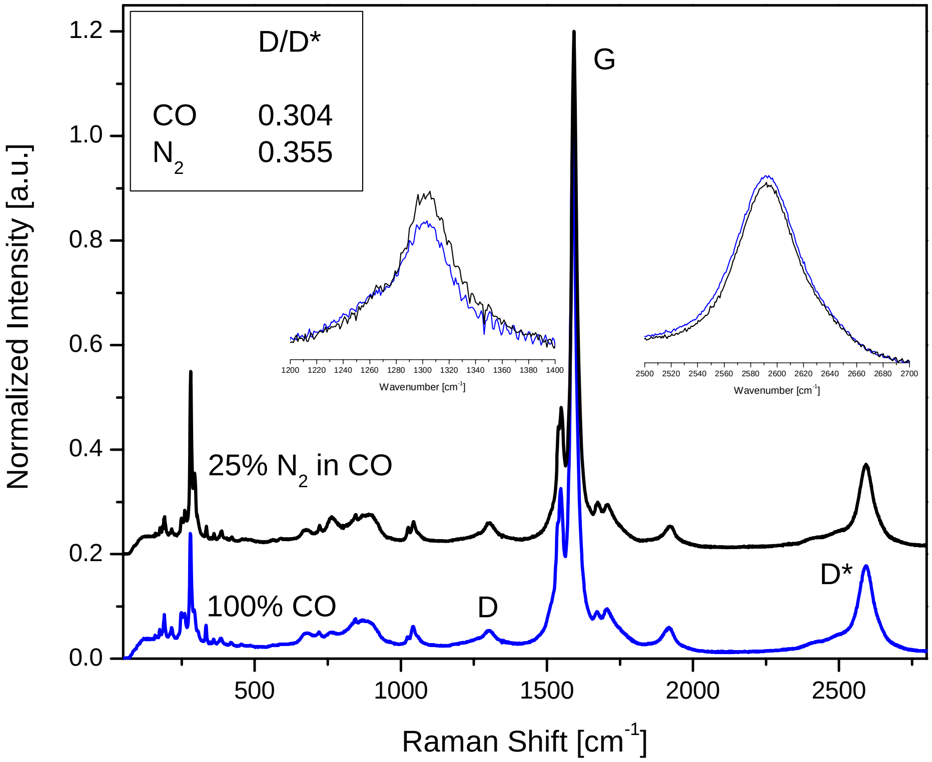

Figure 4.7 Raman spectra of the SWNT produced using pure CO and 25% N_2 in CO. The D and D* bands are respectively enlarged on each side of the G band.

4.3.3. Chemically active gasses

If the addition of an almost inert gas like N_2 has a large effect on the SWNT (n,m) distribution, the addition of small amount of gasses that can actively participate in the reaction process can have even a larger impact. The most obvious is the addition of CO_2, which is the byproduct of the reaction: it can gasify carbon and reduce the rate, since the reaction is characterized by reversibility.

4.3.3.1 CO_2 Addition

The addition of 0.3% CO_2 in CO at 20 psi during the reaction, produces no differences in the (n,m) distribution as shown in Figure 4.8 but produces a large increase in the resonant ratio (the ratio between the SWNT bands and the non resonant background). This is associated with an increase in the quality of the product.

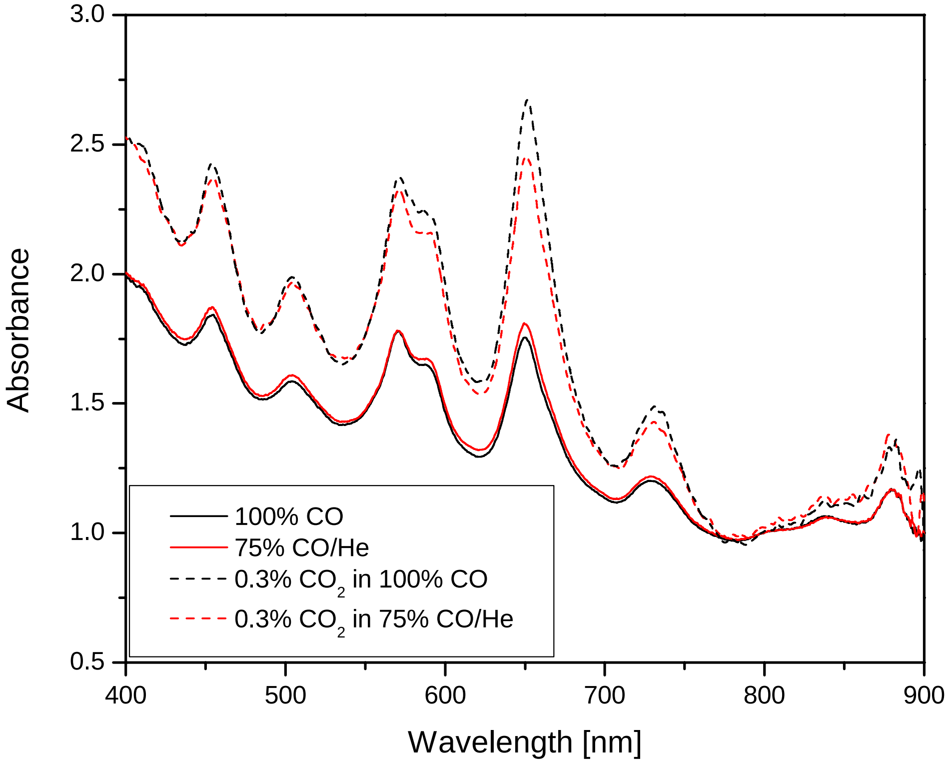

Figure 4.8 Optical absorption spectra of the SWNT obtained in pure CO (black) and 75% CO/He (red) with (dashed) and without (continuous) addition of 0.3% CO_2

A possible explanation for the observed phenomenon is the cleaning of the SWNT surface by CO_2 from possible amorphous carbon generated during the growth process. Amorphous carbon is thermodynamically and kinetically less stable than SWNT, so a selective removal is possible, and consequently an increase in the quality of the product.

4.3.3.2 Water addition

The use of oxidizing gasses to reduce the amount of carbon deposited is widely known in the chemical industry, especially in the reforming process. The typical gas used is steam. It can react with solid C forming CO and H_2. However, water is a much stronger oxidizing agent than CO_2 so it could also affect the catalyst by reducing its activity, or even attacking the SWNT.

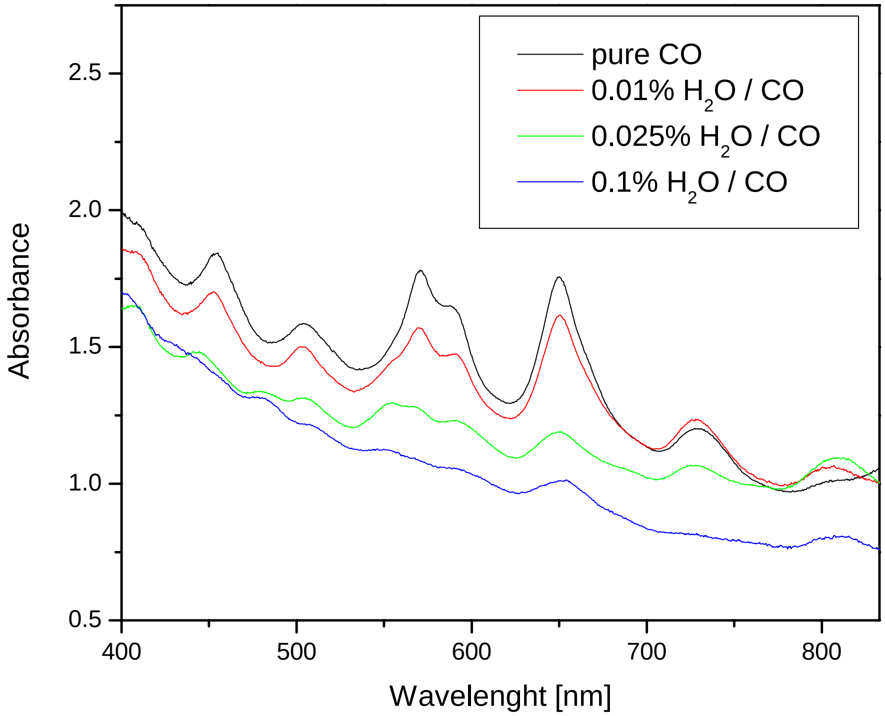

Figure 4.9 Optical absorption spectra of SWNT, showing the effect of addition of increasing amount of water into the CO gas stream.

The harsher effect of water is shown if Figure 4.9, where, it is seen that the quality of the material follows a downward trend with the addition of water. Even very small amounts of H_2O can compromise the product and the cleaning effect, which is clear for CO_2 is not observed here. Above 250 ppm H_2O, the material is severely attacked.

4.4 Effect of temperature

The temperature has a double effect on equation 4.1: on one side it increases the kinetic constant k that follows an Arrhenius-type law (equation 4.2) and, at the same time, it reduces the equilibrium term being the reaction exothermic, so unfavored at high temperatures (equation 4.3).

Moreover, the diffusion and mobility of the metals on the surface are greatly affected by a temperature increase. This can over-compensate the increase in nucleation kinetics resulting in much larger diameter SWNT.

The net effect can be very limited and not as clear as the pressure effect. This is exactly what we observed. In a wide range of temperatures from 725 to 800 ºC, the (n,m) distribution and quality of the product were unchanged. [8] Apparently, it even seams that the distribution moves to smaller diameters, in line with a faster nucleation kinetics (see Figure 4.10). Above 800 ºC, there is a huge shift towards larger diameter tubes: the (6,5) SWNT almost disappear and larger SWNT, like the (8,7), become predominant. This goes is parallel with a significant reduction in the quality of the product.

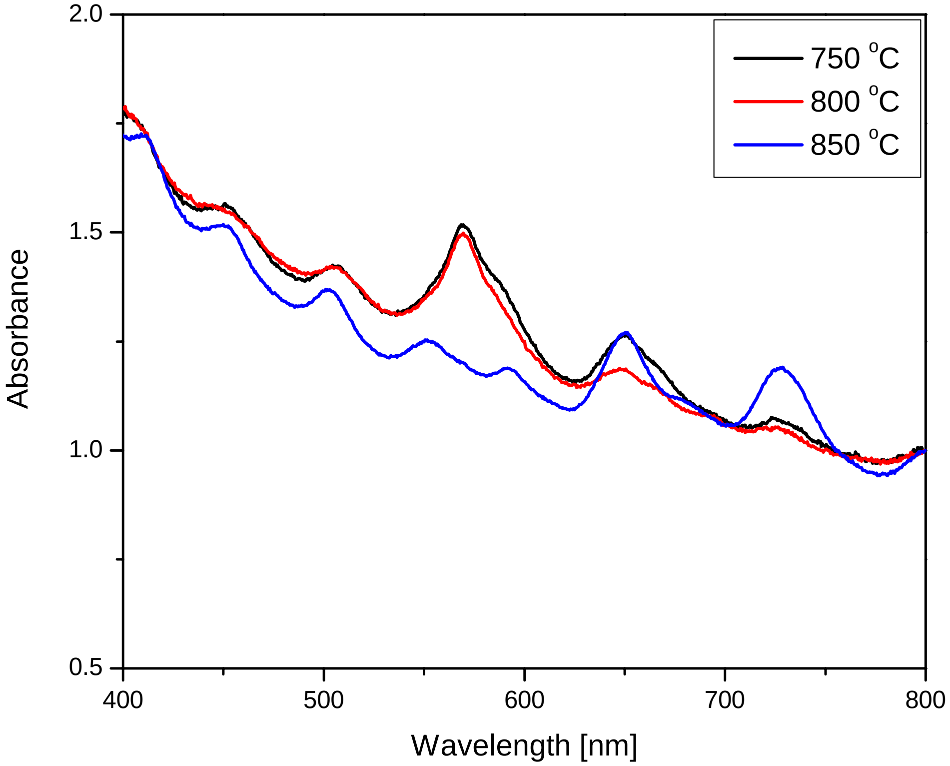

Figure 4.10 Effect of reaction temperature on the SWNT product distribution (conditions 60 psi pure CO).

The behavior at high temperatures is explained by the increased rate of sintering of the metal particles. Moreover, it can be also affected by the silica substrate that, at temperatures above 800-850 °C, starts sintering, reducing the available surface area and reducing its interaction with the supported metal oxides. This collapse of the support magnifies the direct effect of temperature on particle mobility. This phenomenon is associated with reduction of the surface area and a real collapse of the catalyst bed, which visibly reduces in volume. This modification of the surface morphology creates larger particles that grow larger diameter SWNT and also other forms of carbon and does not allow the catalyst to work properly.

4.5 Conclusions

Type I selectivity is associated with the microstructure of the catalyst and its interaction with the support. It can also be affected by the byproducts of the reaction (in this case CO_2) that can alter the quality of the produced SWNT.

Type II selectivity is associated with the rate between the Co cluster growth (on the surface of the catalyst) and the rate of nucleation of SWNT (onto these particles). If the rate of Co sintering is greater than the rate of nucleation, the material produced will have a broader distribution of SWNT species, centered around larger tubes; if the rate of nucleation is fast enough, the nanotube distribution will be very narrow and centered close to the critical particle size. From our observations, this correspond to the (6,5) SWNT that has a diameter of only 0.75 nm. The embryonic particle will be around 0.8-0.85 nm and will contain only 20-30 Co atoms, probably the minimum required to form a structure that can dissolve effectively C inside its lattice.

The most effective way of changing the ratio between the rate of SWNT nucleation and the rate of Co particles growth is altering the pressure of the system.

Dilution with a noble inert gas does not affect the (n,m) distribution, while the addition of a more reactive diluting gas, like N_2, can modify the chemistry of the system, affecting the activation energy of the process. The addition of a small amount of CO_2 can help in cleaning the surface of the SWNT from amorphous carbon, increasing the quality of the product.

Reference:

1 R.H. Perry, D.W. Green, *Perry's Chemical Engineers' Handbook* 7th Ed. **1998** McGraw Hill.

2 Fuller, Shettler, Giddings *Ind. Eng. Chem.* **1966** 58, 18.

3 M. Bowker, *Topics in Catalysis* **1994** 1(3-4), 265.

4 G. Strasser, M. Grunze, M. Golze Journal of Vacuum Science & Technology A: Vacuum, Surfaces and Films **1985** 3(3), 1562-1564.

5 Dr. Balbuena's private communication.

6 S. Reich and C. Thomsen, *Phys. Rev. B* **(2000)** 62, 4273.

7 J. Maultzsch, S. Reich, C. Thomsen, S. Webster, R. Czerw, D. L. Carroll, S. M. C. Vieira, P. R. Birkett, and C. A. Rego *App. Phys. Lett.* **2002** 81, 2647.

8 G. Lolli, L. Zhang, L. Balzano, N. Sakulchaicharoen, Y. Tan, D.E. Resasco *Journal of Physical Chemistry B* **2006** 110(5), 2108-2115.

CHAPTER 5

5. Chemical potential model

As we have seen in the previous chapters, Type I selectivity is controlled by the catalyst microstructure and phase composition, while Type II selectivity is determined by the balance between the SWNT nucleation rate and the metal-particle growth rate. To better understand these phenomena, we have developed a kinetic model that attempts to capture mathematically the behavior of the different stages. Also, a realistic kinetic model may be useful in the optimization of reactor design and operation. At the same time, it may serve as the basis for further understanding the growth mechanism. Therefore, we have attempted to minimize the number of empirical equations using parameters with physical significance.

5.1. Steps considered in the model

Specifically, the different stages considered in this model are the following:

5.1.1. Carburization of the oxidic phase:

This step, described from a physical-chemical point of view in Chapter 3, is fundamental to complete the phase transformation in the active catalyst, but does not generate directly the active sites, which, for our purpose, are defined as Co reduced clusters big enough to nucleate SWNT.

The formation of the carbide completes in few minutes and the reaction is auto-catalyzed by the formation of Mo_2C and metallic Co that can dissociate CO more readily than the oxidic species. Even if the catalyst is not considered active during this step, it is necessary to include it due to its fundamental aspect and the large production of CO_2 associated with this step. We can consider a model reaction as follows:

$$\begin{cases} 2MoO_2 + 6CO \rightarrow Mo_2C + 5CO_2 \\ CoO + CO \rightarrow Co + CO_2 \end{cases}$$

Fixing a stoichiometry (e.g. considering MoO_2 instead MoO_3) allows us having a material balance in good agreement with the total amount of carbon generated. This increases the significance of the numerical fitting of the model as we will see later in the chapter. Considering the phase evolution studied in Chapter 3, after the pre-reduction step, the main oxidic phase observed by XRD is MoO_2, so this assumption seems reasonable.

5.1.2. Catalyst Activation:

This step takes into consideration the creation of active sites in the CoMoCAT® process, following the transformation of the $CoMoO_x$ precursor into the active species (i.e. reduced Co clusters) and will be modeled in terms of the conversion of cobalt oxidized ions (L_{inact}) into active (reduced) clusters (L_{act}). Inside this step are included at least two processes: the final reduction of the Co ions released by the carbide phase and the agglomeration of these atoms to form clusters that are the final active sites. The reduction of the Co ions is expected to be very fast, considering the strong reducing environment (CO) and the elevated temperature. From this assumption, we can think that the rate limiting step is probably the agglomeration of atoms forming a well-formed cluster. So, the rate effectively measured is the rate of growth of Co clusters instead of the reduction from the oxide to metallic. After the cluster is formed, we can define the new gas/solid interface as interface 1 (see schematic in figure 5.1.

The balance of surface sites can be summarized as follows:

$$L_{inact} \xrightarrow{k_a} L_{act} \xleftrightarrow{k_d\,,k_r} L_{deact}$$

where L_{inact} is the molar concentration of surface sites (mol sites/g. cat) present on the catalyst, L_{act} is the concentration of reduced active sites, and L_{deact} is the concentration of reduced but deactivated sites. It is assumed that the reduction step is irreversible, but the deactivation is reversible by the CO_2 - C reaction. As mentioned before, only the supercritical clusters are active for the SWNT growth.

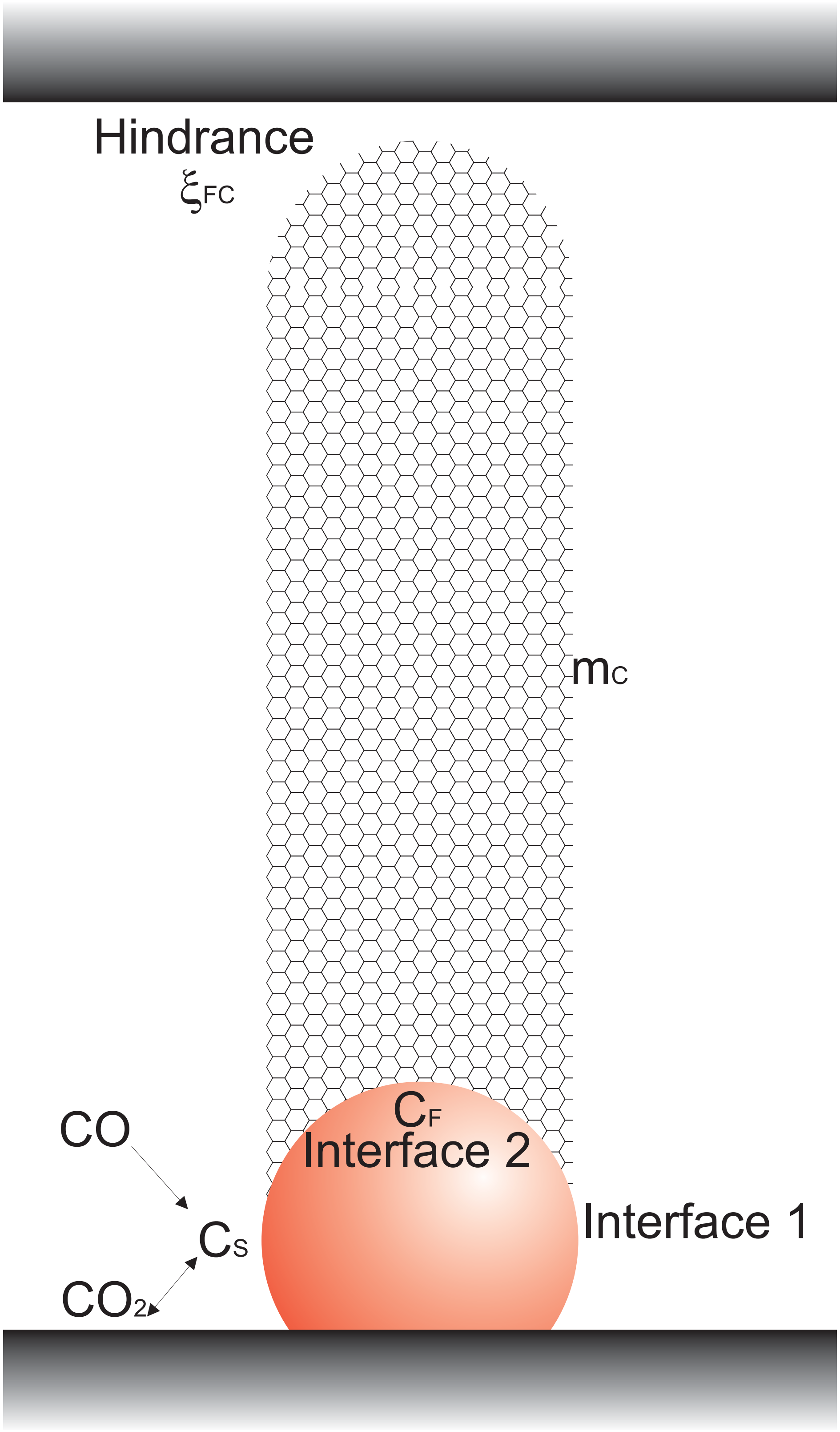

Figure 5.1 Schematic of the SWNT growth mechanism. Two interfaces: gas-metal (1) and metal-SWNT (2) are used to model the process whose driving force is the difference C_S-C_f.

5.1.3. Decomposition of CO over the surface of the reduced Co cluster (interface 1) generating surface carbon species:

While in the text, we refer to carbon concentration, the most correct term would be "surface fugacity" because the thermodynamic activity of these carbon species is not simply the concentration in equilibrium with the gas phase CO, but rather is the result of the several phenomena that occur on the surface; they are i) the CO decomposition that generates surface C, ii) the C diffusion (both across the surface and into the metal particle), and iii) the reverse Boudouard reaction of C with gas phase CO_2. The first one causes an increase in the carbon surface fugacity, the last two act as releasing paths for carbon and help keeping a fraction of the surface clean.

5.1.4. Carbon diffusion, nucleation and growth of SWNT:

After the carbon concentration has reached a certain threshold, nucleation of ordered forms of carbon occur (e.g. hexagons [1,2]). The formation of these nuclei generates a new interface between the catalyst surface and the nanotube (L_{red}/SWNT, interface 2 in figure 5.1). The carbon flux is maintained because the nanotube structure provides a thermodynamic sink for the carbon and as a result the carbon concentration at the interface 2 is kept low.

5.1.5. Growth Termination:

Based on the concept of two interfaces, we can envision two forms of nanotube growth termination. The first type of termination would occur at interface 1 by deactivation of the catalyst active sites, which results in the decrease of the fugacity Cs. The second type would occur at interface 2 when the carbon concentration, C_F, raises and approaches C_S, thus eliminating the driving force for diffusion. As discussed below, the raising in C_F may be due to a mechanical interference of the nanotube growth with its environment, which would hinder the free path of C through the catalyst-nanotube interface 2.

5.2. Mathematical description of the model

5.2.1. Carburization

Even if the carburization step doesn't generate SWNT, it has a fundamental role in the activation of the catalyst: i.e. it reduces the MoO_x lattice to Mo_2C and reduces the Co^{2+} ions to metallic Co. The number of potential active sites for the growth of SWNT is proportional to the reduction of the catalyst L_{red}. Furthermore, during the carburization a large amount of CO_2 is produced due to the reduction process:

$$\begin{cases} 2MoO_2 + 6CO \rightarrow Mo_2C + 5CO_2 \\ CoO + CO \rightarrow Co + CO_2 \end{cases}$$

Resulting in thr production of 2.5 moles of CO_2 per mole of Mo and 1 mole of CO_2 per mole of Co. Measuring the CO_2 evolved during the reaction is our only medium to monitor the kinetic, being the CO in large excess and the C retained onto the catalyst, so a correction for the CO_2 evolved during this step should be considered.

To model the carburization process, we decided to use a simple equation proposed by Proute and Tompkins. [3-5] This model can be expressed in terms of two parameters, k_c and K, and takes into account the autocatalytic effect of the metallic phase during the reduction/carburization step.

The main equations of the model are the following:

Defining a degree of carburization:

$$\alpha = \frac{L_{ox_0} - L_{ox}}{L_{ox_0}} = \frac{L_{car}}{L_{ox_0}}$$ **Equation 5.1**

According to Protue and Tompkins the rate of carburization can be expressed:

$$\frac{d\alpha}{dt} = k_c \cdot (1-\alpha)(1+K\alpha)$$ **Equation 5.2**

Where the term (1-α) represent the consumption of oxidic phase and so reduces the rate for lack of reactants at increasing α, while the term (1+Kα) is the autocatalytic term, that increase the rate at increasing α. So the evolution of degree of carburization along time, which represents the activation of the catalyst, is:

$$\alpha = \frac{1-\exp(-\psi_c \cdot t)}{1+K \cdot \exp(-\psi_c \cdot t)}$$ **Equation 5.3**

where:

$$\psi_c = (1+K) \cdot k_c$$ **Equation 5.4**

And it represent the kinetic constant for the carburization process. Again, from equation 3 the rate of carburization along time is:

$$\frac{d\alpha}{dt} = \frac{(1+K)\cdot\psi_c\cdot\exp(-\psi_c\cdot t)}{(1+K\exp(-\psi_c\cdot t))^2}$$ **Equation 5.5**

The amount of CO_2 evolved during the carburization step can be written as:

$$r_{carb} = \varepsilon_{carb} r^*_{carb}\frac{d\alpha}{dt} = \varepsilon_{carb} r^*_{carb}\frac{(1+K)\cdot\psi_c\cdot\exp(-\psi_c\cdot t)}{(1+K\exp(-\psi_c\cdot t))^2}$$ **Equation 5.6**

Where ε_{carb} is the efficiency of carburization (generally = 1 for total conversion of the oxide to carbide) and r^*_{carb} is the stoichiometric amount of CO_2 producible by the system. This notation, which separates the stoichiometric amount and the fraction of that effectively reduced, allows a quick check of the C balance closure without increasing the complexity of the model. The efficiency term is expected to be low in mild conditions and to increase in harsher conditions (e.g. higher pressure of CO).

5.2.2. Active site formation

The potential activity of the catalyst is related to the degree of carburization:

$$a_p = \frac{L_{ox}}{L_T} = a_{p_0}\cdot(1-\alpha) \quad\Leftrightarrow\quad \alpha = 1-\frac{a_p}{a_{p_0}}$$ **Equation 5.7**

From eq. 7 and 3 results an increase of the potential activity along time:

$$a_p = a_{p_0} \frac{(1+K)\cdot \exp(-\psi_c \cdot t)}{1+K\cdot \exp(-\psi_c \cdot t)}$$ **Equation 5.8**

And (from equation 8) the activation rate along time:

$$-\frac{da_p}{dt} = a_{p_0} \frac{(1+K)\cdot \psi_c \cdot \exp(-\psi_c \cdot t)}{(1+K\exp(-\psi_c \cdot t))^2}$$ **Equation 5.9**

The activation rate can also be expressed in terms of more convenient parameters for the following model as:

$$-\frac{da_p}{dt} = \psi'_a \cdot a_p \cdot (a_p^* - a_p)$$ **Equation 5.10**

where:

$$\psi'_a = \frac{K\cdot \psi_c}{(1+K)\cdot a_{p_0}} \quad ; \quad a_p^* = a_{p_0} \frac{(1+K)}{K}$$ **Equation 5.11**

However this potential activity does not consider the agglomeration of the Co atoms to form an active cluster that can nucleate SWNT. This means chosing the carburization as rate determining step of the activation process, assumption that is probably not true in our case. In a more general way, we can model the transformation L_{inact}→L_{act} as follows:

$$-\frac{dL_{inact}}{dt} = \psi_a \cdot L_{inact}$$ **Equation 5.12**

where ψ_a is the carburization-independent "*activation kinetic function*" that depends on the operating conditions: $\psi_a=\phi_a(T, p_T, p_{CO}, p_{CO2})$. ψ'_a is a "*pseudo activation kinetic function*" that is carburization-dependent. This function (ψ_a) has been typically used in modeling catalysts that involve an induction period [2, 6-10]. In this case, we are using a simple expression of the form:

$$\psi_a = k_a p_{CO}^{m_a} p_{CO_2}^{n_a} \quad ; \quad k_a = k_{a_0} \exp(-E_a/RT) \qquad \textbf{Equation 5.13}$$

In a numerical solution, it is possible to use the expression of ψ_a of equation 13; for a simpler analytical solution, it can be assumed that the reactor operates under differential conditions, i.e. low CO conversion. Therefore, ψ_a can be assumed to be constant. Accordingly, the variation of concentration of sites as a function of time will follow the expression that results from integrating 12:

$$L_{inact} = L_{inact_0} \cdot \exp\left(-\psi_a \cdot t\right) \qquad \textbf{Equation 5.14}$$

where L_{inact0} represents the initial concentration of inactive sites, both oxidized Co and metallic Co that is not agglomerated yet in a cluster.

As the catalyst is being reduced by CO and the atoms agglomerate, $L_{inactive}$ is converted into L_{act} and carbon deposition stars with simultaneous deactivation of some of the sites. Therefore, the net rate of variation of active sites should be expressed as:

$$\frac{dL_{act}}{dt} = \psi_a \cdot L_{inact} - \psi_d \cdot L_{act} + \psi_r \cdot L_{deact} \qquad \textbf{Equation 5.15}$$

L_{act} represents the concentration of active reduced sites (mol red. sites/g. cat), and ψ_d and ψ_r are respectively the *deactivation and regeneration kinetic functions*. These kinetic functions also depend on the operating conditions: $\psi_d=\phi_d(T, p_T, p_{CO}, p_{CO2})$ and $\psi_r=\phi_r(T, p_T, p_{CO}, p_{CO2})$. In the simplest forms, they can be assumed to follow the typical functionality shown in equation 16:

$$\begin{aligned} \psi_d &= k_d\, p_{CO}^{m_d} \quad ; \quad k_d = k_{d_0} \exp(-E_d/RT) \\ \psi_r &= k_r\, p_{CO_2}^{m_r} \quad ; \quad k_r = k_{r_0} \exp(-E_r/RT) \end{aligned} \qquad \textbf{Equation 5.16}$$

Here, it is assumed that the deactivation rate is a direct function of the CO concentration and that regeneration of sites can occur via reverse reaction of C with CO_2.

To solve equation 15, we can use the site balance and express the concentration of deactivated sites, L_{deact}, in terms of L_{inact} and L_{act}. The balance of total sites, at $t=0$ and at a given time t, can be expressed as:

$$L_T = L_{inact_0} + L_{act_0} \quad ; \quad t = 0$$
$$L_T = L_{inact}(t) + L_{act}(t) + L_{deact}(t) \quad ; \quad t = t$$

Equation 5.17

We can use again the concept of catalyst activity, *a*, and the potential catalyst activity a_p. These terms are typically used in kinetic analysis in which there is change in the number of active site as a function of time of reaction (see for example [11-14]). The catalyst activity is the fraction of active sites, and the potential catalyst activity is the fraction of inactivated sites still available to be activated:

$$a = \left(\frac{L_{act}}{L_{inact_0} + L_{red_0}} \right) = \frac{L_{act}}{L_T}$$
$$a_p = \left(\frac{L_{inact}}{L_{inact_0} + L_{act_0}} \right) = \frac{L_{act}}{L_T}$$

Equation 5.18

Now, the balance of active sites can be rewritten as:

$$a + a_p = 1 - (L_{deact} / L_T)$$

Equation 5.19

and the equation 12 and 14, as follows:

$$-\frac{da_p}{dt} = \psi_a \cdot a_p$$
$$a_p = (1 - a_0) \cdot \exp(-\psi_a \cdot t)$$

Equation 5.20

If we compare equations 20 and 10 we can see that there is an apparent incongruence in the definition of the potential activity from an active site balance and from the result of the carburization process. However plugging the meaning of a^*_p and ψ'_a (equation 11) in equation 10 results:

$$-\frac{da_p}{dt} = \psi_c \cdot a_p - \frac{K\psi_c a_p^2}{(1+K)a_{p0}} \qquad \textbf{Equation 5.21}$$

that approaches quickly equation 20 for small values of a_p, when the second order term becomes negligible. This is especially true when the carburization process is faster than the nucleation of the Co ions forming larger clusters, so it is not the rate determining step of the activation process. This means that Equation 20 considers as rate determining step the agglomeration of ions forming an active cluster, a process that is not auto-catalyzed, while equation 10 considers as rate determining step the generation of ions due to the carburization, which is an auto-catalyzed process. In our experimental conditions, the carburization is observed to be very fast so we can assume as rate determining step the agglomeration of ions forming active clusters. Thus, to obtain an analytical solution of the model, we can consider the potential activity expression obtained in equation 20, otherwise a numerical solution can be found using equation 21.

Using the definitions of equations 18, equation 15 can be rewritten as follows:

$$\frac{da}{dt} = \psi_a \cdot a_p - \psi_d \cdot a + \psi_r (1 - a_p - a) \qquad \textbf{Equation 5.22}$$

and substituting equation 20 it is obtained that:

$$\frac{da}{dt}+(\psi_d+\psi_r)\cdot a=\psi_r+(\psi_a-\psi_r)\cdot(1-a_0)\cdot\exp(-\psi_a\cdot t)$$ **Equation 5.23**

As described above ψ_a, ψ_d and ψ_r can be kept with their functionalities in the numerical solution. However, for a simpler analytical solution we can consider them constant. In this case the solution of equation 23, is:

$$a=a_S+\alpha_1\cdot\exp(-\psi_a\cdot t)+\alpha_2\cdot\exp(-\psi_G\cdot t)$$ **Equation 5.24**

where:

$$\psi_G=\psi_d+\psi_r \quad ; \quad a_S=\frac{\psi_r}{\psi_d+\psi_r}=\frac{\psi_r}{\psi_G}$$ **Equation 5.25**

with ψ_G being a *global kinetic constant* ($\psi_d+\psi_r$), and α_1 and α_2, two dimensionless constants defined as:

$$\alpha_1=(1-a_0)\cdot\left(\frac{\psi_a-\psi_r}{\psi_G-\psi_a}\right) \quad ; \quad \alpha_2=(a_0-a_S-\alpha_1)$$ **Equation 5.26**

The above expression for catalytic activity can be simplified for specific cases. For example, let's find the expression for catalyst activity as a function of reaction time for the following cases:

Case 1). The initial activity is negligible ($a_0=0$), the catalyst is activated under reaction conditions, with parallel irreversible deactivation ($\psi_r=0$, a_S=0). Under these conditions, equation 24 became:

$$a=\frac{\psi_a}{\psi_d-\psi_a}\exp(-\psi_a\cdot t)-\frac{\psi_a}{\psi_d-\psi_a}\exp(-\psi_d\cdot t) \qquad \textbf{Equation 5.27}$$

Case 2). The catalyst does not deactivate and only undergoes the activation step. Therefore $\psi_d= \psi_r=0$:

$$a=1-(1-a_0)\cdot\exp(-\psi_a\cdot t) \qquad \textbf{Equation 5.28}$$

Case 3.a). The catalyst initially is totally activated, $a_0=1$, $\psi_a=0$, and the activity varies according to the DMRA (deactivation model with residual activity) model [12-14]

$$a=a_S+(1-a_S)\cdot\exp(-\psi_G\cdot t) \qquad \textbf{Equation 5.29}$$

Case 3.b) The deactivation process is irreversible. Then $\psi_r=0$:

$$a=\exp(-\psi_d\cdot t) \qquad \textbf{Equation 5.30}$$

Figure 2 illustrates the time evolution of catalyst activity for the special cases described above. The values of the parameters used for the general case (case 0) were: ψ_a=0.01, ψ_d=0.002, ψ_r=0.0003 and a_a=0. For case 1, the parameters were: ψ_a=0.01, ψ_d=0.002, ψ_r=0 and a_a=0. For case 2, ψ_a=0.01, ψ_d=0, ψ_r=0 and a_a=0; and for Case 3 ψ_a=0, ψ_d=0.002, ψ_r=0.0003 and a_a=1.

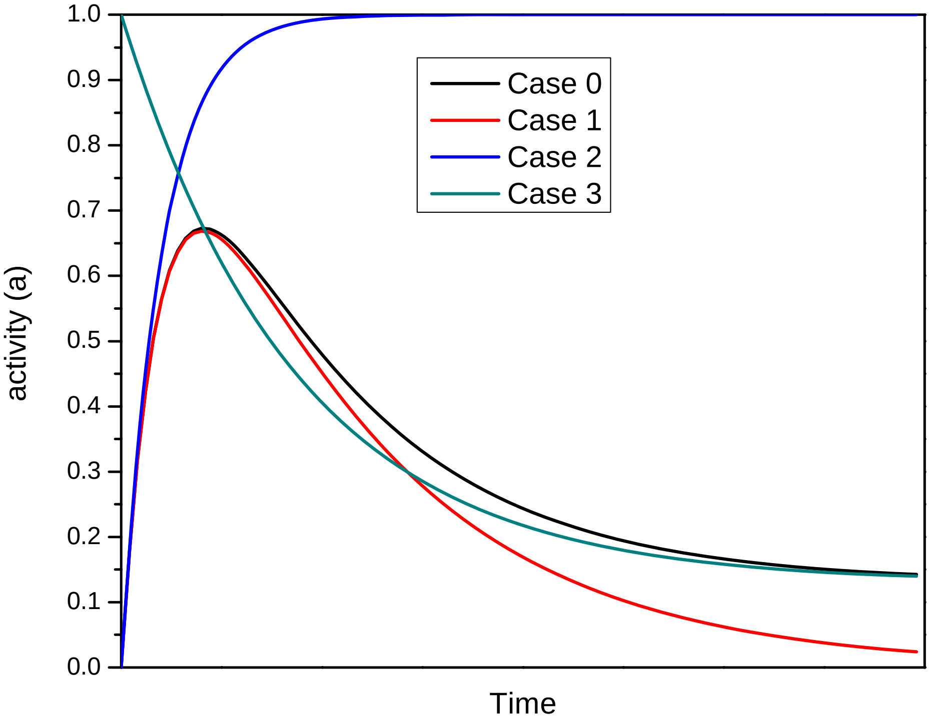

Figure 5.2 Prediction of activity based on different cases

5.2.3. Rate of carbon deposition at interface 1:

After having developed an expression for the catalyst activity for the specific case, we can calculate the net rate of CO disproportionation on the surface using a typical rate expression for the Boudouard reaction: [15]

$$(-r_{CO})_t = (-r_{CO})^0 \cdot a = k_1 \cdot \left(p_{CO} - \frac{p_{CO_2}}{K_{eq} p_{CO}} \right) \cdot a$$

$$k_1 = k_{1_0} \cdot \exp(-E_1/RT) \quad ; \quad K_{eq} = \frac{k_1}{k_2} = \exp(-\Delta G/RT)$$

Equation 5.31

The term $(-r_{CO})^0$ represents the reaction rate of CO decomposition when the catalyst activity is 1, i.e. when is totally activated and before any deactivation process. Therefore, $(-r_{CO})^0$ is a constant value for a given operating conditions. In the case that the catalyst initially will be totally activated (a_0=1), this value is the initial reaction rate. Given the high reaction temperature at which the reaction is carried out, the CO and CO_2 chemisorptions' terms can be neglected in the rate expression.

From the effective rate of CO disproportionation, eqn. 31, and taking into account the stoichiometry of the reaction (2 CO **:** 1 C), the rate of carbon accumulated on the active metallic surface can be calculated as:

$$\frac{dC_S}{dt} = r_C = \frac{(-r_{CO})}{2} = \psi_S \cdot (C_{S_0} \cdot a - C_S) \qquad \textbf{Equation 5.32}$$

In the above equation, the term ψ_S represents the intrinsic kinetic function of the CO disproportionation over the metallic surface. We have considered that the rate of carbon deposition over the surface is proportional to the free surface and to the number of the available active sites to the reaction, i.e. the catalyst activity. Thus, the term C_{S0} expresses the maximum surface concentration of carbon that can be formed over the fresh catalyst (i.e. without deactivation after total activation). This carbon concentration depends of the total active surface exposed by the catalyst. Therefore, if the catalyst is deactivated by the formation of encapsulating coke and/or by sintering, the exposed metallic surface will be diminished.

The evolution of C_S can be calculated solving the differential equation derived from the equation 32:

$$\frac{dC_S}{dt} + \psi_S \cdot C_S = \psi_S \cdot C_{S_0} \cdot a$$ **Equation 5.33**

In this equation, the evolution of the catalyst activity is given by the equation 24.

The solution of equation 33 is given by the following expression:

$$C_S(t) = C_{S_0} \begin{bmatrix} a_S + \dfrac{\psi_S \cdot \alpha_1}{(\psi_S - \psi_a)} \exp(-\psi_a t) + \\ + \dfrac{\psi_S \cdot \alpha_2}{(\psi_S - \psi_G)} \exp(-\psi_G t) - \alpha_3 \exp(-\psi_S t) \end{bmatrix}$$ **Equation 5.34**

where the term α_3 is given by:

$$\alpha_3 = a_S + \frac{\psi_S \cdot \alpha_1}{(\psi_S - \psi_a)} + \frac{\psi_S \cdot \alpha_2}{(\psi_S - \psi_G)}$$ **Equation 5.35**

5.2.4. Carbon diffusion and formation of SWNT at interface 2

This stage represents the diffusion of carbon atoms through the metallic crystallites or surface diffusion over the metal and in turn determines the rate of formation of SWNT. The rate for this step can be expressed as:

$$r_{C_{SWNT}} = \frac{dm_C}{dt} = k_C (C_S - C_F)$$ **Equation 5.36**

where k_C is the effective transport coefficient of carbon on the Co particles and depends on the average size of the Co crystallites, d_{met}, the metallic exposed area,

S_{met}, and of the carbon diffusivity of carbon on the metallic particle. $D_{C,met}$. In general,

$$k_C \approx (S_{met} \cdot \rho_{met}) \cdot \left(D_{C,met} / \overline{d_{met}}\right)$$ **Equation 5.37**

The carbon concentration at interface 2 is termed C_F, which has an initial value of zero and increases with time. However, when C_F reaches a value high enough to favor nucleation, formation of SWNT begins. As a result, a carbon sink is formed at this interface and $C_F < C_S$.

If we consider $C_F \cong 0$, or also constant in time, we can directly solve equation 36 plugging equation 34 for the value of C_S:

$$r_{C_{SWNT}} = j_{C_0}\left[a_S + \frac{\psi_S \cdot \alpha_1}{(\psi_S - \psi_a)}\exp(-\psi_a t) + \frac{\psi_S \cdot \alpha_2}{(\psi_S - \psi_G)}\exp(-\psi_G t) - \alpha_3 \exp(-\psi_S t)\right]$$

$$j_{C_0} = k_C \cdot C_{S_0}$$ **Equation 5.38**

The tem j_{C0} represents the maximum allowable carbon flux (g_C / g_{cat} s) that can be obtained through the metallic particles of the catalysts.

The total CO_2 evolution is the sum of the contribution from carburization and from SWNT growth:

$$r_{C_{tot}} = r_{C_{SWNT}} + r_{C_{carb}}$$ **Equation 5.39**

The resulting CO_2 production rate can be simulated, for example, using the following parameters (Figure 5.3): ψ_a=1; ψ_S=0.5; ψ_d=0.05; ψ_r=0.005; ψ_c=5; K=100.

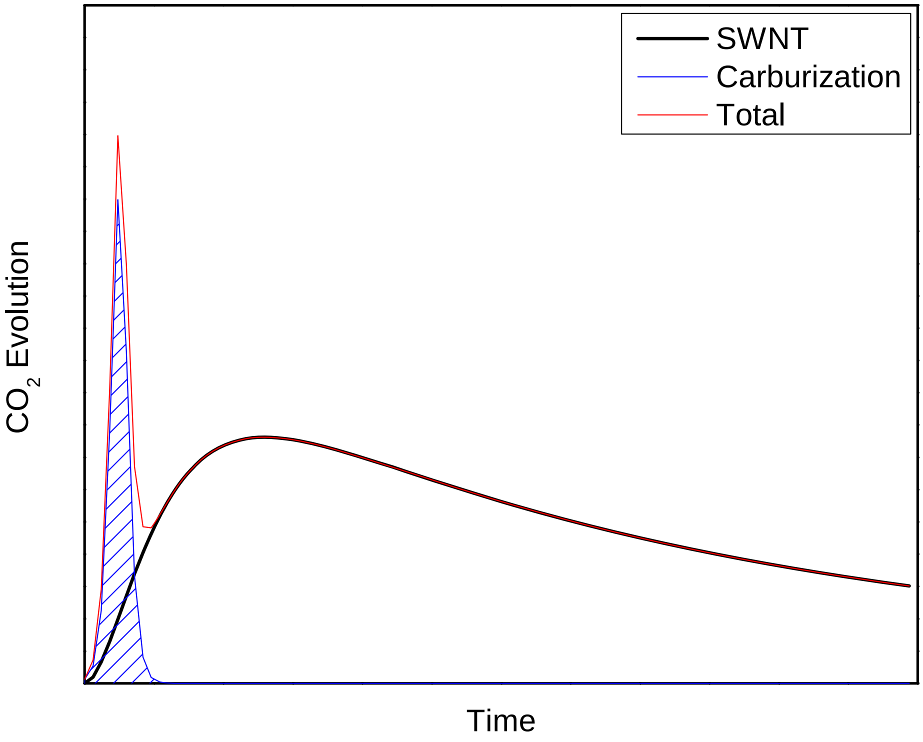

Figure 5.3 Prediction of CO_2 evolution for the CoMoCAT® process using the model developed in equations 5.6, 5.38, and 5.39.

However, it is possible that, as carbon accumulates by increasing length and number of SWNT, physical hindrance for nanotubes displacement may occur, thus making more difficult the insertion of new carbon atoms at interface 2. One may speculate that the magnitude of this hindrance may be a function not only of the length and number of SWNT, but also of the nature of the surrounding environment at the growing site. That is, the interaction of a growing SWNT with the catalyst support and/or with other nanotubes may vary depending on the pore size of the catalyst, the metal content, etc. The larger is the volume of nanotubes compared to the available space the more restricted will be the insertion of new carbon atoms at the interface.

In fact, there have been several examples in which individual SWNT has been allowed to grow practically free of interaction with the catalyst surface or other nanotubes. For example, Liu et al. [16,17] have grown SWNT in the 1-2 cm range when the catalyst was deposited on an edge by photolithography and the growing SWNT was suspended in the flowing gas, thus avoiding hindering its growth by interaction with neither other nanotubes nor the substrate surface. The authors called this phenomenon “kite-mechanism” to illustrate the growth of a long nanotube tail, aligned in the direction of the flow. Other examples of long SWNT have been observed when the substrate is flat and the growing end is open. [18,19] By contrast, when the growth is conducted on a typical high-surface-area porous catalyst, the growth process is eventually impeded by the lack of space for displacement inside the pores and tube-tube interactions.

To take into account these considerations, we assume that the value of C_F is proportional to the amount of carbon accumulated with a proportionality constant ξ_F that depends on the structure of the catalyst substrate and how the growing SWNT accommodate in such structure. Therefore,

$$C_F = \xi_F \cdot m_C$$ **Equation 5.40**

Accordingly, for an open structure, with very low hindrance for the growth of the SWNT, ξ_F should be low. By contrast, for a constricted catalyst structure (e.g. low pore volume), ξ_F should take higher values.

This is an interesting result and presents an alternative possibility to explain the typically observed saturation of SWNT growth, which is commonly ascribed to catalyst deactivation only. [20] More recently Iijima et al. [21] have indicated that they have obtained maximum catalyst utilization when the catalyst particles are sparse, a concept which is in line with our quantifiable hindrance factor (ξFC). The influence of this factor is clearly envisioned when the growth occurs inside a catalyst pore, but it may also be applicable in the case of nanotube forest growth on flat surfaces. As we have previously shown [22], the nanotubes in the forest grow connected to each other by a crust that forms on the top. The mechanical constriction that this crust imposes to the growing nanotubes may also be described in terms of a hindrance factor.

Continuing from equation 36:

$$\frac{dm_C}{dt} + \xi_{FC} m_C = k_C C_S \qquad \textbf{Equation 5.41}$$

where:

$$\xi_{FC} = \xi_F \cdot k_C \qquad \textbf{Equation 5.42}$$

After substitution of equation 34 into equation 41, the analytical solution of equation 41 is:

$$m_C = j_{C_0} \begin{bmatrix} A_0 + A_1 \exp(-\psi_a t) + A_2 \exp(-\psi_G t) - \\ - A_3 \exp(-\psi_S t) - A_4 \exp(-\xi_{FC} t) \end{bmatrix} \qquad \textbf{Equation 5.43}$$

The constants appearing in the above equation are given by the following expressions:

$$j_{C_0} = k_C \cdot C_{S_0} \quad ; \quad A_0 = \frac{a_S}{\xi_{FC}}$$
$$A_1 = \frac{\alpha_1 \cdot \psi_S}{(\psi_S - \psi_a)(\xi_{FC} - \psi_a)}$$
$$A_2 = \frac{\alpha_2 \cdot \psi_S}{(\psi_S - \psi_G)(\xi_{FC} - \psi_G)} \qquad \textbf{Equation 5.44}$$
$$A_3 = \frac{\alpha_3}{(\xi_{FC} - \psi_S)}$$
$$A_4 = A_0 + A_1 + A_2 - A_3$$

The rate of SWNT production is directly obtained from the derivative of the equation 43:

$$r_{C_{swnt}} = \frac{dm_C}{dt} = r_{C_0} \begin{bmatrix} -\psi_a A_1 \exp(-\psi_a t) - \psi_G A_2 \exp(-\psi_G t) + \\ + \psi_S A_3 \exp(-\psi_S t) + \xi_{FC} A_4 \exp(-\xi_{FC} t) \end{bmatrix} \textbf{Equation 5.45}$$

Again, the total rate of CO_2 evolution observed at the exit of the reaction would be the sum of the rate due to SWNT growth from equation 45 and carburization of the catalyst oxidic phase from equation 6:

$$r_{C_{tot}} = r_{C_{SWNT}} + r_{C_{carb}} \qquad \textbf{Equation 5.46}$$

An example of simulation is shown in Figure 5.4. The parameters are: ξ_{FC}=0.1; ψ_a=1; ψ_S=0.5; ψ_d=0.005; ψ_r=0.0005; ψ_c=5; K=100. We can also see the large effect of the hindrance factor, using the same parameters but setting ξ_{FC}=0. From the inset we can also see that the effect of the hindrance factor shows its influence only at long time, when the carbon buildup is large, according to equation 5.40.

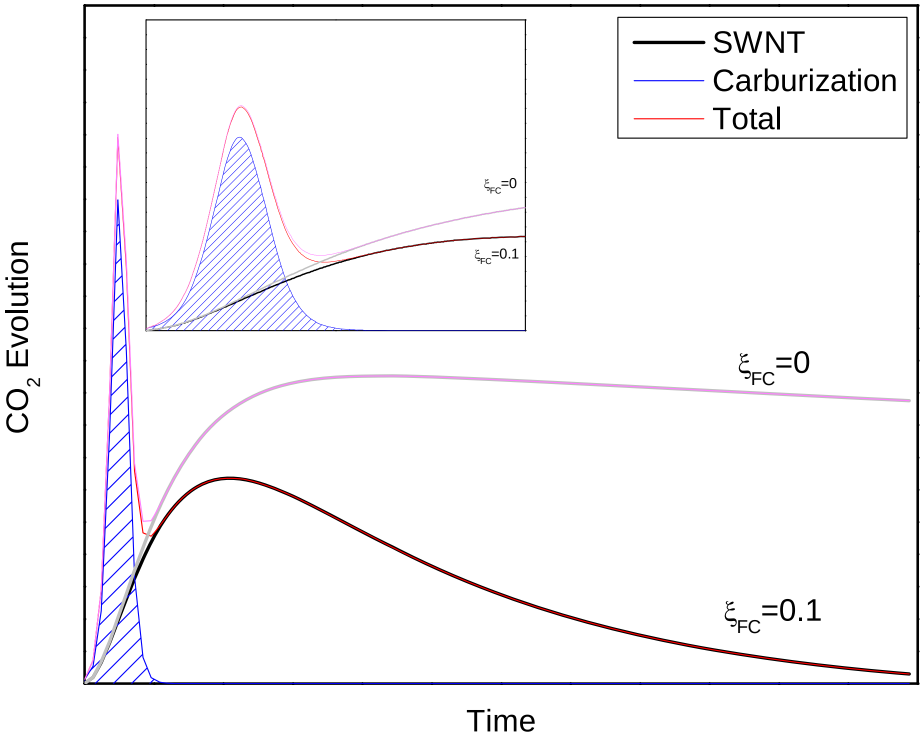

Figure 5.4 Prediction of CO_2 evolution for the CoMoCAT® process using the model developed in equations 5.6, 5.45, and 5.46. The effect at long time of the hindrance factor is evidenced.

5.3. Numerical fitting of the model

A series of experiments have been conducted in different operating conditions, monitoring the evolution of CO_2 during the reaction at increasing operating pressures. Due to the change of the residence time distribution, affected by the apparent reactor and line volumes, the raw data obtained from the mass spec has to be deconvoluted to correlate the measured data with the real kinetic inside the reactor. The detailed mathematical procedure is explained in the Appendix, and is fundamental to obtain comparable data at different operating conditions.

A typical rate profile in function of time is shown in figure 5.5. We can see that there are clearly 2 regions: a sharp production of CO_2 in the first minutes that is associated with the carburization of the oxidic phase ($r_{C_{carb}}$) and an activation - deactivation profile that is associated with the growth of SWNT ($r_{C_{swnt}}$). This behavior is consistent with the simulations we presented in figures 5.3 and 5.4.

To separate these two effects, we can fit the data using the expression found in equation 46 above. The fitting parameters are reported in table 5.1. We can clearly see the carburization step (shaded region) and the real kinetics of growth of SWNT (bold line). All the errors are calculated for a 95% confidence interval.

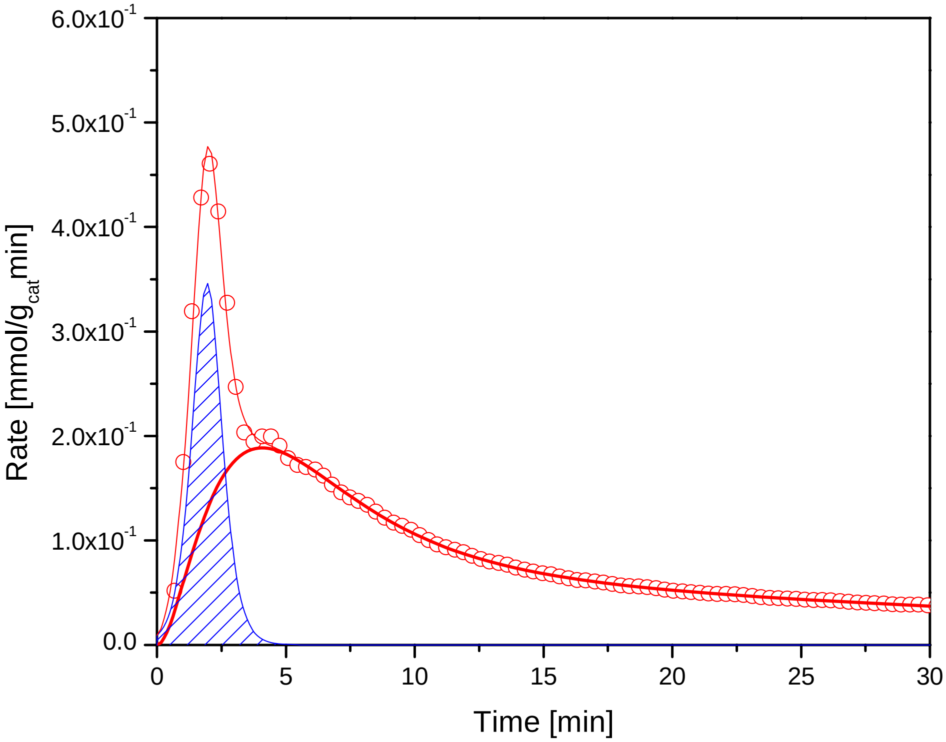

Figure 5.5 Typical MS profile obtained at 20 psig CO pressure. Are evidenced the carburization of the oxide phase (blue shaded region) and the SWNT growth (bold red line).

χ^2/DoF	5.8244 10^{-11}
R^2	0.99328

Carburization

$r{*}_{carb}$	$5.33 \cdot 10^{-4}$	$\pm 7.63 \cdot 10^{-5}$
K	151	±56.4
ϵ	1	±0‡
ψ_c	2.58	±0.177

SWNT

ψ_a	0.765	±30.6
ψ_d	0.181	±0.202
ψ_r	0.086	±0.070
ψ_S	0.0290	±0.0286
j_{C0}	0.0093	±0.375
ξ_{FC}	0.788	±31.8

Mass Balance

Carburization	
Fit	Measured
0.53 mmol	0.49 mmol

SWNT	
Fit	Measured
3.01 mmol	3.05 mmol

‡ Fixed to 1 due to redundancy with $r{*}_{carb}$

Table 5.1. Fitting result from Figure 5.3; the mass balance closes very well validating the fitting.

As we can see from table 1, the closure of the mass balance validates the fitting: for the carburization step the fitted values of the shaded area compare very well with the amount calculated using the stoichiometric reaction described before:

$$\begin{cases} 2MoO_2 + 6CO \rightarrow Mo_2C + 5CO_2 \\ CoO + CO \rightarrow Co + CO_2 \end{cases}$$

The remaining area (under the bold line) is very similar to the experimental data obtained by TPO, that is, the effective amount of SWNT present on the sample. In this case the amount of CO_2 evolved by the oxidation of the carbide is negligible compared to the one from SWNT:

$$\begin{cases} Mo_2C + 4O_2 \rightarrow 2MoO_3 + CO_2 \\ C_{SWNT} + O_2 \rightarrow CO_2 \end{cases}$$

In addition to the validation of the mass balance, the importance of the fitting is the possible physical meaning of the adjustable parameters. However the large autocorrelation among the parameters makes this significance less certain. This is due to the large number of independent variables present in the model. Both, the model from equation 5.45 and equation 5.38 (setting ξ_{FC}=0) present similar autocorrelation. A way to reduce this autocorrelation and increase the physical meaning of the model is performing a multiple dataset fitting sharing the parameters that are independent from the operating condition that is changed between the sets. In our specific case 6 experiments were performed at increasing pressures: from 0 psig to 100 psig at steps of 20 psig. The carbon yield increases almost linearly (Figure 4.2) and the chirality distribution moves towards smaller SWNT (Figure 4.3). Obtaining kinetic data for this series can increase our understanding of the activation and deactivation process and help in the control of Type I and Type II selectivity.

A first simple fitting can be performed using equation 5.38 (so not considering the hindrance effect). This fitting allows for seeing if there are differences between the activation-deactivation kinetic. The hindrance factor in this case will tend to mask the effect of the deactivation, modeling a similar behavior. The fitting is shown in figure 5.6 and the numerical results are summarized in table 5.2. The carburization was fixed to the best values obtained in previous fittings.

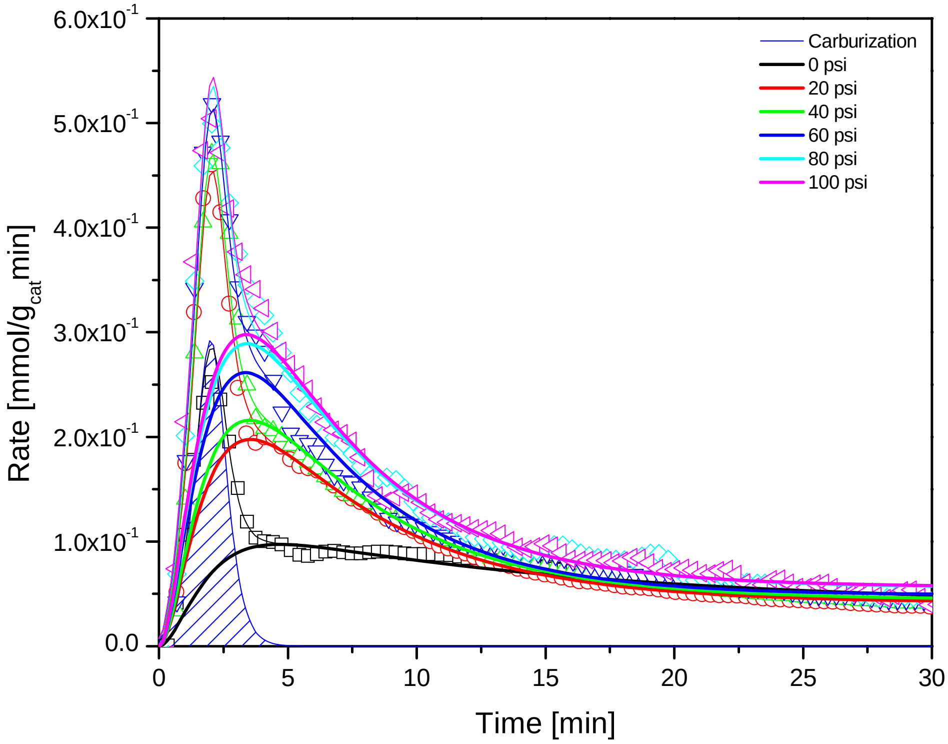

Figure 5.6 Fitting of the experimental datasets using the model proposed in Equation 5.38.

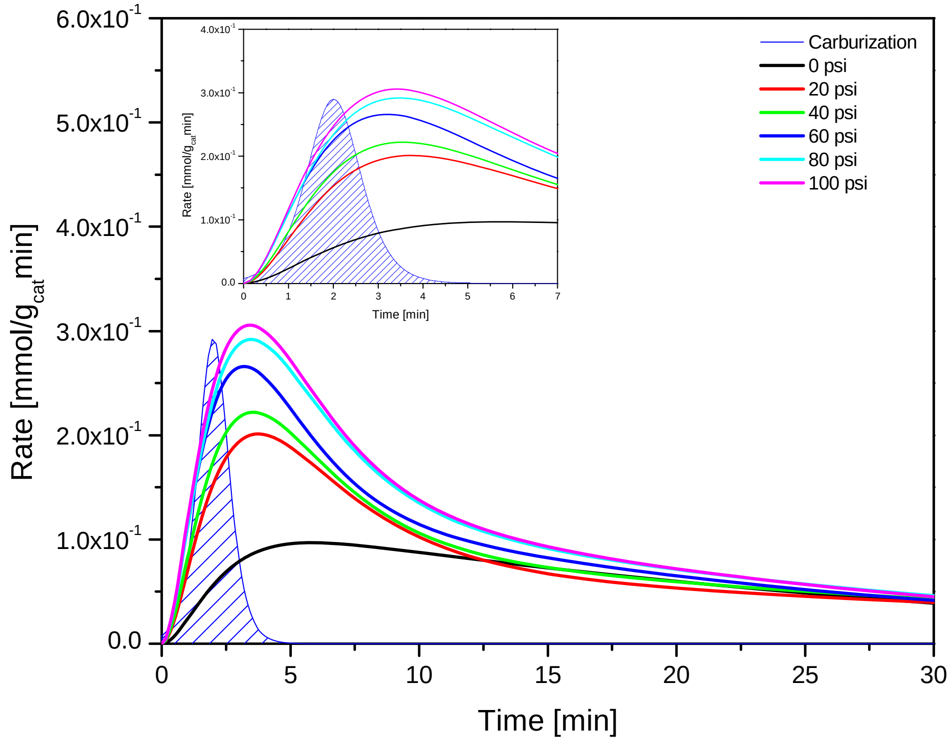

Figure 5.7 Simulated data for the fitting of Figure 5.6. Inset is a magnification of the first minutes.

χ^2/DoF	1.4610^{-10}
R^2	0.98459

Shared parameters

Carburization		
$r{*}_{carb}$	$4.62 \cdot 10^{-4}$	±0‡
K	156	±0‡
ϵ†	0.739	±0‡
ψ_c	2.52	±0‡
SWNT		
ψ_a	1.04	±739!
ψ_S	1.04	±739!
ψ_r	0.0245	±0.00113

Variable parameters

pressure	ψ_d		j_{C0}	
0	0.049	±0.0047	$1.17 \cdot 10^{-4}$	$\pm 4.80 \cdot 10^{-6}$
20	0.152	±0.0091	$2.97 \cdot 10^{-4}$	$\pm 1.16 \cdot 10^{-5}$
40	0.157	±0.0092	$3.29 \cdot 10^{-4}$	$\pm 1.25 \cdot 10^{-5}$
60	0.185	±0.0106	$4.17 \cdot 10^{-4}$	$\pm 1.62 \cdot 10^{-5}$
80	0.174	±0.0097	$4.53 \cdot 10^{-4}$	$\pm 1.66 \cdot 10^{-5}$
100	0.179	±0.0099	$4.70 \cdot 10^{-4}$	$\pm 1.74 \cdot 10^{-5}$

† ϵ is 0.739 at 0 psi and fixed to 1 for pressures above 0 psi

‡ Fixed parameters

! Strong autocorrelation between parameters

Table 5.2 Numerical results of the fitting of Figure 5.6.

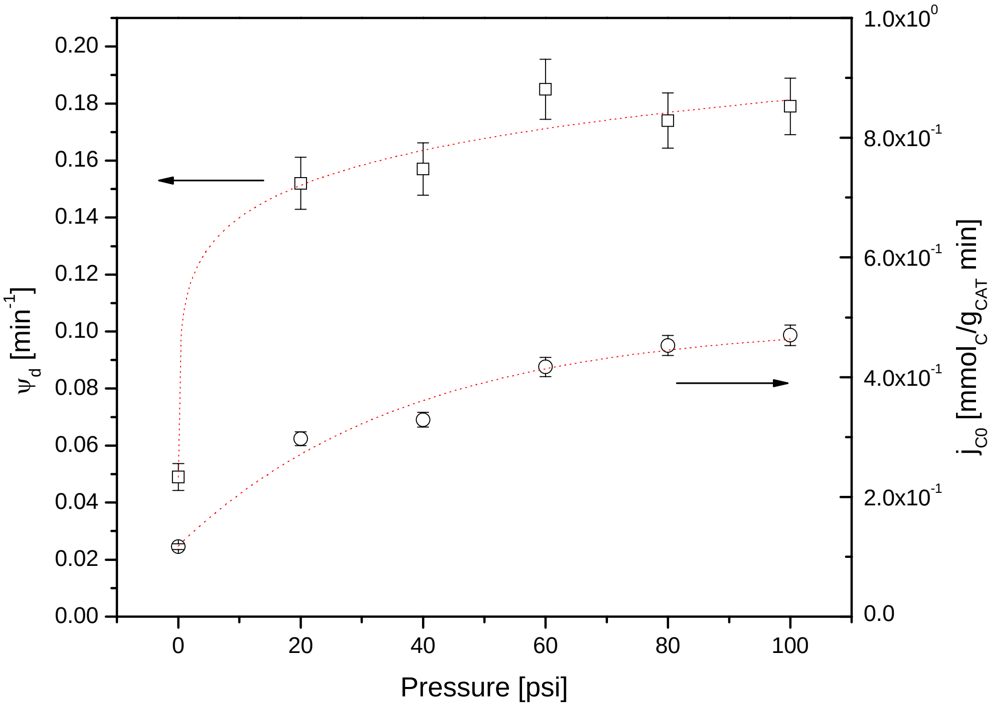

Figure 5.8 Graphical representation of the trend from table 5.2.

Besides the strong autocorrelation between activation and surface reaction, due to the mathematical expression of equation 5.38, which contains the difference (ψ_a-ψ_s), and the small number of datapoints available at short times, there is a clear trend in the deactivation kinetic function and the maximum transport term j_{C0}, both increase with pressure (Figure 5.8). The first one is explained by the increased carbon deposition that can consequently deactivate the surface due to coverage. The second one is an effect of the different activation of the catalyst: an increased number of sites will correspond to an increased surface for the diffusion of carbon, so a larger transport term. This trend is the same followed by the carburization efficiency, meaning that at low pressures not all the catalyst is activated and consequently part of it is inactive. This effect is reduced at high pressures where the activation is complete. This means that j_{C0} is expected to reach a plateau at high pressures, in accordance with Figure 5.2.

To study the initial activation of the catalyst, we have to break up the autocorrelation between ψ_a and ψ_s. We can do this by the introduction of the hindrance factor (so using the model proposed in equation 5.45). Mathematically the difference (ψ_a-ψ_s) is substituted by the product (ψ_a-ψ_s)(ψ_a-ξ_{FC}). The hindrance factor now is taking charge of the majority of the long time effects. This method allows us to get a better understanding of the phenomena that happens at the very beginning of the reaction, when there is no carbon deposited and the hindrance is not present.

Repeating the fitting using the model from equation 5.45, and focusing on ψ_a and ψ_s we can obtain the numerical results summarized in table 5.3. The trends are shown in figure 5.9.

χ^2/DoF	1.0910^{-10}
R^2	0.98858

Shared parameters

Carburization		
$r*_{carb}$	$4.62 \cdot 10^{-4}$	±0‡
K	156	±0‡
ϵ†	0.739	±0‡
ψ_c	2.52	±0‡
SWNT		
ψ_r	0.149	±0.0097
j_{C0}	0.0175	±0.003
ξ_{FC}	0.766	±0.425

Variable parameters

pressure	ψ_d		ψ_a		ψ_S	
0	1.100	±0.647	0.101	±0.058	0.057	±0.0315
20	0.884	±0.562	0.356	±0.055	0.047	±0.00292
40	0.770	±0.503	0.429	±0.060	0.043	±0.00262
60	0.659	±0.443	0.598	±0.082	0.042	±0.00264
80	0.598	±0.408	0.517	±0.069	0.046	±0.00258
100	0.585	±0.401	0.544	±0.073	0.045	±0.00263

† ϵ is 0.739 at 0 psi and fixed to 1 for pressures above 0 psi
‡ Fixed parameters

Table 5.3 Results of the fitting to reveal the effect of ψ_a and ψ_S on the reaction rate.

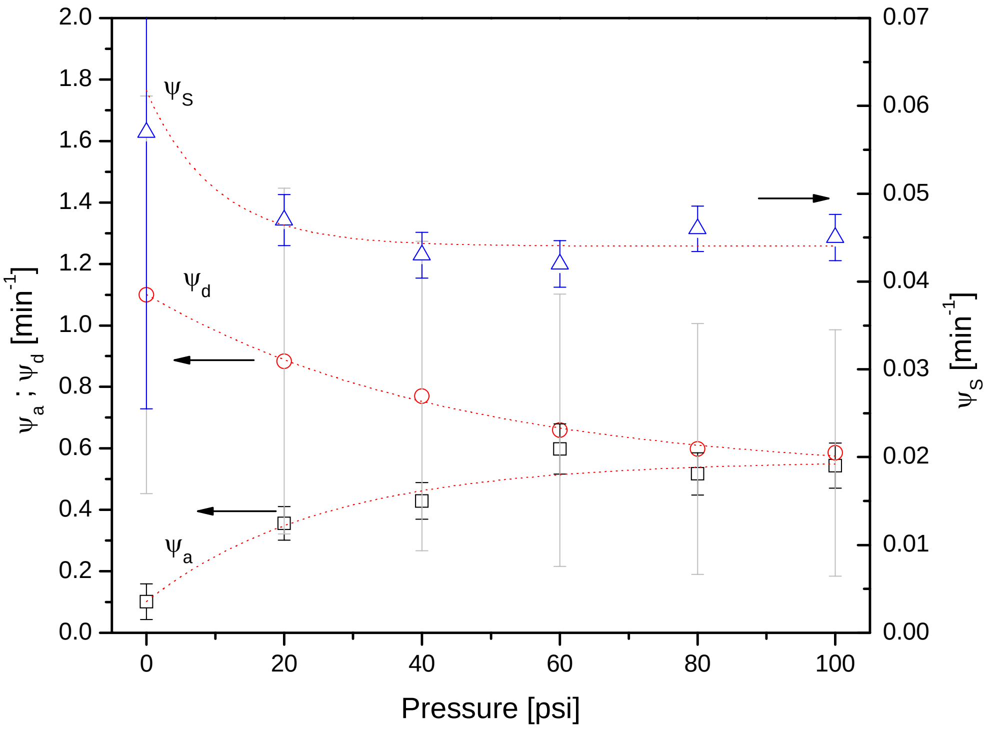

Figure 5.9 Trend of the free parameters in function of the pressure for the fitting of table 5.4.

From the analysis of the data there is a clear increase of the activation kinetic parameter (ψ_a) with pressure. This is in agreement with our observations of a faster nucleation at higher pressures.

We can also observe that the surface reaction kinetic (ψ_s) is almost constant except at very low pressure (atmospheric). This can be explained considering a Langmuir isotherm. At high pressures the surface concentration of C, so its coverage, is elevated blocking almost all the available sites to the gas phase. When the pressure is reduced the coverage is diminished and the apparent surface reaction rate increases being more sites available. This also means that the surface reaction, at least at high pressures, is apparently the rate determining step. This is not due to a slow intrinsic reaction rate, but to the availability of active sites. The real rate determining step is probably the diffusion of the carbon from interface 1 to interface 2. This is also a verisimilar behavior.

More careful consideration should be given to ψ_d. If we compare Figure 5.9 (with the effect of the hindrance factor) and Figure 5.8 (not considering the hindrance limitations) we see that in the first case ψ_d seams diminished by a pressure increase while in the latter it is increased. However, with the introduction of the hindrance factor ξ_{FC}, we have introduced a second deactivation route parallel to the coverage of the surface with carbon. It results in an inevitable correlation of the two parameters that model the same effect. This is evidenced by the large error associated with both ψ_d and $\xi_{FC.}$ Probably, the real trend of ψ_d is the one shown in figure 5.8, while the apparent decrease of figure 5.9 is due to the shift of part of the deactivation effect towards $\xi_{FC.}$

To summarize, using our chemical potential model, introducing or not the effect of the hindrance of the support, we have observed:

a) An increasing activation kinetic at increasing pressure that is in agreement with the faster nucleation and reduction of the average diameter that we have observed before.

b) A small surface decomposition kinetic ψ_S that seems to be zeroth order as a function of the pressure of CO. This would suggest that this step is the rate determining in the growth of SWNT and that is limited by the availability of surface site that are covered by carbon waiting to diffuse to the interface 2. This is also a likely scenario being the surface reactivity very high at elevated temperatures, while the diffusion through the solid phase or over the surface is still low, leaving a metal surface almost totally covered by carbon atoms.

c) An increasing deactivation kinetic due to a higher carbon deposition.

d) In the case of hindrance by the support, the termination of the growth by this phenomenon is probably the dominant one. However, in this case, is hard to separate this effect from the deactivation due to carbon deposition on the metal surface.

5.4. Conclusions

While this model is simple and may not capture all the possible phenomena that are present on the catalyst, it is able to obtain parameters with physical significance that, at least, follow a trend expected by experimental observations:

a) The carburization process is very fast and almost stoichiometric (at pressures above atmospheric). It completes in few minutes after contacting with CO.

b) There is an increase in the rate of activation at higher pressures. This increase matches with the reduction of average diameter and the change in chirality observed at increasing pressures.

c) The rate determining step seems to be the availability of surface sites to decompose CO. The surface is covered by carbon that is waiting to diffuse to interface 2 to form the SWNT.

d) There is an increase in deactivation at high pressures. This is associated with the increased yield, so the amount of carbon deposited. This effect is probably masked by the greater effect of the support hindrance.

With the use of a chemical potential model, where the kinetic is modeled using the difference between chemical potential at the gas-metal interface and the metal-SWNT interface, we were able to capture the trend in the physical processes that are behind the SWNT growth and find what is reasonably the rate determining step.

This chemical potential model has shown many possibilities to capture the real processes that define the SWNT growth; however, due to the high number of parameters involved, a further refining is necessary. A future work using, for example, engineered catalyst support or changing the temperature of the reaction, will help separate the effects of the single model components. This will allow us to increase the significance and the certainty of these parameters.

We can also think at the chemical potential model as a tool to diagnose the reaction in an industrial environment. Through the model, and monitoring the CO_2 evolved, is possible to follow each aspect of the process and, eventually, take provisions to optimize it.

List of symbols used

Term	Definition	units
A	Catalyst activity	-
a_0	Initial catalyst activity	-
a_p	Potential catalyst activity	-
a_{p0}	Maximum potential catalyst activity	-
a_{p*}	Constant defined in equation 5.11	-
a_S	Residual catalyst activity, defined in equation 5.25	-
A_0	Constant defined in equation 5.44	time, min
A_1	Constant defined in equation 5.44	time, min
A_2	Constant defined in equation 5.44	time, min
A_3	Constant defined in equation 5.44	time, min
A_4	Constant defined in equation 5.44	time, min
C_F	Carbon concentration at the SWNT-phase side	mol C/g cat.
C_S	Carbon concentration at the gas-phase side	mol C/g cat.
C_{S0}	Maximum carbon concentration at the gas-phase side	mol C/g cat.
$D_{C,met}$	Carbon diffusivity on the metallic particles	m^2/s
d_{met}	Average metallic particle diameter	m
E_1	Activation energy for CO decomposition	kJ/mol
E_a	Activation energy for activation step	kJ/mol
E_d	Activation energy for deactivation step	kJ/mol
E_r	Activation energy for regeneration step	kJ/mol
ΔG	Gibbs energy for CO decomposition	kJ/mol

k_c	Kinetic constant for the carburization	s^{-1}
K	Autocatalytic kinetic constant	-
k_1	Kinetic constant for CO decomposition	s^{-1}
k_a	Kinetic constant for activation step	s^{-1}
k_d	Kinetic constant for deactivation step	s^{-1}
k_r	Kinetic constant for regeneration step	s^{-1}
k_{10}	Pre-exponential factor of CO decomposition	mol CO.g cat^{-1}.s^{-1}.bar^{-1}
k_{a0}	Pre-exponential factor of activation step	$s^{-1}bar^{-ma}$
k_{d0}	Pre-exponential factor of deactivation step	$s^{-1}bar^{-md}$
k_{r0}	Pre-exponential factor of regeneration step	$s^{-1}bar^{-mr}$
k_C	Transport coefficient of carbon on Co particles	m^2/s
K_{eq}	Equilibrium constant of CO decomposition	bar^{-1}
j_{C0}	Maximum flux through the metal particles	mol g cat^{-1} min^{-1}
L_{act}	Concentration of active sites	mol site.g cat^{-1}
L_{act0}	Initial concentration of active sites	mol site.g cat^{-1}
L_{deact}	Concentration of deactivated sites	mol site.g cat^{-1}
L_{inact}	Concentration of inactive sites	mol site.g cat^{-1}
L_{inact0}	Initial concentration of inactive sites	mol site.g cat^{-1}
L_{ox}	Concentration of oxidized sites	mol site.g cat^{-1}
L_{ox0}	Initial concentration of oxidized sites	mol site.g cat^{-1}
L_{red}	Concentration of reduced sites	mol site.g cat^{-1}
L_{red0}	Initial concentration of reduced sites	mol site.g cat^{-1}
L_T	Total concentration of sites	mol site.g cat^{-1}
m_a	Kinetic order in equation 2	-

m_d	Kinetic order in equation 5	-
m_r	Kinetic order in equation 5	-
m_C	Mass of SWNT accumulated over the catalyst	g C.g cat^{-1}
p_{CO}	Partial pressure of CO	bar
p_{CO2}	Partial pressure of CO_2	bar
$(-r_{CO})^0$	Maximum rate of CO decomposition	mol CO.g cat^{-1}.min^{-1}
r_{carb}	Rate of carburization	mol C.g cat^{-1}.min^{-1}
r^*_{carb}	Stoichiometric amount of carburization	mol C.g cat^{-1}
r_{SWNT}	Rate of SWNT production	mol C.g cat^{-1}.s^{-1}
r_{Tot}	Total rate	mol C.g cat^{-1}.s^{-1}
R	Molar gas constant	J.mol^{-1}.K^{-1}
T	Temperature	ºC, K
t	Time	min

Greek letters

α	Degree of carburization	-
α_1	Constant defined in equation 5.26	-
α_2	Constant defined in equation 5.26	-
α_3	Constant defined in equation 5.35	-
ε_{carb}	Efficiency of carburization	-
ψ'_a	Pseudo-activation kinetic function defined in eq. 5.11	min^{-1}
ψ_a	Activation kinetic function	min^{-1}
ψ_c	Carburization kinetic function defined in eq. 5.4	min^{-1}
ψ_d	Deactivation kinetic function	min^{-1}
ψ_r	Regeneration kinetic function	min^{-1}
ψ_S	Surface reaction kinetic function	min^{-1}
ψ_G	Global kinetic function, defined in equation 5.25	min^{-1}
$\rho_{\mu\varepsilon\tau}$	Bulk density of metallic particles	$kg.m^{-3}$
ξ_F	Dimensionless Hindrance factor	-
ξ_{FC}	Hindrance factor - defined in equation 5.42	min^{-1}

Reference:

1 J. Zhao, A. Martinez-Limia, P.B. Balbuena *Nanotechnology* **2005** 16, 575

2 K.Bolton, F. Ding, A. Rosen *Journal of Nanoscience and Nanotechnology* **2006** 6, 1211

3 E. G. Proute, F.C. Tompkins *Trans. Faraday Sot.* **1944** 40, 488

4 B. Delmon Bull. Sot. Chim. France **1961** 590

5 T. V. Hiep, S. Kaliaguine *Chem. Eng. Sci.* **1973**, 28, 195

6 J.I. Villacampa , C. Royo, E. Romeo, J.A. Montoya, P. Del Angel, A. Monzón *Applied Catalysis A: General* **2003** 252, 363.

7 M. Pérez-Cabero, E. Romeo, C. Royo, A. Monzón, A. Guerrero-Ruíz, I. Rodríguez-Ramos, *Journal of Catalysis* **2004** 224, 197.

8 D. Farcasiu, J.O. Li, A. Kogelbauer *Journal of Molecular Catalysis A* **1997,** 124, 67.

9 E.L. Agorreta, J. A. Peña, J. Santamaria, A. Monzón, *Ind. Eng. Chem. Res.* **1991** 30, 111-122

10 P. Mcallister, E.E. Wolf *Journal of Catalysis* **1992**, 138, 129.

11 M. Morbidelli, A. Servida, and A. Varma, *Ind. Eng. Chem. Fund.* **1982**, 21, 278

12 A.L. Pozzi, H.F. Rase *Catalyst fouling, Ind. Eng. Chem.* **1958** 50, 1075–1080.

13 J. Corella, J. Adanez, A. Monzón, *Ind. Eng. Chem. Res.* **1988,** 27, 375

14 A. Borgna, T.F. Garetto, A. Monzón, C.R. Apesteguía, *Journal of Catalysis* **1994** 146, 69– 81.

15 J.W. Snoeck, G.F. Froment, M. Fowles *Ind. Eng. Chem. Res.* **2002**, 41, 4252.

16 S. Huang, M. Woodson, R. Smalley, J. Liu *NanoLetters* **2004,** 4, 1025.

17 L.X. Zheng, M.J. O'Connell, S.K. Doorn, X.Z. Liao, Y.H. Zhao, E.A. Akhadov, M.A. Hoffbauer, B.J. Roop, Q.X. Jia1, R.C. Dye, D.E. Peterson, S.M. Huang, J. Liu, Y.T. Zhu *Nature Materials* **2004** 3, 673.

18 K. Hata, D.N. Futaba, K. Mizuno, T. Namai, M. Yumura, S. Iijima *Science*, **2004** 306, 1362.

19 L. Zhang, Y. Tan, D. E. Resasco, *Chemical Physics Letters* **2006** 422, 198

20 D.N. Futaba, K. Hata, T. Yamada, K. Mizuno, M. Yumura, S. Iijima *Physical Review Letters* **2005** 95, 056104.

21 D.N. Futaba, K. Hata, T. Namai, T. Yamada, K. Mizuno, Y. Hayamizu, M. Yumura, S. Iijima *Journal of Physical Chemistry B* **2006** 110, 8035

22 L. Zhang, Z. Li, Y. Tan, G. Lolli, N. Sakulchaicharoen, F.G. Requejo, B.S. Mun, D.E. Resasco *Chemistry of Materials* **2006,** 18, 5624

CHAPTER 6

6. Conclusions

The selective growth of SWNT and of a specific (n,m) chirality is a major scientific and industrial goal. Separation methods have been proposed, but presently they are economically unfavorable and limited at laboratory scale. Moreover, the best separation results are achieved only starting from an already narrow (n,m) distribution.

The production method we developed, called CoMoCAT®, presents very high selectivity towards SWNT and a very narrow diameter distribution. In this contribution, we have studied the fundamental aspects of the catalyst to reveal the requirements for reaching high Type I selectivity (selectivity towards SWNT vs. other forms of carbon) and Type II selectivity (selectivity towards a specific (n,m) SWNT). We have also demonstrated that Type III selectivity (selectivity towards a specific length of SWNT) is related to the hindering limitations of the support morphology and we introduced a new concept, called hindrance factor, that is critical for modeling the growth mechanism of SWNT with physical significance.

Based on our results, the most important requirement for Type I selectivity is the formation of a stable and homogeneous $CoMoO_x$ phase, which stabilizes the Co ions until they are released during the reaction. As soon as these ions are freed, they get reduced by CO and agglomerate forming small metal clusters that initiate the SWNT growth. The first step of the nucleation is the formation of a SWNT cap ("embryo") on the surface of the metal particle. These embryos can start the growth of a specific SWNT depending on the particle diameter at the time of formation.

Because the diameter (and the (n,m) distribution) is determined by the instantaneous structure of the metal particle at the time of SWNT growth, the resulting SWNT chirality is determined by the balance between the metal particle growth, due to sintering and addition of more Co ions, and the rate of nucleation of SWNT on the surface. We have discovered that, if we increase the nucleation rate, changing the conditions of the reaction (e.g. increasing the pressure of the system, and supplying more carbon), the SWNT distribution tends to become narrower around a specific diameter of about 0.75 nm. The size of the Co particle associated with this diameter is the critical diameter below which the catalytic activity is suppressed. This is explained considering that the number of atoms present in a 0.8 nm Co particle is around 24. Smaller particles do not have high enough carbon solubility to initiate the VLS mechanism.

For this reason, when the nucleation kinetic is faster than the rate of growth of the metal particle, the selectivity towards a specific range of (n,m) tubes is greatly enhanced around a critical size. When, on the contrary, the nucleation kinetic rate is reduced, the diameter distribution becomes broader, and the average diameter becomes larger.

To control the nucleation kinetic we can either increase the rate of carbon deposition, for example by increasing the pressure of the system, or reduce the activation energy for the nucleation step. We found that the addition of N_2 to the system increases the nucleation kinetics without affecting the quality of the product. This has been explained by the insertion of some N atoms inside the SWNT lattice that can increase the curvature of the cap, reducing the stress, and so reducing the activation energy associated with the process of cap formation.

To better understand the growth process we developed a chemical potential model, where the rate of SWNT growth is proportional to the difference in fugacity between the gas-metal interface and the metal-SWNT interface. Kinetic data was obtained from a series of experiments performed in different operating conditions that allowed us to test the model.

We found that at increasing partial pressure of CO, the activation kinetics (so the nucleation of a SWNT) increases. This trend agrees with the experimental observation of a smaller SWNT distribution at higher pressures.

The deactivation process also seems to increase with CO pressure. This was modeled using two different effects: pure deactivation due to coverage of the active sites by carbon, in equilibrium with a regeneration process of gasification by CO_2, and due to the hindrance of the support that impedes the growth of SWNT, thus reducing the driving force of the process. This new concept has been shown to be dominant in the case of high surface area catalysts.

We also found that the rate determining step of the SWNT growth (once they are nucleated) is the availability of surface sites. The rate of the surface reaction was found to be zeroth order in CO suggesting that the lack of active sites, probably covered by carbon atoms waiting to diffuse, is responsible for the limitation of the rate.

The increased carbon yield at high pressures is due to a higher number of active sites, so a higher number of SWNT produced, more than a faster growth rate.

We also found that the addition of traces of gases that help cleaning the surface can increase the quality of the product. In the case of CO_2, we found that the addition up to 3,000 ppm in the CO stream increases the quality (probably due to cleaning of the surface) while the addition of water does not improve quality. In fact, more than 250 ppm of H_2O actually destroys the carbon formed, thus resulting in poor quality and low yield.

APPENDIX A

A. Experimental methods

A.1. SWNT Growth

A.1.1. Catalyst preparation

The SiO_2-supported catalyst (2% total metal 1:3 Co/Mo molar ratio) was prepared by incipient wetness co-impregnation using an aqueous solution of $(NH_4)_6Mo_7O_{24} \bullet 4\ H_2O$ and $Co(NO_3)_2 \bullet 6\ H_2O$ (both from Sigma Aldrich). The wet material was then dried in a convection oven at 110 °C for 12 hours and then calcined at 500 °C for 3 h.

The SiO_2 supports were: Silica Gel (Alfa Aesar) [S.A. 500 m^2/g P.V. 0.7 ml/g] and precipitated silica (Hisil 210 from PPG) [S.A. 150 m^2/g P.V. 1.1 ml/g].

A.1.2. SWNT production

The reaction was performed in a vertical fluidized-bed quartz reactor of 25 mm ID equipped with 2 quartz porous discs to hold the fluidized catalyst powder in the reaction zone 100 mm long. The reactor was placed at the center of an electric furnace, 300 mm heated zone, and the controlling thermocouple was mounted at its center, very close to the quartz tube.

The catalysts, 0.5 grams, were pre-reduced in flowing H_2 (500 sccm) using a temperature ramp of 10 °C/min until the optimal reduction temperature was reached and holding 30 minutes at this temperature. The pre-reduction step is critical for the performance of the catalyst, as described in Chapters 3 and 4, and can be optimized by performing a temperature programmed reduction [3]. The optimum temperature for SiO_2-supported catalyst is 500-550 °C.

After the pre-reduction step the reactor was purged for 5 min. with inert gas (500 sccm), He if not specified otherwise, and the temperature was increased to 750 °C maintaining the gas flow. The temperature was let to stabilize for 5 more min. and the system was pressurized by mean of a back-pressure regulator placed after the reactor.

At this point, the flow was switched to CO (1,000 sccm) and the catalyst was let react for 30 min. After this time, the reactor was purged with He (500 sccm) and let cool down gradually under He flow.

In general, He is used as inert gas, but some experiments were performed using Ar or N_2 according to the description in the text. All the gases were UHP grade (ultra high purity) purchased from AirGas. The inert gases were purified of oxidizing agents (O_2, H_2O, CO_2) by a chemical trap (Mini Gas-Kleen purifier from Pall Corporation). According to the specifications the outlet purity is < 1 ppb contaminants. [1] The CO was purified of metal carbonyls and CO_2 by a Maxi Gas-Kleen purifier also from Pall Corporation. The H_2 was used as is and not purified.

For the addition of chemically active promoting gasses (CO_2 and H_2O) an extra service line with a 5 sccm mass flow controller was used. In the case of water addition, Helium was bubbled through a humidifier heated at the opportune temperature.

A.2. SWNT Characterization Techniques

A.2.1. Raman Spectroscopy

Raman spectroscopy is a very powerful SWNT characterization technique and is used to obtain information on their vibration and electronic structure. It is based on the inelastic scattering of visible light by matter. When light interacts with a substance it may be absorbed, transmitted, or scattered. The light may be scattered elastically or inelastically. Elastic scattering is the most common phenomenon and occurs without loss of photon energy (so frequency) but only change in direction (Raleigh scattering). In the inelastic scattering the photon interacts more deeply with the matter and loses or increases its energy. This frequency difference is called the Raman shift. The frequency increase/decrease is quantized and match as the phonon density of states of the sample. If, upon collision with a molecule, the photon loses some of its energy, the resulting radiation has a positive Raman shift (Stokes scattering). In contrast, when the incoming photons gain energy, the resulting radiation has higher frequencies (anti-Stokes scattering) and negative Raman shift is observed. To observe anti-Stokes scattering the initial ground-state of the molecule should be an excited state, so with empty vibrational energy levels underneath. This means that in the completely relaxed state (at 0 K) the anti-Stokes vibrations are not observed. Their intensity increases with increasing sample temperature.

A limitation of Raman spectroscopy is the extremely low cross sections associated with the process (about 1 every 10^6 photons is affected by Stokes scattering). Sometimes, the low efficiency of the Raman scattering process can be improved through the so-called resonant Raman effect. There are two kind of resonance effect. One is surface-enhanced resonance (SER). This happens when a substrate (commonly Ag) is excited by the laser light, generally by mean of a surface plasmon wave, and then this excitation is transferred to the sample molecule in a more efficient way than direct interaction with the incoming photon. The second kind of resonant Raman (the one that happens in SWNT) is direct resonance. This resonant effect occurs when the energy of the incoming or outgoing photon matches the energy of an allowed opto-electronic transition within the sample. [2,3] In the particular case of SWNT the resonant Raman effect is very strong due to the sharp Van Hove singularities present in the one-dimensional electronic density of states. The energy difference between the spikes falls in the visible and near-infrared range [4- 9] and as consequence , when the excitation laser energy is close to that of an allowed optical transition between singularities in the one-dimensional density of states of SWNT, the Raman intensity is greatly enhanced. [10-12]

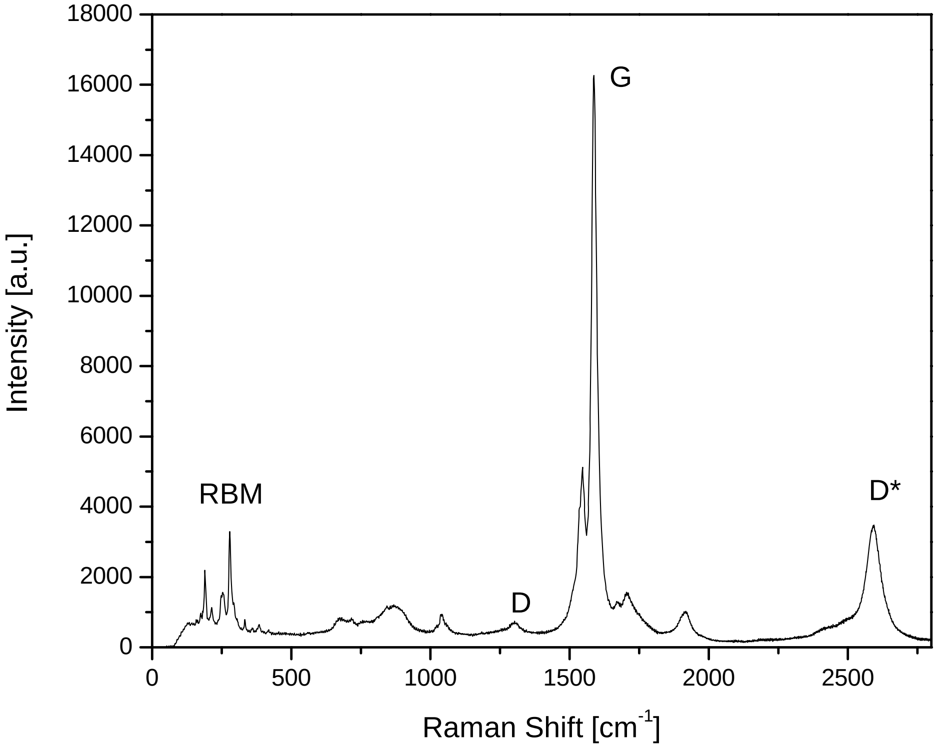

Figure A.1 Typical raman spectrum of a SWNT sample. The 4 characteristic bands are marked: RBM (100-350 cm^{-1}), D (around 1300 cm^{-1}), G (1592 cm^{-1}) and D* (around 2600 cm^{-1})

In Figure A.1, the Raman spectrum of a typical SWNT sample is illustrated. The spectrum has three main first-order components: the so-called radial breathing mode (RBM) at around 250 cm^{-1}, the D-band around 1,300 cm^{-1}, and the G-band at 1,592 cm^{-1}. It is also labeled the strongest second-order (2 phonons) band (D*) around 2,600 cm^{-1}.

The radial breathing mode is a low frequency (generally below 350 cm^{-1}) A_1 mode corresponding to the symmetric expansion and contraction of the tube diameter around the tube axis. It resembles the movement of the chest during breathing. These bands have been proposed to be independent of chirality. [13] Bandow et al. calculated the RBM frequencies of all types of SWNT and found that all frequencies fall on a common line according to the expression: [14]

$$\omega_{RBM} \cong \frac{248}{d} \quad \omega(cm^{-1}) \quad d(nm)$$

Equation A.1

Besides the radial breathing mode band, the Raman spectra of SWNT also comprise a disorder-induced Raman band (D-band), which is a feature common to all sp^2 hybridized disordered carbon materials. In principle, this vibration is Raman-forbidden because the defect vibrating generates a dipole moment. However, by a double resonance effect that can involve a defect and/or another phonon it becomes visible in Raman. [15] In the specific, the electron is excited in an energy space with non zero momentum (k), so when scatters and generates the vibrating phonon, for the conservation of the total momentum of the system, it revert its momentum so is no more possible the recombination with the hole that now is in opposite k-space. This is the typical Raman forbidden process when the final state is not allowed. However, it can scatter elastically against a defect present in the lattice of the SWNT or inelastically against another phonon generating the D (1,300 cm^{-1}) and D* (2,600 cm^{-1}) bands respectively. Thus the ratio D/D* represent the probability for the excited electron to scatter against a defect or against a phonon so it is a measure of the density of defects in the SWNT. This effect is illustrated in Figure A.2.

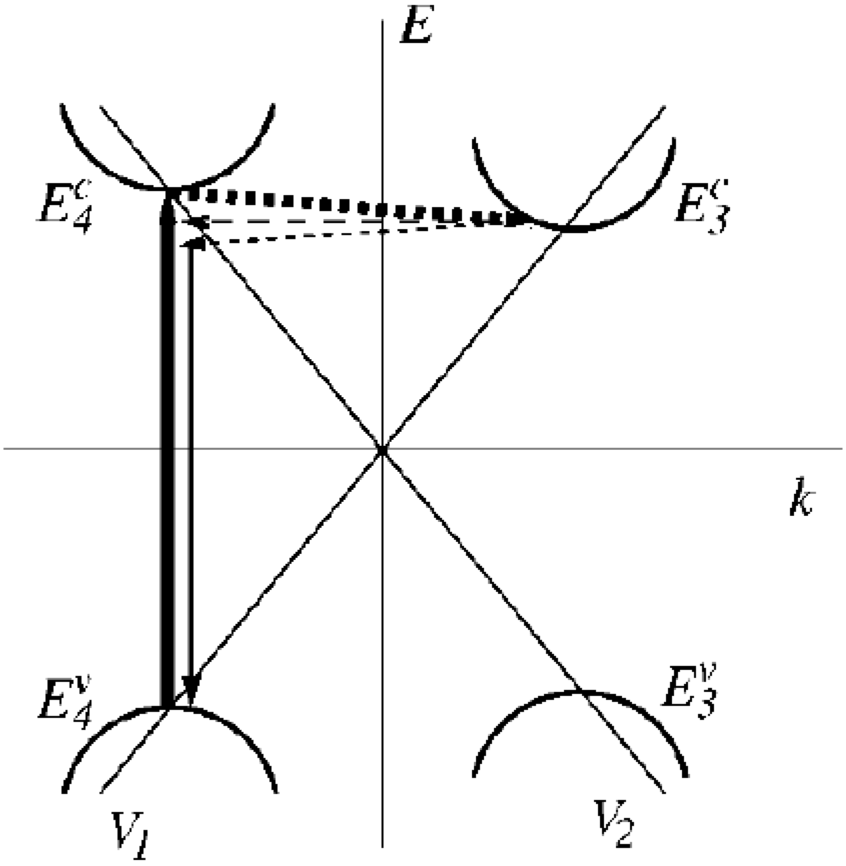

Figure A.2 Schematic of the origin of the D and D* band. The excited electron is transferred from the conduction to the valence band (bold continuous line) and the phonon is generated (bold dashed line). Because the phenomena happens at non zero momentum (k) to recombine with the hole it can either scatter elastically against a defect (long dash) or inelastically against a second phonon (short dash). The resulting Raman shift will be respectively 1,300 (D) and 2,600 (D*) cm^{-1}. [16]

Thus the D-band is usually regarded as an overall indicator of defects: sp^3 carbon atoms, holes in the SWNT walls, attached functional groups, and in fact, non-nanotube graphitic domains all contribute to the D-band. The D-band has been related not just to defects on SWNT but also to the presence of other forms of disordered carbon such as carbon nanoparticles and amorphous carbon. [17] However, these forms of carbon are generally non resonant, so the signal generated from them is largely overcome by the one resulting from the SWNT. Therefore, the relative intensity of the D-band has been used only as a qualitative indication of the presence of undesired forms of carbon (i.e., microcrystalline graphite, amorphous carbon, MWNT, carbon nanofibers), while it can be a semi-quantitative indication of defects inside the SWNT lattice.

The most intense line of the SWNT Raman spectrum is the so-called G-band which corresponds to the tangential C-C stretching. The G-band in carbon nanotubes presents a left shoulder (generally referred as G^-). This splitting is due the difference of the C-C vibration along the axis of the tube (G) and along the circumference (G^-). This is generated by the curvature of the SWNT. The larger is the SWNT (so lower is the curvature) the more the G^--band overlaps to the main G feature. A clearly separated G^- is indication of small diameter SWNT.

The spectrometer used was a Jovin Yvon-Horiba LabRam HR-800 equipped with a CCD detector and a single notch filter. The laser excitation energy was 1.96 eV (633 nm).

A.2.2. SWNT suspensions

Right after production, the nanotubes are present in the form of bundles. For many applications the goal is obtaining individual nanotubes with a fixed (n,m) chirality. Moreover, the nanotubes optical features (optical absorption and fluorescence) are seriously compromised in the presence of bundles. An effective way for obtaining stable suspensions of individual SWNT is the use of surfactants. The most widely used are sodium dodecil sulphate (SDS) [18,19] and sodium dodecil benzene sulphonate (SDDBS). [20] Weisman et al. [18,19], using a 1% SDS suspension, have assigned for many small-diameter semiconducting tubes an experimental values for the S_{11} and S_{22} transition of each that differs slightly from the theoretical values calculated by Kataura et al.. [21] The experimental values obtained by Weisman are more accurate in the individuation of SWNT because they consider the perturbation due to the surrounding absorbed surfactant molecules. In a recent contribution, we showed that sodium cholate (a bile salt) is even more effective than SDDBS in deboundling and suspending SWNT. [22]

To obtain the stable surfactant suspension 20 mg of as-produced SWNT material were added to 7 ml of 2% NaCholate (Sigma Aldrich) solution and processed in a horn sonic dismembrator (CPX 750, Cole-Parmer) equipped with a microtip of 1/8” in diameter for 60 minutes at 7W of power. To prevent heating, the vial was placed in a water-cooled bath. The resulting black suspension was ultracentrifuged at 25,000 G for 1 hr to precipitate the not debundled tubes and the catalyst present.

A.2.3. SWNT (n,m) analysis

The (n,m) distribution of individual tubes in the suspension was analyzed using optical absorption. The optical features observed correspond to electronic transitions inside the joined density of states of the nanotubes, and in particular between the corresponding pairs of Van Hove singularities. [23-27] These can be matched with theoretical or experimental data associated with the different (n,m) nature of the SWNT. [18,19]

The equipment used was a Bruker Equinox 55 FTIR and a Shimadzu double beam spectrometer UV-2101 for the UV-VIS region. 10 mm light path "I" grade Quartz cuvettes were used. The centrifuged supernatant was diluted to reach absorbance equal 1 at 800 nm.

A.2.4. TPO

The method that we have developed for quantifying the amount of SWNT produced is based on the standard temperature programmed oxidation technique (TPO), commonly employed in catalysis research. A continuous flow (80 sccm) of 5% O_2/He was passed over the catalyst containing the carbon deposits while the temperature was linearly increased (10 °C/min). The evolution of CO_2 produced by the oxidation of the carbon species was monitored by a FID (SRI 110) placed after a methanation catalyst bed made of 10% Ni on alumina. Accurate quantification was performed by injecting a control pulse (100 μl) of CO_2 before each run.

A.3. Catalyst characterization

A.3.1. TPR

Temperature-programmed reduction (TPR) experiments were conducted passing a continuous flow of 5% H_2/Ar (50 sccm) over approximately 50 mg of the calcined catalyst, while linearly increasing the temperature at a constant heating rate of 10°C/min. The hydrogen uptake as a function of temperature was monitored using a thermal conductivity detector, SRI Model 110 TCD.

A.3.2. NO Absorption

Absorption of NO (nitric oxide) was performed in a custom-made in-situ transmission cell used also for XANES/EXAFS experiments. It allows introducing different gases and operating in a wide temperature range (70-1000 K). A self-supporting 1" catalyst pellet was made by pressing 50 mg of catalyst in a hydraulic press. The resulting pellet, about 200 μm thick, was placed in the spectrometer beam inside the cell (Bruker Equinox 55 FTIR). The catalyst was reduced in flowing H_2 (100 sccm) to the reduction temperature. This temperature was maintained for 10 min. and then cooled in He (100 sccm) to 50 °C. At this low temperature was introduced a mixture of 5% NO in He (50 sccm) for 20 min. The system then was purged with He (100 sccm) for another 20 min. and the spectrum of the absorbed species acquired. In each case the reference background spectrum was taken just before the introduction of NO.

A.3.3. XRD

X ray diffraction pattern were acquired using a Bruker AXS Discovery G8 equipped with GADDS detector. The GADDS is an aerial detector that, despite the low photonic efficiency, presents extremely high resolution and sensitivity. This is allowed by integrating a whole sector of the diffraction cone instead of a single line. This feature open up the possibility of measuring very dispersed and diluted catalyst samples (2% total MeOx on amorphous silica). In a typical experiment the acquisition time to scan the 2θ region 10-90° was 12 h.

The resulting diffractogram was analyzed using the powder diffraction database PDF-2 2004 from ICDD to individuate the phases presents.

A.4 Kinetic Analysis.

A.4.1. MS acquisition

A mass spec (MKS RGA Y-200amu) was connected to the exit of the reactor by a stainless steel capillary (1/64” ID 1/16” OD about 6’ long). The capillary was first connected to a manifold system vacuumed to 5E-1 torr. The pressure in the manifold was controlled by mean of a needle valve. The total flowrate through the capillary was determined by the pumping capacity, so it was kept constant between the experiments. The manifold was then connected to the mass spec chamber by a metering valve to maintain the pressure inside the main chamber at 1.5 E-5 Torr.

The mass range 1-50 amu was scanned at 6 seconds intervals and a data point was recorded every 18 seconds. All the masses (main ions and fragments) were followed to obtain quantitative data from the system.

Even if high attention was paid to maintain the system in the same conditions from run to run, differences arise from the different reaction conditions inside the reactor. In particular, in the case of increasing pressure in the system, the apparent rector volume, so the residence time distribution, changes in function of pressure. To obtain quantitative and correct data on the kinetic is necessary to measure the gas composition in the reactor bed, not at the exit of the reactor, or worst at the detector.

A.4.2. MS deconvolution

To solve the problem described above we need to solve the inverse of the response of a system to an inlet function. We can measure the output and we are interested in the input that generated it. This principle is illustrated in Figure A.3.

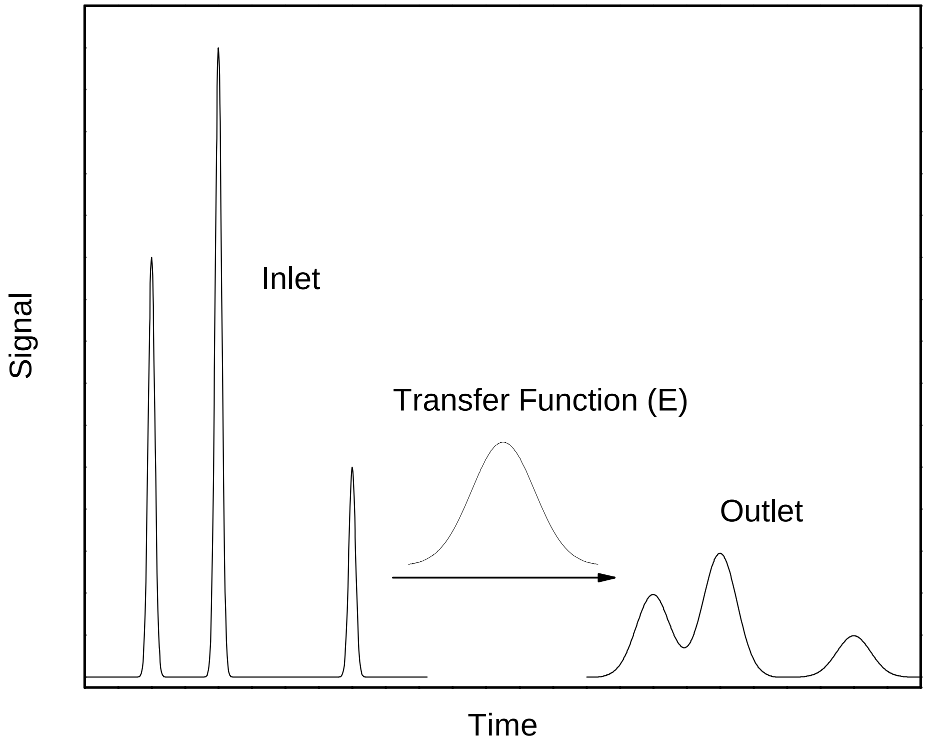

Figure A.3 Representation of the effect of the convolution integral (transfer function E).

The convolution integral is defined as: [28]

$$C_{out}(t) = \int_0^t C_{in}(t-t') \cdot E(t') \cdot dt' \qquad \textbf{Equation A.2}$$

Or in an equivalent form:

$$C_{out}(t) = \int_0^t C_{in}(t') \cdot E(t-t') \cdot dt' \qquad \textbf{Equation A.3}$$

where dt = dt’

According to this definition, $C_{out}(t)$ is the convolution of $C_{in}(t)$ with the residence time distribution of the vessel, $E(t)$, and this can be written concisely as:

$$C_{out}(t) = C_{in}(t') * E(t-t') \qquad \textbf{Equation A.4}$$

The convolution operator * in the time domain is not invertible, but it is equivalent to multiplication operation in frequency dominium (see for example [29]). Therefore, calculating the Fourier transform, the above equation is converted into the following expression: [30]

$$F[C_{out}(t)] = F[C_{in}(t')] \cdot F[E(t-t')] \qquad \textbf{Equation A.5}$$

The concentration at the inlet of the vessel can be directly deduced as the inverse Fourier transform:

$$C_{in}(t') = F^{-1}\left[\frac{F[C_{out}(t)]}{F[E(t-t')]}\right]$$ **Equation A.6**

This calculation implies to know the mathematical form of the $C_{out}(t)$ and $E(t-t')$. In other cases, numerical solution can be reached by mean of Fast Fourier transform (FFT) algorithms. Numerically also the direct convolution integral is calculated using the FFT:

$$C_{out}(t) = F^{-1}\left[F[C_{in}(t')]\cdot F[E(t-t')]\right]$$ **Equation A.7**

In contrast to convolution (equation A.7), deconvolution (equation A.6) is very sensitive to noise of the transfer function E(t) , due to the ratio between the Fourier transforms. In particular this noise tends to have a frequency corresponding to the sampling rate of E(t). To obtain the final value of C_{in} a Fourier low pass filter should be applied to cut out the noise introduced by the transform of E(t). [31] This filter does not alter the signal if the time scale of the process is much longer than the sampling interval (in our case 30 minutes against 18 seconds sampling). This will be clearer in the following examples.

To calculate E(t) we can consider a known inlet and measure what is the response of the system at that inlet. In particular, if $C_{in}(t)$ is chosen wisely an analytical solution is possible. If we consider as $C_{in}(t)$ a step function (0 t<0 ; 1 t>0), equation A.2 or A.3 become:

$$C_{out}(t) = \int_0^t E(t') \cdot dt'$$ **Equation A.8**

So

$$E(t) = \frac{dC_{out}}{dt}$$ **Equation A.9**

In the case of our system, the switch from He to CO is a theoretical step function, which is transformed in a more gradual slope by the residence time distribution and diffusion in the system. (Figure A.4) The derivative of the measured increase in CO represents a good estimation of the residence time distribution in the system. (Figure A.5)

For example considering the data from the 20 psi experiment:

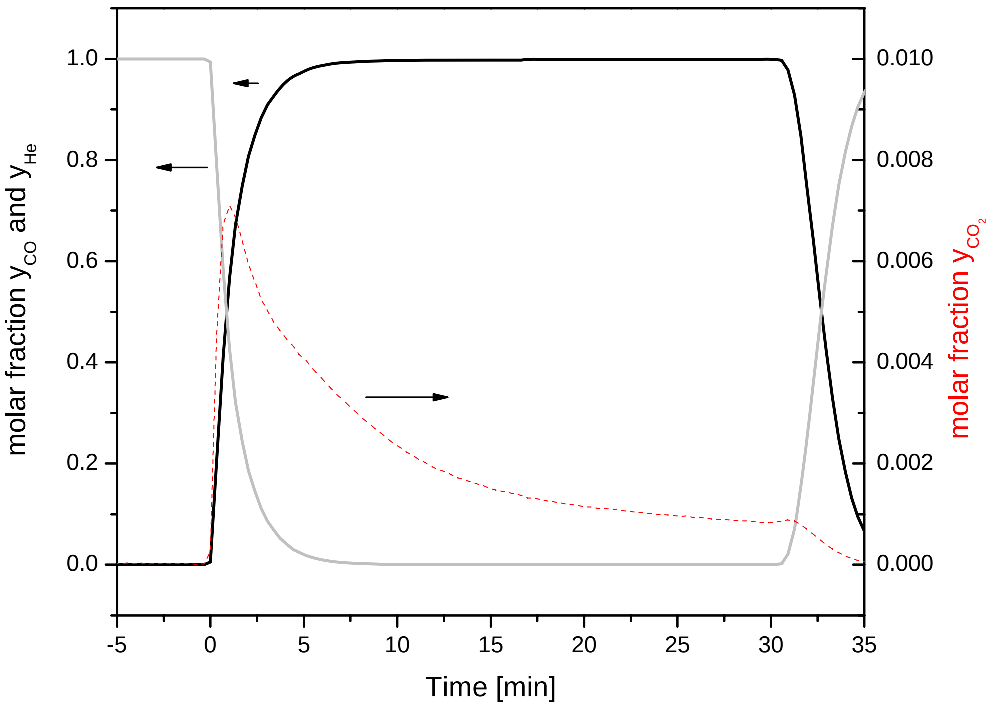

Figure A.4 Raw MS signal obtained from the growth of SWNT at 20 psi. The molar fraction of CO (black), He (gray) and CO_2 (dashed red) are shown.

We can focus on the CO signal (black line) and calculate the derivative to obtain the transfer function E(t):

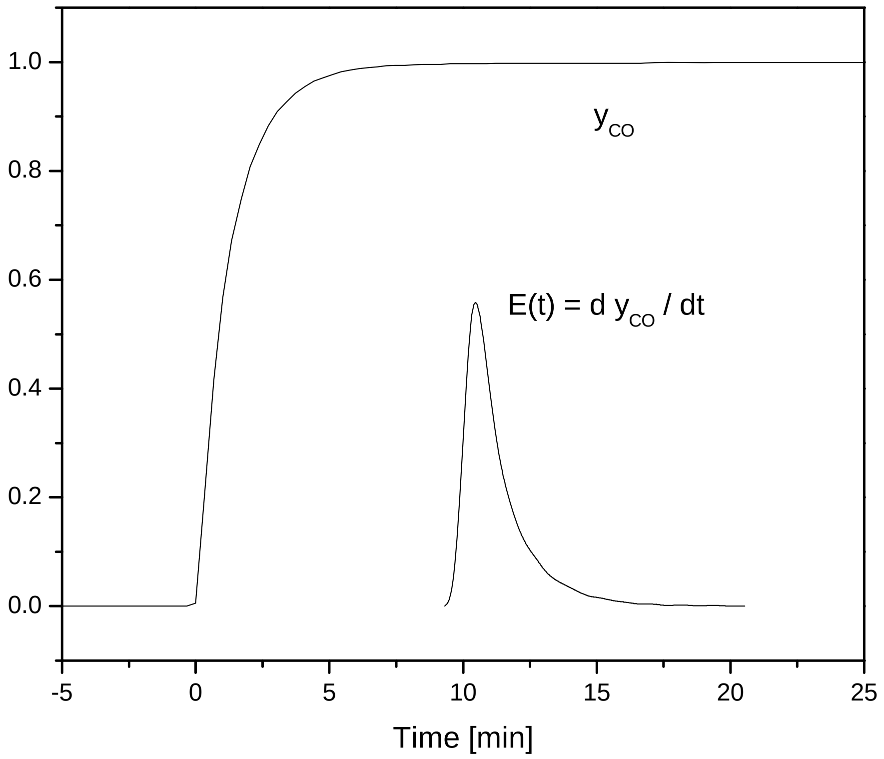

Figure A.5 CO signal from figure A.4 and its first derivative that represent E(t).

Accordingly, it is possible to numerically apply equation A.6 to the signal of CO_2 and obtain the deconvoluted values (red). (Figure A.6) As we can see this signal is very noisy especially at time close to 0. This is due to the numerical backtransformation of the noise of E(t). We can apply a Fourier low pass filter with the same amplitude of the sampling interval to obtain a more corrected curve (blue):

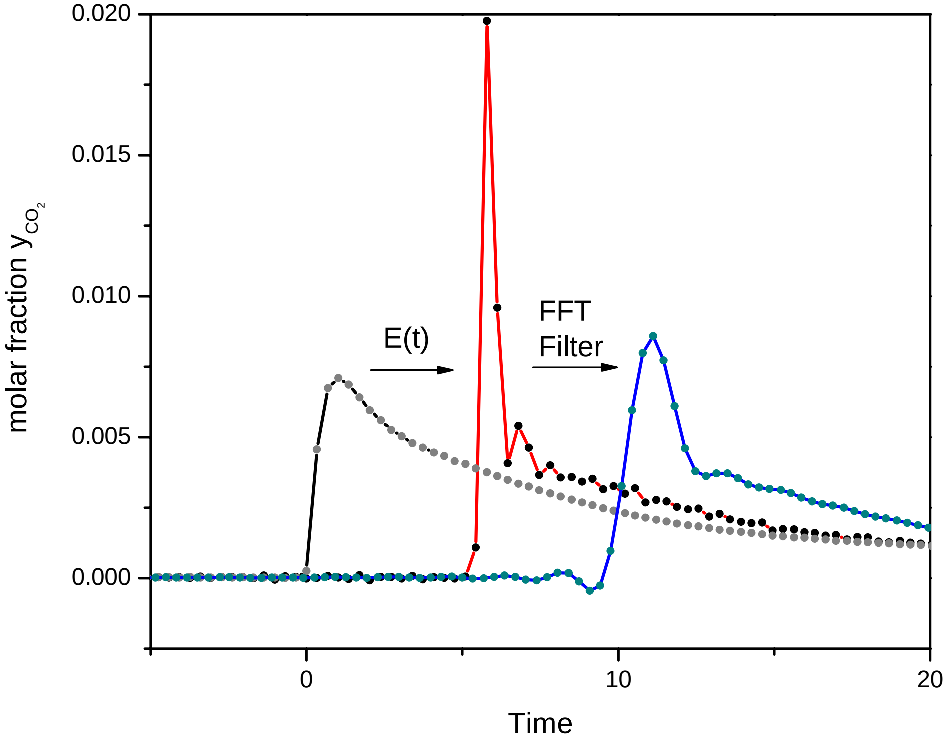

Figure A.6 Deconvolution using E(t) and FFT filtering of the signal (black) to obtain the real CO_2 concentration at the exit of the catalyst bed.

Reference:

1 http://www.pall.com/pdf/A79e_Mini-Gaskleen_Purifier.pdf

2 S.A. Asher *Anal. Chem.* **1993** 65, 59A.

3 S.A. Asher *Anal. Chem.* **1993** 65, 201A.

4 A. Kasuya, M. Sugano, T. Maeda, Y. Saito, K. Tohji, H. Takahashi, Y. Sasaki, M. Fukushima, Y. Nishina, C. Horie *Phys. Rev. B* **1998** 57, 4999.

5. M. S. Dresselhaus, G. F. Dresselhaus, R. Saito *Solid State Commun.* **1992** 84, 201**.**

6 E. Richter, K.R. Subbaswamy, *Phys. Rev. Lett.* **1997** 79, 2738.

7. M. A Pimenta, A.Marucci, S.A.Empedocles, M. G, Bawendi, E. B. Hanlon, A. M. Rao, P. C. Eklund, R. E. Smalley, G. Dresselhaus, M. S. Dresselhaus, *Phys. Rev. B* **1998** 58, R16016.

8. C. T. White and T. N. Todorov *Nature* **1998** 393, 240.

9. D. Östling, D. Tománek, A. Rosén *Phys. Rev. B* **1997** 55, 13980.

10. H. Kataura, Y. Kumazawa, Y Maniwa, I. Umezu, S. Suzuki, Y. Ohtsuka, Y.Achiba *Synth. Met.* **1999** 103, 2555.

11. P. Corio, S. D. M. Brown, A. Marucci, M. A. Pimenta, K. Kneipp, G. Dresselhaus, M. S. Dresselhaus, *Phys. Rev. B* **2000** 61, 13202.

12. S. Reich C. Thomsen, *Phys. Rev. B* **2000** 62, 4273.

13 R. Saito, T. Takeya, T. Kimura, G. Dresselhaus, M.S. Dresselhaus *Phys. Rev. B* **1998** 57, 4145.

14 S. Bandow, S. Asaka, Y. Saito, A.M. Rao, L. Grigorian, E. Richter, P.C. Eklund *Phys. Rev. Lett.* **1998** 80, 3779.

15 C. Thomsen, S. Reich *Phys. Rev. Lett.* **2000** 85(24), 5214.

16 A.G. Souza Filho, A. Jorio, A.K. Swan, B.B. Goldberg, R. Saito, J.H. Hafner, C.M. Lieber, M.A. Pimenta, G. Dresselhaus, M.S. Dresselhaus *Phys. Rev. B* **2002** 65(8) 5417.

17 H. Jantoljak, U. Kuhlmann, C. Thomsen, S. Curran, S. Roth, W. Maser, C. Journet, P. Bernier *Mol. Cryst. Liq. Cryst. Sci. Technol.* **1998** 10, 145.

18 S.M. Bachilo, M.S. Strano, C. Kittrell, R.H. Hauge, R.E. Smalley, R.B. Weisman *Science* **2002,** *298,* 2361.

19 M.J. O'Connell, S.M. Bachilo, C.B. Huffman, V.C. Moore, M.S. Strano, E.H. Haroz, K.L. Rialon, P.J. Boul, W.H. Noon, C. Kittrell, J. Ma, R.H. Hauge, R.B. Weisman, R.E. Smalley *Science* **2002**, *297,* 593.

20 O. Matarredona, H. Rhoads, Z. Li, J.H. Harwell, L. Balzano, D.E. Resasco *J. Phys. Chem. B* **2003,** *107,* 13357.

21 Kataura, H.; Kumazawa, Y.; Maniwa, Y.; Umezu, I.; Suzuki, S.; Ohtsuka, Y.; Achiba, Y. *Synthetic Met.* **1999,** *103,* 2555.

22 Y. Tan, D.E. Resasco *J. Phys. Chem. B* **2005,** *109*, 14454-14460.

23 R. Saito, K. Sato, Y. Oyama, J. Jiang, Ge.G. Samsonidze, G. Dresselhaus, M.S. Dresselhaus *Physical Review B: Condensed Matter and Materials Physics* **2005,** 72(15), 153413.

24 P. Corio, A. Jorio, N. Demir, M.S. Dresselhaus *Chemical Physics Letters* **2004**, 392(4-6), 396-402.

25 A. Jorio, R. Saito, T. Hertel, R.B. Weisman, G. Dresselhaus, M.S. Dresselhaus, *MRS Bulletin* **2004**, 29(4), 276-280.

26 A. Jorio, A.G. Souza Filho, G. Dresselhaus, M.S. Dresselhaus, R. Saito, J.H. Hafner, C.M. Lieber, F.M. Matinaga, M.S.S. Dantas, M.A. Pimenta *Physical Review B: Condensed Matter and Materials Physics* **2001**, 63(24), 245416

27 A.G. Souza Filho, A. Jorio, J.H. Hafner, C.M. Lieber, R. Saito, M.A. Pimenta, G. Dresselhaus, M.S. Dresselhaus *Physical Review B: Condensed Matter and Materials Physics* **2001**, 63(24), 241404

28 O. Levenspiel *Chemical Reaction Engineering*, 3rd Ed., **1999** Weiley.

29 http://en.wikipedia.org/wiki/Fourier_transform

30 T. Liliedahl, K. Sjöström, L.P. Wiktorsson *AIChE Journal* **1991** 37(9), 1415-1419.

31 http://en.wikipedia.org/wiki/Deconvolution